



CZECH TECHNICAL UNIVERSITY IN PRAGUE

Faculty of Civil Engineering
Department of Mechanics

**Engineering properties of alkali activated
composites**

DOCTORAL THESIS

Ing. Petr Hlaváček

Ph.D. Programme: Civil Engineering
Branch of study: Physical and Material Engineering

Supervisor: doc. Ing. Vít Šmilauer, Ph.D.

Prague, 2014



CZECH TECHNICAL UNIVERSITY IN PRAGUE
Faculty of Civil Engineering
Thákurova 7, 166 29 Prague 6

DECLARATION BY CANDIDATE

Author: Petr Hlaváček

Title: Engineering properties of alkali activated composites

I hereby declare that this thesis is my own work. The thesis was elaborated under the guidance of my supervisor doc. Ing Vít Šmilauer at the Czech Technical University in Prague, Faculty of Civil Engineering, Department of Mechanics.

All the sources which has been used are mentioned in the bibliography.

In Prague, 4th September 2014

Signature:

Acknowledgments

First of all I would like to appreciate the patience and support of my thesis supervisor doc. Ing. Vít Šmilauer, Ph.D., who helped me with all questions during my study and research. Special thanks belong to doc. RNDr. František Škvára, DrSc. for fruitful technical discussions, which motivated me to solve scientific challenges.

I thank to co-authors of papers attached to this work, namely the already mentioned doc. Ing. Vít Šmilauer, Ph.D. and doc. RNDr. František Škvára, DrSc. and to Ing. Rostislav Šulc, Ph.D., RNDr. Lubomír Kopecký, doc. Ing. Jiří Němeček, Ph.D., Ing. Pavel Padevět, Ph.D. and Ing. Zuzana Cílová, Ph.D.

I also thank to professor Pavel V. Krivenko for the opportunity to stay one month in the V.D. Glukhovskiy Scientific Research Institute for Binders and Materials in Kiev and for the possibility to visit the unique buildings in Mariupol. Next I thank to Dr. Fernando Pacheco-Torgal and professor José Barroso Aguiar for the fruitful internship at the University of Minho in Portugal and for the co-authorship in journal paper.

Further thanks belong also to the organizers of advanced courses which I took during the Ph.D. study, particularly to prof. Ing. Milan Jirásek, DrSc., prof. Ing. Jiří Šejnoha, DrSc., RNDr. Šárka Hošková, Ph.D., doc. Ing. Milena Pavlíková, Ph.D., prof. RNDr. Pavel Demo, CSc. and Ing. Olga Šolcová, CSc., DSc. Special thanks go to my colleagues from department Ing. Martin Horák and Ing. Jan Stránský for the help with FEM, programming and advanced mechanical models.

Especially I would like to appreciate the encouragement, support and patience of my parents, my wife Maruška and son Toníček.

The financial support from the Grant Agency of the Czech Technical University in Prague under grant No. SGS12/116/OHK1/2T/11 and from the Czech Science Foundation GAČR under projects GAP104/12/0102 and GA13-22230S are gratefully acknowledged.

Abstrakt

Předložená disertační práce se zabývá novými kompozitními stavebními materiály založenými na bázi alkalicky aktivovaného úletového popílku a Portlandského cementu s uhlíkovými nanovlákný.

Alkalicky aktivované materiály jsou používány déle než 60 let. Díky jejich intenzivnímu výzkumu v posledních desetiletích byly objasněny základní mechanismy alkalické reakce. Nicméně je zapotřebí dalšího výzkumu souvisejících fenoménů jako výkvětů či autogenního smrštění. V předchozí práci byl formulován kvantitativní model vývoje objemových fází v průběhu aktivace úletového popílku, nyní je představen mikromechanický model predikující vývoj elasticity v průběhu zrání N-A-S-H gelu. Elasticita alkalicky aktivovaných kompozitů je modelována pomocí víceúrovňové homogenizace založené na elastických vlastnostech jednotlivých fází a na objemovém zastoupení těchto fází. Youngův modul je předpovídán a ověřen na úrovni pasty a betonu. Jak již bylo zmíněno, výkvěty představují jeden z hlavních faktorů pro použitelnost alkalicky aktivovaných kompozitů. Vzhledem k tomu, že kvůli své dostupnosti je roztok NaOH obvykle používán jako alkalický aktivátor, je studována role sodíkových kationtů v N-A-S-H gelu. Experimenty loužením ukázaly téměř úplnou vyluhovatelnost sodíku z N-A-S-H gelu, což ukazuje na slabou vazbu sodíkových kationtů v gelu. Pomocí numerických simulací je určen difuzní koeficient pro transport sodíkových kationtů z N-A-S-H gelu a je predikován jejich transport z gelu. Posledním tématem v oblasti alkalicky aktivovaných materiálů je návrh, vývoj a charakterizace pěny z alkalicky aktivovaného popílku. Pasta z alkalicky aktivovaného popílku je napěněna hliníkovým práškem. Pěna je charakterizována pomocí mechanických vlastností, žáruvzdornosti, chemické odolnosti a tepelných vlastností.

Cementové kompozity s uhlíkovou nanovýztuží jsou vyrobeny z takzvaného cementového hybridního materiálu. Uhlíková nanovlákná jsou zde syntetizována přímo na povrch cementových zrn, čímž je dosaženo výborného rozptýlení uhlíkových nanovláken. Pro různé kompozice je změřena lomová energie na úrovni pasty a malty. Numerické simulace validují výsledky z experimentů a predikují lomové vlastnosti pro různé délky a různá objemová zastoupení uhlíkových nanovláken.

Klíčová slova: úletový popílek, alkalická aktivace, pěna, chemická odolnost, žáruvzdornost, mechanické vlastnosti, geopolymery, loužení, výkvěty, uhlíková nanovlákná, hybridní cementový materiál, mikromechanika, lomová energie.

Abstract

This doctoral thesis is devoted to novel composite building materials based on alkali activated fly ash and on Portland cement with carbon nanofibres.

Alkali activated materials have been utilized for more than 60 years. Due to extensive research in the last decades, basic mechanisms of the alkali reaction have been understood. However, further research is needed for related phenomenons, such as efflorescence or autogenous shrinkage. A quantitative model of phase evolution during fly ash activation was formulated previously, now a descriptive micromechanical model aiming at elasticity evolution during N-A-S-H gel hardening is introduced. The elasticity of alkali activated composites is predicted via multiscale homogenization using intrinsic elastic properties of particular phases and evolving volume fractions of the phases. The Young's modulus is calculated and validated for alkali activated fly ash paste and concrete. As mentioned above, efflorescence presents one of the governing factors for usability of the alkali activated fly ash-based composites. Since a solution of NaOH is usually used as an affordable alkali activator, the role of sodium cations in the N-A-S-H gel is examined. Leaching experiments proved almost full leachability of sodium from the N-A-S-H gel, which points to a weak alkali bond of the sodium cations in the N-A-S-H gel. A diffusion coefficient for the sodium cation transport is determined by numerical simulations and its transport from the N-A-S-H gel is predicted. The last stage in the field of alkali activated fly ash is a design, development and characterisation of an alkali-activated fly ash-based foam. The alkali activated fly ash paste is foamed by an aluminium powder. The foam is characterised in terms of mechanical properties, fire resistance, chemical resistance and thermal behaviour.

Cement composites with carbon nano-reinforcement are prepared from a so called cement hybrid material. The carbon nanofibres are directly synthesized on the surface of the cement grains and thus a perfect dispersion of the carbon nanofibres is guaranteed. Fracture energy for different compositions is measured at the level of cement paste and mortar. Numerical simulations validate the values obtained from experiments and predict fracture behaviour for composites with different volumes and lengths of carbon nanofibres.

Keywords: fly ash, alkali activation, foam, chemical durability, thermal resistance, mechanical properties, geopolymer, leaching, efflorescence, carbon nanotubes, cement hybrid material, micromechanics, fracture energy.

Contents

I	Integrating text	1
1	Introduction	1
1.1	Alkali activated materials	1
1.2	Carbon nanoreinforcement	4
1.3	List of thesis papers	5
2	Alkali activated fly ash	6
2.1	Source materials	6
2.2	Autogenous shrinkage	7
2.3	Efflorescence	9
2.4	Micromechanical modeling	10
2.5	Foam	12
3	Cement paste with carbon nano-reinforcement	16
3.1	Source materials	17
3.2	Fracture energy determination	18
3.3	Numerical simulations	18
4	Conclusions	20
5	References	21
6	List of publications	27
7	List of projects	28
7.1	Grant Agency of the Czech Technical University in Prague	29
7.2	Czech Science Foundation	29
II	Paper 1	30
III	Paper 2	42
IV	Paper 3	47

V	Paper 4	55
VI	Paper 5	65

Part I

Integrating text

1 Introduction

Alkali-activation generally presents a reaction between a strong alkaline liquid (e.g. a solution of sodium hydroxide and sodium metasilicate) and a solid aluminosilicate material (fly ash, metakaolin or blast furnace slag). The reaction product is called, depending on the authors, soil-cement [1], geopolimer [2], inorganic polymer [3], alkali-activated material or N-A-S-H gel [4–6], where the designation N-A-S-H gel describes the reaction product of alkali activation similar to the designation of cement hydration product C-S-H gel. The alkali activation is also known as a pozzolanic reaction from hydration of ordinary Portland cement (OPC) blended with secondary cementitious materials. The strongly alkaline calcium hydroxide, which is formed during the hydration of OPC, promotes the hydrolysis and dissolution of the Si–O group of blended aluminosilicate materials [7].

Production of Portland clinker is energy intensive process with relatively high CO₂ emissions, the decarbonation of limestone liberates 0.47 kg of CO₂ per one kg of clinker and the cement industry contributes to the CO₂ global emissions by around 7%. A theoretical energy consumption is 1758 kJ for calcination of one kg of clinker [8]. World cement production reached 4 billion tonnes in 2013, compared to 1.67 billion tons in 2000 [9]. To become more sustainable, the Portland clinker content in common cements was significantly reduced in last decades and secondary cementitious materials (e.g. fly ash or blast furnace slag) are utilized instead. Further reduction of Portland clinker becomes possible, when the strength of hydrated cement increases and thus less binder is needed to reach similar mechanical properties of the final composite. Also a full replacement of OPC in concrete comes into consideration when a new binder e.g. an alkali activated fly ash is utilized.

1.1 Alkali activated materials

The world annual production of fly ash (FA) is estimated to be around 600 million tons [10]. The current production of FA in the Czech Republic is about 6 million tons per year and it is estimated that only 20-30% of FA is reused, while the majority is stored on landfills/lagoons, which leads to an ecological burden. A successful utilization of fly ash by means of alkali-activation has been proved by several researchers [11–14]. The stability of alkali-activated fly ashes has been proved by Wallah and Rangan by long term tests



Figure 1: Residential buildings from alkali activated slag. Mariupol, Ukraine. Photo: author, May 2012.

[13]. On the other hand the mechanism of the alkali activation is not well described yet. Previously several chemistry-based models were introduced for deeper understanding of the alkali reaction, [15–17]. The basic mechanism of geopolymer formation was described by Fernández-Jiménez [18] and more advanced structural models were introduced by Y. Zhang [19] or J. L. Provis [20]. Since the elasticity presents one of the most developed frameworks of micromechanical models, a micromechanical model aiming at description of elasticity evolution during alkali activation of fly ash is formulated in Paper 1 [6]. The model is based on a quantitative description of a volumetric evolution of phases during alkali reaction and on intrinsic elastic properties of chemical phases on different scales [21]. Based on this model, the macroscopic elastic modulus during alkali-activation process is predicted on four scales, each scale taking into account relevant material phases [22], see Paper 2.

The alkali activated materials are known for more than 60 years. One of the first known large-scale application of alkali activated materials are residential buildings in Mariupol, Ukraine, see Fig. 1. The houses were built in 1960's from bricks made from alkali activated slag waste from Mariupol's iron and steel works (today Azovstal) with a design strength of 7.5 MPa. One brick from the buildings was examined in 2012. The compressive strength of 14 MPa was measured.

Despite a relative long history of alkali activated materials, a further research is needed for related phenomenons such as autogenous shrinkage or efflorescence. The efflorescence occurs under moisture gradient and presents one of the main disadvantages of alkali-activated materials. The weakly bound Na^+ cations from N-A-S-H gel are dissolved in water and transported to the surface. As the water evaporates the Na remains at the

surface creating Na carbonate [23, 24]. It has been proved, that the alkalis are able to be leached out without affecting the N-A-S-H gel skeletal structure and loss in strength, see Paper 4.

A presence of the strong alkali environment during activation of fly ash allows quite easy foam preparation. Similar to a well known technology of autoclaved aerated concrete (AAC), when a foaming agent is mixed with the fly ash paste an aerated closed-pore structure emerges. Between the most common foaming agents belongs: aluminium powder releasing hydrogen, hydrogen peroxide liberating oxygen or sodium carbonate releasing carbon dioxide.

A cement-based AAC is a well-known material in Europe since 1920's. A Swedish architect Johann Eriksson patented the AAC in 1923. The first AAC manufacturer in the world was established in Sweden in 1929, and the use of a fly ash (FA) as a filler was first mentioned in Lindman's patent in 1931 [25]. Aerated alkali-activated materials were mentioned by several authors previously. In 1987, Costopoulos patented a fly ash-based aerated concrete [26]; he used fly ash class C or class F blended with ordinary Portland cement. Prud'homme *et al.* [27, 28] synthesized a geopolymer-based foam from dehydroxylated kaolinite activated by a solution of potassium hydroxide and potassium silicate, where silica fume served as a blowing agent. Delair *et al.* [29] examined the durability of a kaolinite-based geopolymeric foam in aqueous media. Bell and Kriven [30] prepared foams from metakaolin-based geopolymer, and Cilla *et al.* [31, 32] created a open cell geopolymer foam.



Figure 2: A typical fly ash foam specimen.

An alkali-activated fly ash foam (FAF) is designed, synthesized, and optimized as a part of this work, see Paper 5. The FAF is a Portland cement-free, non-autoclaved foam, composed of alkali-activated fly ash and aluminium powder treated at temperatures below 80 °C. Hydrogen liberation during the activation process leads to a closed-pore network.

A laboratory-scale production process is elaborated and mixture compositions undergo optimization for their pore distribution and bulk density. A typical FAF specimen is shown in Fig. 2.

1.2 Carbon nanoreinforcement

The effort to create a stronger binder led to an attempt to reinforce the cement paste with carbon nanofibers/nanotubes. The carbon nanofibers (CNF) and carbon nanotubes (CNT) have previously found use in the manufacture of a high strength binder, as has been demonstrated for composites [33, 34] and specifically for cement pastes [35–37]. The CNT exhibit Young modulus from 180 to 588 GPa and tensile strength in the range between 2000 and 6140 MPa [38]. A uniform distribution of both CNT and CNF in cement composites is a challenging task, even within a small volume of cement paste. A simple powder mixing procedure leads to flocculation and improper dispersion of the CNF/CNT in the volume. For this reason, Sanchez and Ince proposed adding silica fume to cement to increase the dispersiveness of CNF [39]. A water dispersion of CNT/CNF with the help of surfactants is another widely-used method to introduce carbon nanomaterials into polymers [35]. However, most surfactants and additives prolong the cement setting and hardening times. Another approach, introduced A. Nasibulin *et al.*, uses CNT directly synthesized on the surface of cement grains creating a cement hybrid material (CHM) [40, 41]. The (CHM) can easily be mixed with conventional cement guaranteeing perfect dispersion of CNT in the cement matrix.

The effect of carbon reinforcement in the cement paste is reported inconsistently across the literature. It has been reported that even a small mass fraction of CNT (0.005) helped to increase flexural strength by 22% [37] and on the other hand a decrease of more than 30% in compressive strength has been mentioned [35]. To show the effect of CNT reinforcement from a mechanical point of view, series of experiments with the cement hybrid material are performed and micromechanical simulations are executed, see Paper 3.

This thesis consists of four journal papers and one peer-reviewed conference contribution. Please note that since all the papers are self-contained, the thesis may contain repetitions.

1.3 List of thesis papers

The papers 1,3 and 4 are already published in journals, the Paper 5, which is fundamental for the thesis, is accepted for publication. The papers are listed in a chronological order. The number in parentheses is my contribution to the paper.

- **Paper 1**, ISI Journal, IF 2.3, (20%), [6]
Vít Šmilauer, Petr Hlaváček, František Škvára, Rostislav Šulc, Lubomír Kopecký, Jiří Němeček: Micromechanical multiscale model for alkali activation of fly ash and metakaolin, *Journal of Materials Science*, 2011, 46(20), 10 citations,
- **Paper 2**, Peer-reviewed conference paper, (30 %), [22]
Petr Hlaváček, Vít Šmilauer, Rostislav Šulc, Lubomír Kopecký, František Škvára: Elastic properties of geopolymer concrete based on fly-ash, *Novel Developments and Innovation in Cementitious Materials*, 31st Cement and Concrete Science Conference, 2011, no citation,
- **Paper 3**, Peer-reviewed Journal in SCOPUS, SNIP 0.27, (40%), [42]
Vít Šmilauer, Petr Hlaváček, Pavel Padevět: Micromechanical analysis of cement paste with carbon nanotubes, *Acta Polytechnica*, 2012, 52(6), 1 citation,
- **Paper 4**, ISI Journal, IF 0.43, (23%), [43]
František Škvára, Vít Šmilauer, Petr Hlaváček, Lubomír Kopecký, Zuzana Cílová: A weak alkali bond in (N, K)–A–S–H gels: Evidence from leaching and modeling, *Ceramics-Silikáty*, 2012, 56(4), 4 citations,
- **Paper 5**, ISI Journal, *in Press*, IF 2.3, (80%) [44]
Petr Hlaváček, Vít Šmilauer, František Škvára, Lubomír Kopecký, Rostislav Šulc: Inorganic foams made from alkali-activated fly ash: mechanical, chemical and physical properties, *Journal of the European Ceramics Society*, 2014, *in Press*, no citation.

2 Alkali activated fly ash

Wider application of alkali activated fly ash (AAFA) is restrained especially by the need of liquid activator, by the efflorescence and by a slow reaction process. It was found previously that increasing curing temperature from 20°C to 80°C speeds up the reaction by factor of 380 [45], so a heat curing is usually applied.

2.1 Source materials

The fly ash class F from the Opatovice brown coal power plant, Czech Republic (Blaine 210 m²/kg) is used as the source material for alkali-activation, see Tab. 1 for the chemical composition. Fig. 3 shows the FA particle size distribution.

Table 1: Chemical composition of fly ash (wt %).

	SiO ₂	Al ₂ O ₃	Fe ₂ O ₃	CaO	K ₂ O	TiO ₂
Fly ash	51.9	32.8	6.3	2.7	2.12	1.89

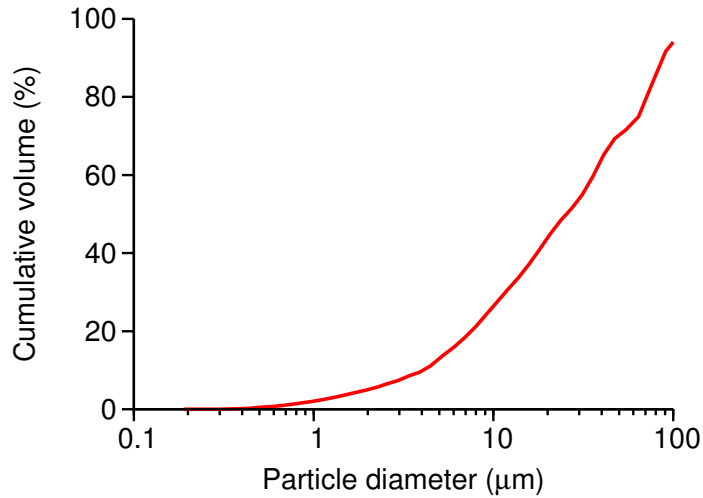


Figure 3: The particle size distribution curve of fly ash used in experiments.

Sodium hydroxide pellets dissolved in sodium metasilicate constitute the alkali activator. Composition of AAFA binder was optimized previously by R. Šulc from our research group [46]. The final composition and compressive strength of AAFA paste is given in Tab. 2. Tab. 3 shows a typical composition of AAFA based concrete [47].

The aluminum metal powder from Albo Schlenk Inc., Bojkovice, Czech Republic, product type 76013 (average particle diameter by mass, $d_{50} \approx 35 \mu\text{m}$), is used as an air entraining agent in the foam production process.

Table 2: Composition and compressive strength of AAFA paste mix. Thermal curing 12 hours at 80°C.

Sample label	FA/Solid	Liquid/Solid	NaOH/Solid	Sodium water glass/Solid	f_c [MPa]
AAFA	1.0	0.45	0.07	0.38	65.7

Table 3: Typical composition of AAFA concrete mix per one m³, data from T. Strnad [47].

	Mass [kg]	Density [kg/m ³]	Volume [m ³]
Fine aggregates	695	2653	0.257
Coarse aggregates	1183	3197	0.363
AAFA paste	597	1843	0.324
Added water	51	998	0.051

2.2 Autogenous shrinkage

Autogenous shrinkage presents one of the insufficiently described properties of alkali activated materials.

The autogenous shrinkage of AAFA-based composite is calculated from measured volume changes of AAFA paste during alkali activation at ambient temperature. The data are fit with analytical shrinkage models and recalculated to the levels of mortar and concrete and compared with known autogenous shrinkage of ordinary Portland cement (OPC) based materials.

The autogenous shrinkage of a cement paste is defined as the macroscopic volume change with zero moisture transport from/to a specimen [48]. It is calculated from the measured length changes of bellows filled up with the AAFA paste placed in a climatic chamber. The length of bellows was measured every 5 minutes during maturing. The autogenous shrinkage $\varepsilon_{as}(t_n)$ in the time step t_n is determined as:

$$\varepsilon_{as}(t_n) = \frac{l(t_0) - l(t_n)}{l(t_0)}, \quad (1)$$

where $l(t_0)$ is the initial length of the specimen and $l(t_n)$ is the length at given time step. The measured autogenous shrinkage is fitted using functions given in FIB Model Code 2010 [49], see Eq. (2) and using adapted B3 model [50], see Eq. (3). The FIB Model Code reads

$$\varepsilon_{as}(t) = \varepsilon_{\infty} \left(1 - e^{-0.2\sqrt{t}}\right), \quad (2)$$

where $\varepsilon_{as}(t)$ is the autogenous shrinkage at given time, and ε_{∞} represents the final autogenous shrinkage at infinite time. This model is originally formulated for autogenous shrinkage of OPC based concrete. Another function fitting shrinkage is adapted from B3 model for mean shrinkage strain in the cross section:

$$\varepsilon_s(t, t_0) = -\varepsilon_{\infty} \tanh \sqrt{\frac{t - t_0}{\tau_{sh}}}, \quad (3)$$

where $\varepsilon_s(t, t_0)$ presents the shrinkage at given time t , t_0 is the shrinkage starting time, ε_{∞} presents the final shrinkage at infinite time and τ_{sh} is the shrinkage half-time.

Total shrinkage is split to plastic and autogenous parts. Plastic shrinkage is believed to occur up to the final set. In the early stage, a material is still plastic and the skeleton is under formation thus no stress is caused by the early age shrinkage.

The autogenous shrinkage starts after final set, which occurs at ambient temperature approx. 240 hours after mixing. The autogenous shrinkage on the AAFA paste 15 days after the final set was found as 0.89 mm/m, see Fig. 4. Shrinkage of mortar and concrete is recalculated from the shrinkage of the paste and from the volume fractions of aggregates (Tab. 3) using data published by G. Pickett [51]. The B3 model is calibrated with the

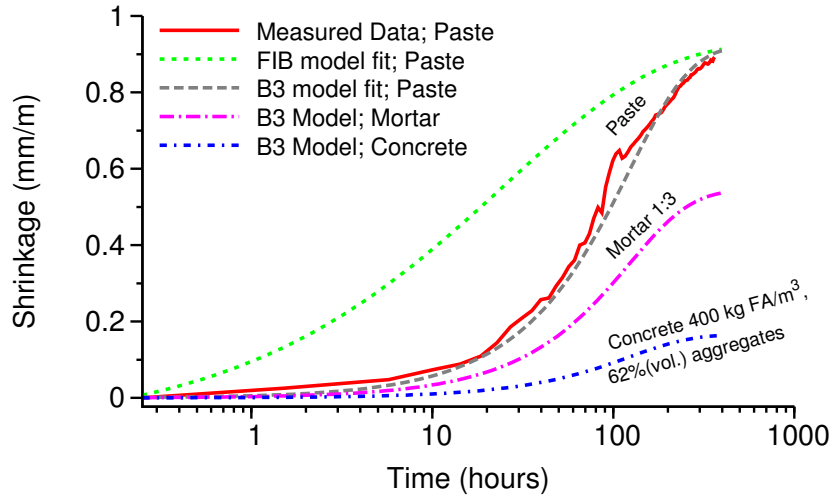


Figure 4: Autogenous shrinkage of AAFA composites, measured data on paste level, analytical fit and prediction of shrinkage on the level of mortar and concrete. Zero time is the final set of AAFA paste.

experimental data and it gives for AAFA concrete at 30 days after the final set autogenous shrinkage in the range 0.05-0.2 mm/m. This corresponds well to a typical value for an OPC-based concrete at the age of one month, which is, according to Neville, between 0.04 mm/m for a regular concrete and 0.7 mm/m for a high-performance concrete [7].

2.3 Efflorescence

The efflorescence presents one of the aesthetic restraints of AAFA. Since the alkali reaction runs in a strong alkaline environment, liquid NaOH presents the simplest and cheapest way to reach such conditions. The mechanical properties of AAFA composites based on NaOH were optimized previously, but the chemical bond of the Na⁺ cations in the N-A-S-H gel remained unknown.

The transport of Na ions was preliminarily studied in my M.Sc. thesis [45] and an advanced analysis is done in Paper 4. Two different leaching experiments were performed on the Institute of Chemical Technology in Prague. In the first experiment, a 40×40×160 mm beam from AAFA paste was immersed into 600 ml of deionized water, which was changed every 24 hours and the concentration of Na₂O in the water bath was measured. The loss of Na⁺ from the body in time was evaluated from the measured concentrations in the water bath. In the another experiment, matured AAFA paste sample was crushed under the size of 0.5 mm and leached 150 days in deionized water, which was changed between 1 and 3 days. The content of Na was determined using X-ray fluorescence analysis. Only 2% of Na remained in the paste after leaching, which proves the almost full leachability of Na from the AAFA.

A 3D leaching simulation reproducing the loss of Na₂O in the specimen is performed in OOFEM package [52]. A linear isotropic material model for transport problems is used. The diffusion coefficient is assumed to be constant and independent from concentration, although it is known, that the water vapor diffusivity for matured concrete decreases by a factor of 20 [53]. The linear diffusion equation reads

$$\frac{\partial c}{\partial t} = \nabla \cdot (D \nabla w), \quad (4)$$

where c is the concentration, t is time, and D is the searched diffusion coefficient for Na transport in AAFA.

Fig. 5 left shows measured concentrations of Na₂O in the water bath and results from simulations. The linear diffusion coefficient is found as $1.6 \cdot 10^{-7} \text{ m}^2/\text{day}$.

The Na₂O concentration profile from the sample surface is verified independently by EDX analysis. Surface areas of the sample are cut from the 28 day-leached AAFA prisms and exposed to an EDX line analysis. Analytical solution of the linear diffusion equation leads to [53]

$$c(x, t) = c_{init} \operatorname{erf} \frac{x}{2\sqrt{Dt}} \quad (5)$$

where c_{init} is the initial concentration of Na₂O in the body, $c(x, t)$ is the concentration at a given time and a position x from the surface, D represents the constant diffusion

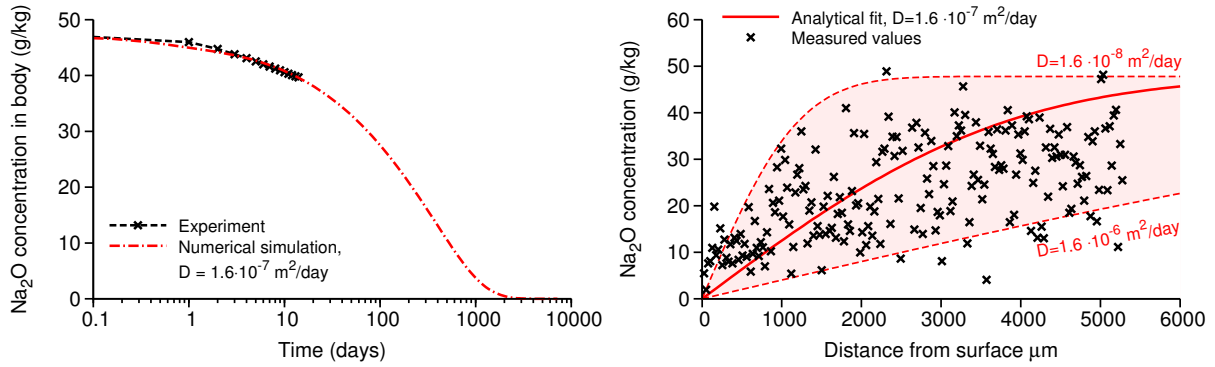


Figure 5: Concentrations of Na_2O in the AAFA paste specimens. The prism $40 \times 40 \times 160$ mm was leached in deionized water which was regularly replaced.

coefficient and t is time. The feasible lower and upper bounds for the linear diffusion coefficient are depicted on Fig. 5 right.

The Na leaching can be stopped by exposing activated fly ash to temperatures over 600°C . This could be explained by Na embedding inside newly formed glass.

2.4 Micromechanical modeling

To contribute to the understanding of evolution of mechanical properties during AAFA hardening, a micromechanical model aiming at description of elasticity evolution during alkali activation of fly ash is formulated.

A volumetric model of phase evolution during alkali activation of fly ash and a preliminary micromechanical analysis of N-A-S-H gel was previously published in my M.Sc. thesis [45]. However, a detailed analysis of the elastic properties of AAFA composites shows, that the micromechanical models overestimate the elasticity of AAFA concrete. The inconsistency is explained with introduction of cracks in the alkali-activated paste, which is quantified via a damage parameter, see Paper 1 and Paper 2.

The elastic properties of AAFA composites are described on N-A-S-H gel level, AAFA paste level and on the level of mortar and concrete. The Young's modulus of the N-A-S-H gel was determined by nanoindentation, as 17.72 GPa after 98 days at ambient temperature corresponding to the degree of fly ash reaction 0.437 [54].

Effective elastic properties on the other levels (AAFA paste, mortar and concrete) are obtained through averaging over the relevant material phases, see Tab. 4. The homogenization schemes consider isotropic spherical inclusions perfectly bonded with a matrix. The estimation of effective bulk and shear moduli of composite can be formulated for

Mori-Tanaka method and self-consistent scheme [55] as:

$$k_{eff} = \frac{\sum_i f_i k_i \left[1 + \frac{3k_0}{3k_0 + 4\mu_0} \left(\frac{k_i}{k_0} - 1 \right) \right]^{-1}}{\sum_i f_i \left[1 + \frac{3k_0}{3k_0 + 4\mu_0} \left(\frac{k_i}{k_0} - 1 \right) \right]^{-1}}, \quad (6)$$

$$\mu_{eff} = \frac{\sum_i f_i \mu_i \left[1 + \frac{6k_0 + 12\mu_0}{15k_0 + 20\mu_0} \left(\frac{\mu_i}{\mu_0} - 1 \right) \right]^{-1}}{\sum_i f_i \left[1 + \frac{6k_0 + 12\mu_0}{15k_0 + 20\mu_0} \left(\frac{\mu_i}{\mu_0} - 1 \right) \right]^{-1}}. \quad (7)$$

For a given i^{th} phase, f_i represents the volume fraction, k_i is the bulk modulus and μ_i is the shear modulus. A reference medium is described as the 0^{th} phase.

Table 4: Intrinsic elastic properties used in the homogenization of Young’s modulus.

Material	Young’s modulus [GPa]	Poisson ratio [-]
Fly ash	105	0.2
N-A-S-H gel	17.72	0.2
Voids	0.001	0.001
Fine aggregates	60	0.2
Coarse aggregates	70	0.2

Two homogenization schemes were utilized in the simulations. First one, the Mori-Tanaka method [56], deals with a continuous reference matrix. All inclusions are embedded inside this reference medium. Aligning k_0, μ_0 in the Eqs. (6), (7) with a specific phase k_i, μ_i leads to the Mori-Tanaka method. This method was used for the levels of N-A-S-H gel, mortar and concrete.

The another one, self-consistent scheme of Budiansky and Hill [57], is an implicit scheme for composites with no dominant phase. In this case the reference phase points back to the homogenized medium itself, which leads to $k_0 = k_{eff}$ and $\mu_0 = \mu_{eff}$ after several iterations. The self-consistent scheme is suitable especially for the AAFA paste level. Due to small differences in the volume fractions no dominant phase exists on this level.

In the experiments, secant elastic moduli of paste and concrete samples were measured several times during slow hardening under ambient curing conditions. The Young’s modulus was obtained from Hooke’s law:

$$E = \frac{\Delta\sigma}{\Delta\varepsilon} = \frac{\sigma_a - \sigma_b}{\varepsilon_a - \varepsilon_b}, \quad (8)$$

where σ_a is upper loading limit, approximately one third of compressive strength and σ_b

is the lower loading limit standardized as 0.5 MPa, ε_a , ε_b are the corresponding measured strains.

The experiments on the concrete level show lower elastic moduli compared to the simulations, see Fig. 6. This demonstrates stiffness reduction of paste caused by formation of shrinkage cracks, which can be quantified by a damage parameter. The damage parameter is defined as

$$D = 1 - \frac{\tilde{E}}{E}, \quad (9)$$

where \tilde{E} represents the Young's modulus of material with cracks and E is the theoretical Young's modulus of undamaged material.

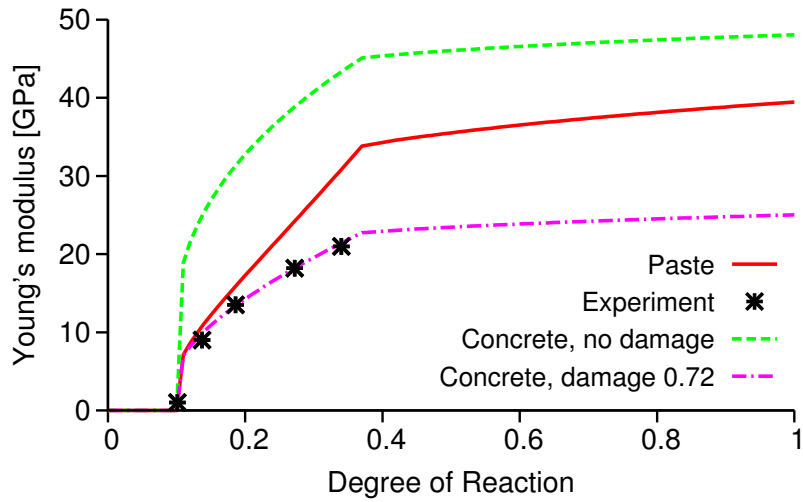


Figure 6: The development of elastic modulus during hardening of AAFA paste and concrete.

2.5 Foam

The synthesis and characterisation of the foam produced from alkali activated fly ash (FAF) is the one of the major parts of this thesis. The FAF laboratory-scale production and characterisation is described in the Paper 5. Fig. 7 shows a typical FAF specimen after a fire resistance test.

The fly ash-based foam is produced from the AAFA paste blowed up with an aluminum powder. The reaction between the Al metal powder and the alkaline activator proceeds quickly, approximately as



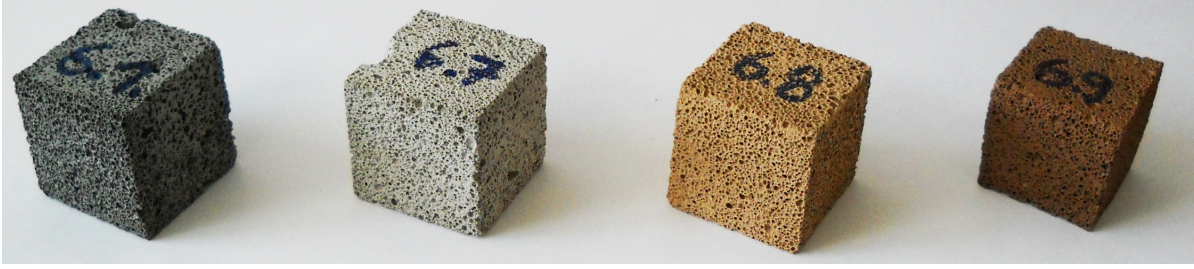


Figure 7: Alkali activated fly ash foam samples after fire-resistance test (reference, 500°C, 800°C, 1100°C).

Due to the speed of the reaction, a hand stirring took place directly in a mold. To achieve a proper pore distribution, the aluminium powder is first mixed with the fly ash powder in dry state and the liquid activator is added subsequently. A mixture optimization leads to a final composition, which is given in the Tab. 5. Experiments and micromechanical simulations proved that reasonable bulk densities are in the range of 400 to 800 kg/m³.

Table 5: Fly ash foam composition (the listed masses fill approximately the volume of 100 ml).

Mixture	FA (g)	Liquid/solid (-)	NaOH (g)	Na metasilicate (g)	Al (g)	Bulk density (kg/m ³)
FAF	50	0.38	2.9	16.1	0.045	671

The FAF is characterized by means of its compressive and flexural strength, thermal conductivity and capacity, exposure to high temperatures, performance in chemically aggressive environments and 2D morphology. In comparison to traditional autoclaved aerated C-S-H-based materials, FAF retains exceptionally good fire resistance and high chemical durability, exhibits a rather closed-pore network, and requires temperatures below 80°C for curing without the need for autoclaving. Tab. 6 shows the measured physical properties of FAF compared with traditional AAC. The values always represent an average of at least four measurements.

Resistance to chemically aggressive environments is proved by a long-term exposure to solutions of Na₂SO₄, MgSO₄, NaCl, H₂SO₄ and HCl at ambient temperature. The results show that the most severe degradation of FAF occurs in HCl and H₂SO₄ solutions, see Tab. 7.

Effective Young’s modulus provides useful information on the microstructure of a material. Especially, it is possible to determine the interconnectedness of phases and validate their intrinsic elastic properties. A 2D scan of FAF (see Fig. 8) gives a starting microstructure for a numerical analysis exploring the role of porosity on elasticity. The

Table 6: Data on fly ash foam (FAF) and traditional autoclaved aerated concrete (AAC) [7, 58].

		FAF	AAC 600	AAC 675
Bulk density	ρ^b (kg/m ³)	671	600	675
Compressive strength	f_{cm} (MPa)	6.0	4.5	6.3
Flexural strength	f_{tm} (MPa)	1.0	0.85	1.0
Thermal conductivity	λ (W/m/K)	0.145	0.160	0.180
Thermal capacity	c_p (J/kg/K)	1089	-	-

Table 7: Relative compressive strength ($f_{cm,r}$), relative Young’s modulus (E_r), and relative mass (m_r) of fly ash foam after 360 days of exposition to chemical aggressive environments.

	Na ₂ SO ₄	MgSO ₄	NaCl	H ₂ SO ₄	HCl
$f_{cm,r}$	0.86	0.74	0.45	0.20	0.20
E_r	0.72	0.79	0.49	0.03	0.04
m_r	0.96	0.98	1.00	0.75	0.76

porosity of FAF can be divided into two groups. The first one represents small micropores ($< 100 \mu\text{m}$), which reside in the activated fly ash paste. The second group are macropores ($> 100 \mu\text{m}$) creating the FAF pore structure. The macroporosity of the specimens ϕ^{macro} is calculated from a known bulk density of the paste $\rho_{\text{paste}}^b = 1752 \text{ kg/m}^3$ [6] and the measured FAF bulk density ρ_{foam}^b

$$\phi^{\text{macro}} = 1 - \frac{\rho_{\text{foam}}^b}{\rho_{\text{paste}}^b}. \quad (11)$$

The 2D scan is converted to 256 grayscales and 13 meshes are generated with macroporosities in the range of 0.50–0.74 in 0.02 increments. A burning algorithm explores the paste connectedness within the images and eliminates disconnected parts from the edges. The ratio of the pixels that remains after the burning algorithm to the original amount is called solid percolation. The solid percolation threshold represents the macroporosity where no path between the top and the bottom exists. In our particular case, this corresponds to a macroporosity of 0.72, which equals to the FAF bulk density of 490 kg/m^3 , see Fig. 9. However, the solid percolation threshold in 3D would be higher due to out-of-plane solid paths [59]. This result is in agreement with the lowest bulk density of 400 kg/m^3 measured in our experiments.

The burnt images serve for creating a mesh with 500×500 elements and a finite element size of $40 \mu\text{m}$. Since the porosity is not meshed, the resulting mesh contains between

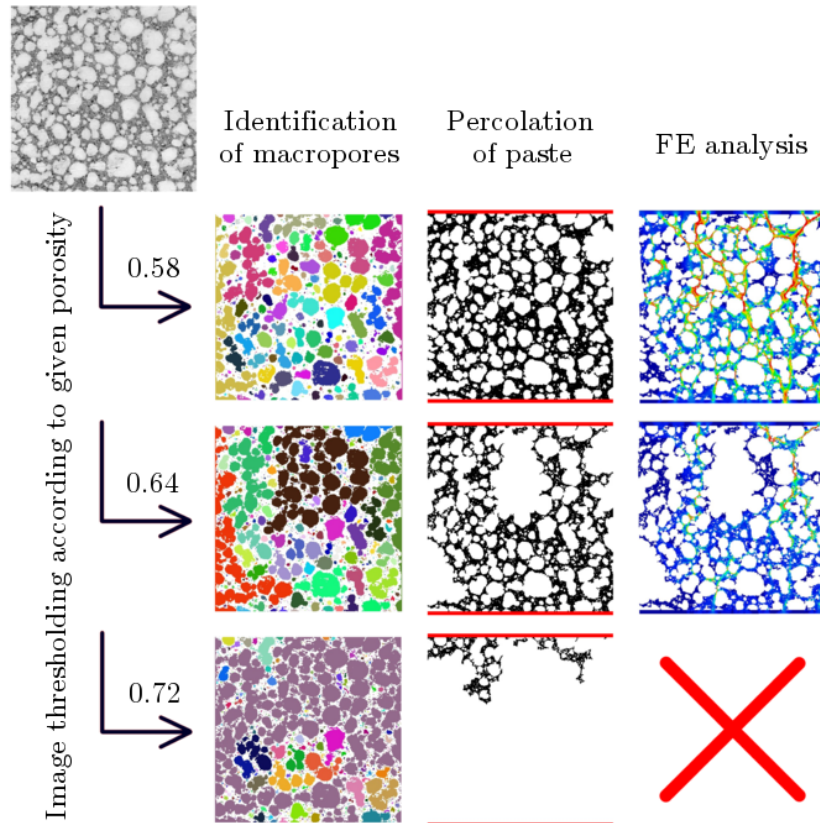


Figure 8: Image processing of fly ash foam: thresholding, identification of pores, percolation and stress σ_{22} .

70 000 and 130 000 finite linear quadrilateral elements. The horizontal edges are loaded by kinematic uniform boundary conditions in the form of a prescribed displacement, while the vertical edges are kept free. The role of macroporosity to the effective Young's modulus is shown in the Fig. 9.

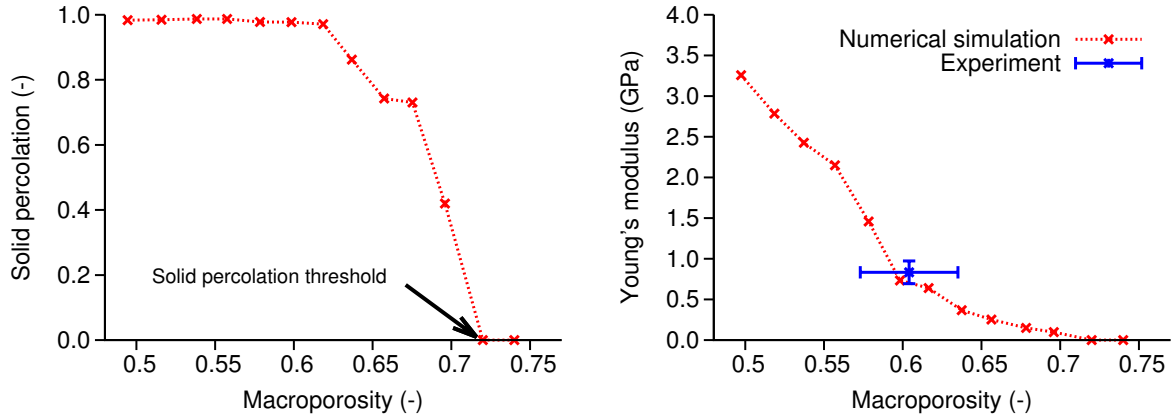


Figure 9: Solid percolation (left) and Young's modulus (right) of fly ash foam for different macroporosities.

3 Cement paste with carbon nano-reinforcement

Carbon nanofibers/nanotubes (CNT/CNF) seemed to improve mechanical strength and fracture energy of cement-based composites [37], but various authors report inconsistent data about the effect of the carbon nanoreinforcement. For this reason the micromechanical simulations are carried out to shed a light on their performance. In addition, small scale experiments help us to calibrate the numerical models on CNT/CNF reinforced paste with variable carbon volume content. The effect of CNT/CNF length, amount and clustering is studied and analyzed, see Paper 3.

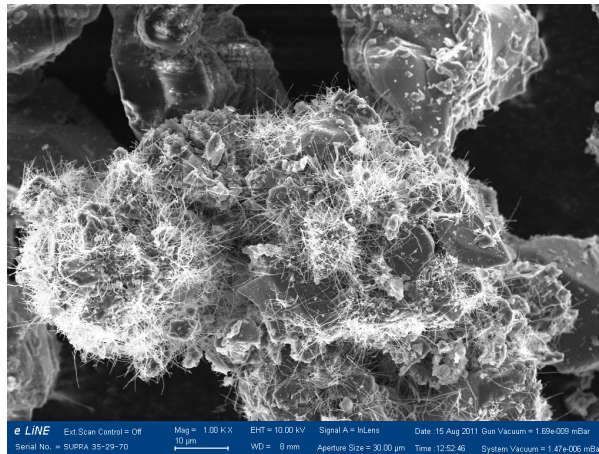


Figure 10: Cement grain with surface-synthesized CNT, image wide $112 \mu\text{m}$. Image by K. Hruška, Institute of Physics ASCR, Prague.

Cement with surface-synthesized carbon nanotubes/nanofibers (cement hybrid material - CHM) is used as a CNT/CNF source. Fig. 10 shows the SEM image of the CHM, the Portland cement particles are completely covered with the carbon nanofibers.

Table 8: Chemical composition of OPC and CHM wt(%).

	CaO	SiO ₂	Fe ₂ O ₃	Al ₂ O ₃	MgO	Carbon
OPC	65.6	19.0	3.5	5.0	1.1	-
CHM	44.2	14.4	2.8	1.5	1.4	30.0

Table 9: Five batches with different CNT/CNF amount used in the experiments. In all mixes superplasticizer Glenium ACE 40 is used in the amount of 0.2% to the binder mass.

Designation	CEM I (g)	CHM (g)	Water (g)	Carbon/paste
0% CNT	234.0	0	81.9	0 vol %
0.88% CNT	225.81	8.19	81.9	0.88 vol %
1.75% CNT	217.62	16.38	81.9	1.75 vol %
3.46% CNT	201.24	32.76	81.9	3.46 vol %
7.31% CNT	163.8	70.2	81.9	7.31 vol %

3.1 Source materials

Ordinary Portland cement CEM I 42.5 R originated from Mokra, Czech Republic, is utilized as the source material for all specimens. Specific Blaine surface has the value of 355 m²/kg, see Tab. 8 for the chemical composition.

The cement hybrid material (CHM) was synthesized by L. Nasibulina’s group from AALTO University (Finland) by the chemical vapor deposition method [41]. The Portland sulfate-resistant cement (CEM I 42.5N) was used as the base for CNF/CNT growth. The chemical composition is given in Tab. 8.

The CNF/CNT growth runs at temperature about 600°C in fluidized bed reactor where acetylene is utilized as the main carbon source for its low decomposition temperature and affordability. The CNT typically grown on the cement particles are 30 nm in diameter and up to 3 μm in length [60], the specific surface area of CNT is about 10 – 20 m²/g. CNT exhibit elastic modulus in the range of 180 - 588 GPa and tensile strength from 2 to 6 GPa [37, 60].

Tab. 9 shows the composition of the mixes used in the experiments. Samples sized 13 × 13 × 80 mm were cut on diamond saw from 40 × 40 × 160 mm beams.

3.2 Fracture energy determination

The fracture energy, G_f , is determined according to the RILEM standard [61]. See Fig. 11 for layout of the experiment. The three-point bending test under displacement-controlled regime gives access for the load-displacement curve. The work of external force P could be calculated as

$$W_f = \int_0^{u_f} P du \quad (12)$$

where u is the load-point displacement and u_f is the final displacement at which the load equals to zero. The average fracture energy in the ligament, according to the RILEM standard, is defined as

$$G_f = \frac{W_f}{b(d - a_0)} \quad (13)$$

where b presents the thickness of the beam, d the beam depth and a_0 is the depth of the notch. The support span L was set to 50 mm.

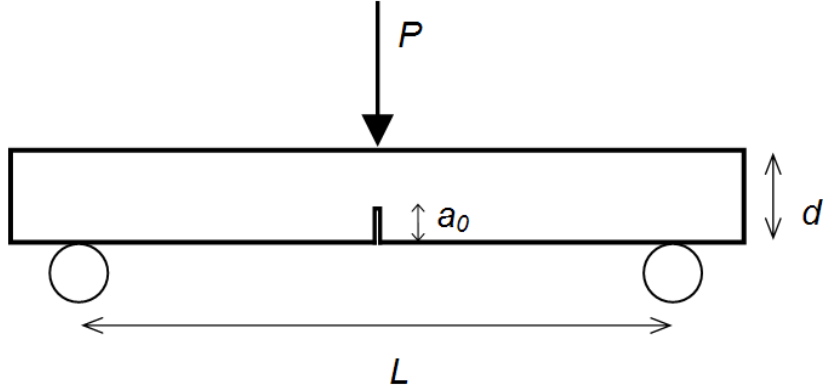


Figure 11: Fracture energy determination, scheme of the three point bending test.

Fig. 12 shows the measured fracture energy of CNT reinforced cement pastes with various amount of CNT in the mixture. The average CNT length is $2.5 \mu\text{m}$. The CHM samples exhibit almost no increase in the fracture energy, even if more than 3% (vol.) of CNT is utilized.

3.3 Numerical simulations

The numerical simulations were carried out in the OOFEM package [52]. A $100 \times 100 \mu\text{m}$ 2D microstructures of hardened cement paste generated with CEMHYD3D were used for reproducing the fracture energy of CNT-free and CNT-reinforced cement pastes. The Fig. 13 shows the 2D microstructure used in simulations. Four phases were taken into account: porosity, clinker, hydration products and CNT, the mechanical properties are

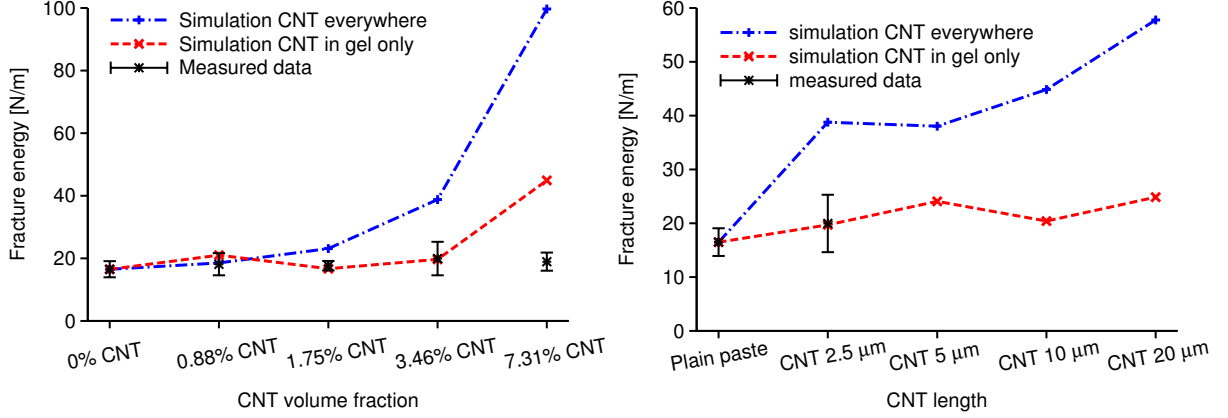


Figure 12: Fracture energy of cement paste with various amount and length of CNT/CNF, CNT length set to $2.5 \mu\text{m}$ (left) and CNT amount set to 3.46% (right).

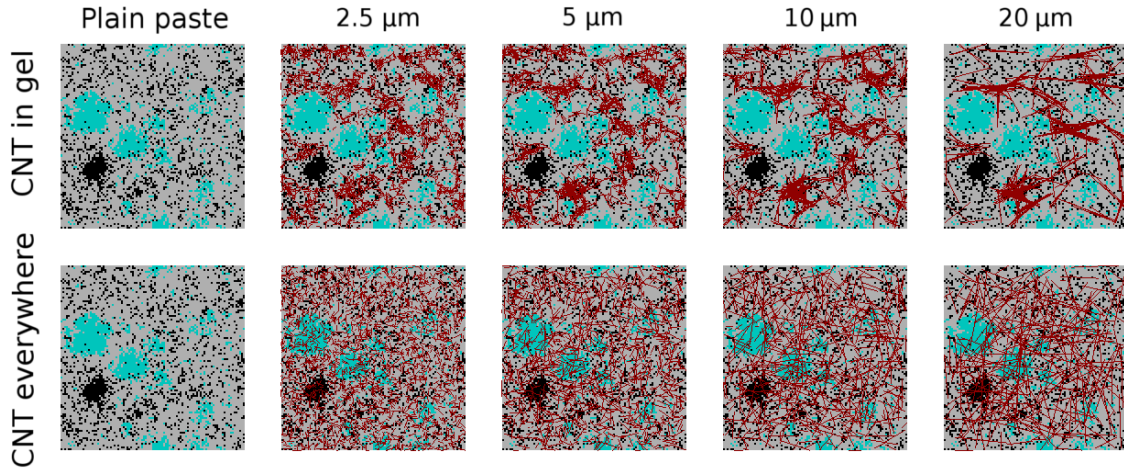


Figure 13: Comparison of different length of CNT/CNF, ideally dispersed and clustered in the C-S-H gel and voids. CNT amount 3.46% (vol). Black porosity, gray products, light blue unreacted cement and red CNT.

given in Tab. 10. The fracture energy and tensile strength of hydration products (mainly the C-S-H) were deduced from experimental data and simulation on plain pastes. The final parameters (5.58 MPa tensile strength and 12.9 N/m fracture energy) are in good correspondence with values given in the literature [37, 62]. The properties of CNT were estimated from recent results [21], the CNT cross-section was considered as $50 \text{ nm} \times 1 \mu\text{m}$ which in fact represents a bundle of CNT nanotubes.

Isotropic damage material model is assigned to all components (Tab. 10), see OOFEM documentation [52] or Šmilauer et al. [42] for a deep description of the material model.

Fig. 13 shows the microstructure of cement composite used in the numerical simulations. Two different CNT distributions were taken into account:

Table 10: Elastic and fracture properties of the components used in the numerical simulations.

Phase	E (GPa)	ν	f_t (MPa)	G_f (N/m)
Porosity	0.2	0.02	-	-
Clinker	135	0.3	-	-
Products	21.7	0.24	5.58	12.9
CNT	231	0.14	3000	200

- CNT randomly distributed in whole microstructure - “CNT everywhere”, in reality impossible due to the initial volume occupied by the unhydrated cement particles,
- CNT in clusters, random distribution of CNT in hydration products and voids - “CNT in gel”, no CNT in the cement grains.

Fig. 12 shows that the clustering of CNT is a crucial factor for the nanoreinforcement effectiveness. Increasing the length of perfectly dispersed CNT leads to a high increase of fracture energy, but the clustering promotes formation of cracks around heavily reinforced zones and the CNT reinforcement is thus ineffective. The difference between the numerical simulation and measured value for sample with 7.31% of CNT in the mixture (Fig. 12) could be explained by insufficient quality of the sample used in experiment caused by a high volume of CNT which reduced the workability.

4 Conclusions

This doctoral thesis is devoted to novel composite building materials based on alkali activated fly ash and on Portland cement with carbon nanoreinforcement.

The main results of this thesis can be summarized as:

- Determination of autogenous shrinkage of alkali activated fly ash paste cured under ambient temperature. The autogenous shrinkage of AAFA-based composite is calculated from measured volume changes of AAFA paste during alkali activation at ambient temperature. The data are fitted with analytical shrinkage models and recalculated to the levels of mortar and concrete and compared with known autogenous shrinkage of ordinary Portland cement (OPC).
- Identification of Na diffusion coefficient and prediction of Na transport from the alkali activated fly ash paste. Since the Na efflorescence presents one of the governing factors for usability of the alkali activated fly ash-based composites, leaching

experiments and numerical simulations proved almost full leachability of sodium from the N-A-S-H gel. The efflorescence of AAFA can be stopped exposing the activated fly ash to temperatures over 600°C. The Na is embedded inside newly formed glass and thus no transport occurs.

- Validation of elasticity of the alkali activated fly ash composites by micromechanical simulations and homogenization techniques. The elastic properties are described on N-A-S-H gel level, AAFA paste level and on the level of mortar and concrete. The Young's modulus of the N-A-S-H gel was determined previously by nanoindentation, as 17.72 GPa. Effective elastic properties on the other levels (AAFA paste, mortar and concrete) are obtained through averaging over the relevant material phases.
- Design, synthesis and characterisation of a foam made from alkali activated fly ash paste blowed up with an aluminium powder. The fly ash foam is characterized by means of its compressive and flexural strength, thermal conductivity and capacity, exposure to high temperatures, performance in chemically aggressive environments, and 2D morphology. In comparison to traditional autoclaved aerated C-S-H-based materials, the fly ash foam retains exceptionally good fire resistance and high chemical durability, exhibits rather a closed-pore network, and requires temperatures below 80°C for curing without the need for autoclaving.
- Evaluation of the effect of carbon nanoreinforcement in a cement paste. The study of cement paste with carbon nanofibres have proven that the clustering and improper dispersion of carbon nanofibres are the crucial factors for improvement of fracture behaviour of the composite material. Our results from the experiments show almost no improvement of the fracture energy. The micromechanical simulations have shown that increasing the amount of carbon nanofibres has negligible effect to the fracture energy of the cement composite since the ideal dispersion of the nanofibres is in reality hardly possible. The volume of the microstructure which is at the beginning of the hydration occupied by the cement particles could never be reinforced. Thus the carbon nanofibres are ineffective, since they are shorter than an average cement grain size. In this regard, improvement of the mechanical properties could happen through longer fibres, estimated 50 μm in length at least.

5 References

- [1] V. D. Glukhovskiy, *Soil Silicates (Gruntosilikaty)*. Kiev, Budivelnik publisher, USSR, 1959.

- [2] J. Davidovits, “Synthesis of new high-temperature geo-polymers for reinforced plastics/composites,” in *Proceedings of PACTEC’79, Society of Plastic Engineers*, pp. 151–154, 1979.
- [3] J. Van Jaarsveld, J. Van Deventer, and G. Lukey, “The effect of composition and temperature on the properties of fly ash-and kaolinite-based geopolymers,” *Chemical Engineering Journal*, vol. 89, no. 1, pp. 63–73, 2002.
- [4] A. Palomo, M. W. Grutzeck, and M. T. Blanco, “Alkali-activated fly ashes. A cement for the future,” *Cem. Concr. Res.*, vol. 29, pp. 1323–1329, 1999.
- [5] A. Fernández-Jiménez and A. Palomo, “Composition and microstructure of alkali activated fly ash binder: Effect of the activator,” *Cem. Concr. Res.*, vol. 35, pp. 1984–1992, 2005.
- [6] V. Šmilauer, P. Hlaváček, F. Škvára, R. Šulc, L. Kopecký, and J. Němeček, “Micro-mechanical multiscale model for alkali activation of fly ash and metakaolin,” *J Mater Sci*, vol. 46, no. 20, pp. 6545–6555, 2011.
- [7] A. M. Neville, *Properties of Concrete*. John Wiley & Sons, Inc., 1997.
- [8] H. F. W. Taylor, *Cement Chemistry*. Academic Press, New York, 1990.
- [9] The European Cement Association, “Activity Report 2013,” report, CEMBUREAU, Brussels, Belgium, May 2014.
- [10] M. Ahmaruzzaman, “A review on the utilization of fly ash,” *Progress in Energy and Combustion Science*, vol. 36, no. 3, pp. 327–363, 2010.
- [11] C. Shi, P. V. Krivenko, and D. Roy, *Alkali-activated cements and concretes*. Taylor & Francis, first ed., 2006.
- [12] A. Fernandez-Jimenez and A. Palomo, “Characterisation of fly ashes. Potential reactivity as alkaline cements,” *Fuel*, vol. 82, pp. 2259–2265, 2003.
- [13] S. E. Wallah and B. V. Rangan, “Low-calcium fly ash-based geopolymer concrete: Long term properties,” Research Report GC 2, Curtin University of Technology, Perth, Australia, 2006.
- [14] F. Škvára, L. Kopecký, V. Šmilauer, and Z. Bittnar, “Material and structural characterization of alkali activated low-calcium brown coal fly ash,” *Journal of Hazardous Materials*, vol. 168, pp. 711–720, 2009.

- [15] J. Davidovits, “Chemistry of geopolymeric systems, terminology,” in *Geopolymer '99 International Conference*, (Saint Quentin, France), pp. 9–40, 1999.
- [16] M. Criado, A. Fernández-Jiménez, and A. Palomo, “Alkali activation of fly ash. part iii: Effect of curing conditions on reaction and its graphical description,” *Fuel*, vol. 89, no. 11, pp. 3185 – 3192, 2010.
- [17] C. Chen, W. Gong, W. Lutze, I. Pegg, and J. Zhai, “Kinetics of fly ash leaching in strongly alkaline solutions,” *Journal of Materials Science*, vol. 46, pp. 590–597, 2011.
- [18] A. Fernández-Jiménez, A. Palomo, I. Sobrados, and J. Sanz, “The role played by the reactive alumina content in the alkaline activation of fly ashes,” *Microporous and Mesoporous Materials*, vol. 91, pp. 111–119, 2006.
- [19] Y. Zhang, Z. Li, W. Sun, and W. Li, “Setting and Hardening of Geopolymeric Cement Pastes Incorporated with Fly Ash,” *ACI Materials Journal*, vol. 106, no. 5, pp. 405 – 412, 2009.
- [20] J. L. Provis and J. S. J. van Deventer, “Geopolymerisation kinetics. 2. Reaction kinetic modelling,” *Chemical Engineering Science*, vol. 62, pp. 2318–2329, 2007.
- [21] J. Němeček, V. Šmilauer, and L. Kopecký, “Nanoindentation characteristics of alkali-activated aluminosilicate materials,” *Cement and Concrete Composites*, vol. 33, no. 2, pp. 163–170, 2011.
- [22] P. Hlaváček, V. Šmilauer, R. Šulc, L. Kopecký, and F. Škvára, “Elastic properties of geopolymer concrete based on fly-ash,” in *Novel Developments and Innovation in Cementitious Materials*, p. 4, 2011.
- [23] F. Škvára, L. Kopecký, L. Myšková, V. Šmilauer, L. Alberovská, and L. Vinšová, “Aluminosilicate polymers - influence of elevated temperatures, efflorescence,” *Ceramics - Silikáty*, vol. 53, no. 4, pp. 276–282, 2009.
- [24] L. Ly, E. R. Vance, D. S. Perera, Z. Aly, and K. Olufson, “Leaching of geopolymers in deionised water,” *Advances in Technology of Materials and Materials Processing Journal*, vol. 239, no. 8, pp. 236–247, 2006.
- [25] F. H. Wittmann and A. Balkema, *Advances in autoclaved aerated concrete*. AA Balkema, 1992.
- [26] N. G. Costopoulos and H. K. Newhouse, “Building material manufacturing from fly ash,” Apr. 21 1987. US Patent 4,659,385.

- [27] E. Prud'homme, P. Michaud, E. Joussein, C. Peyratout, A. Smith, S. Arrii-Clacens, J.-M. Clacens, and S. Rossignol, "Silica fume as porogent agent in geo-materials at low temperature," *Journal of the European Ceramic Society*, vol. 30, no. 7, pp. 1641–1648, 2010.
- [28] E. Prud'homme, P. Michaud, E. Joussein, C. Peyratout, A. Smith, and S. Rossignol, "In situ inorganic foams prepared from various clays at low temperature," *Applied Clay Science*, vol. 51, no. 1, pp. 15–22, 2011.
- [29] S. Delair, E. Prud'homme, C. Peyratout, A. Smith, P. Michaud, L. Eloy, E. Joussein, and S. Rossignol, "Durability of inorganic foam in solution: The role of alkali elements in the geopolymer network," *Corrosion Science*, vol. 59, no. 0, pp. 213 – 221, 2012.
- [30] J. Bell and W. Kriven, "Preparation of ceramic foams from metakaolin-based geopolymer gels," in *Ceram Eng Sci Proc*, vol. 29, pp. 97–112, 2009.
- [31] M. S. Cilla, P. Colombo, and M. R. Morelli, "Geopolymer foams by gelcasting," *Ceramics International*, vol. 40, no. 4, pp. 5723 – 5730, 2014.
- [32] M. S. Cilla, M. R. Morelli, and P. Colombo, "Open cell geopolymer foams by a novel saponification/peroxide/gelcasting combined route," *Journal of the European Ceramic Society*, vol. 34, no. 12, pp. 3133 – 3137, 2014.
- [33] E. Hammel, X. Tang, M. Trampert, T. Schmitt, K. Mauthner, A. Eder, and P. Pötschke, "Carbon nanofibers for composite applications," *Carbon*, vol. 42, no. 5, pp. 1153–1158, 2004.
- [34] B. I. Yakobson, C. Brabec, and J. Bernholc, "Nanomechanics of carbon tubes: instabilities beyond linear response," *Physical review letters*, vol. 76, no. 14, p. 2511, 1996.
- [35] A. Cwirzen, K. Habermehl-Cwirzen, and V. Penttala, "Surface decoration of carbon nanotubes and mechanical properties of cement/carbon nanotube composites," *Advances in cement research*, vol. 20, no. 2, pp. 65–73, 2008.
- [36] M. S. Konsta-Gdoutos, Z. S. Metaxa, and S. P. Shah, "Multi-scale mechanical and fracture characteristics and early-age strain capacity of high performance carbon nanotube/cement nanocomposites," *Cement and Concrete Composites*, vol. 32, no. 2, pp. 110–115, 2010.

- [37] G. Y. Li, P. M. Wang, and X. Zhao, “Mechanical behavior and microstructure of cement composites incorporating surface-treated multi-walled carbon nanotubes,” *Carbon*, vol. 43, no. 6, pp. 1239–1245, 2005.
- [38] P. Morgan, *Carbon fibers and their properties*. CRC Press, 2005.
- [39] F. Sanchez and C. Ince, “Microstructure and macroscopic properties of hybrid carbon nanofiber/silica fume cement composites,” *Composites Science and Technology*, vol. 69, no. 7, pp. 1310–1318, 2009.
- [40] A. G. Nasibulin, S. D. Shandakov, L. I. Nasibulina, A. Cwirzen, P. R. Mudimela, K. Habermehl-Cwirzen, D. A. Grishin, Y. V. Gavrilov, J. E. Malm, U. Tapper, *et al.*, “A novel cement-based hybrid material,” *New Journal of Physics*, vol. 11, no. 2, p. 023013, 2009.
- [41] L. I. Nasibulina, I. V. Anoshkin, S. D. Shandakov, A. G. Nasibulin, A. Cwirzen, P. R. Mudimela, K. Habermehl-Cwirzen, J. E. M. Malm, T. S. Koltsova, Y. Tian, E. S. Vasilieva, V. Penttala, O. V. Tolochko, M. J. Karppinen, and E. I. Kauppinen, “Direct synthesis of carbon nanofibers on cement particles,” *Transportation Research Record: Journal of the Transportation Research Board*, vol. 2, no. 2142, pp. 96 – 101, 2010.
- [42] V. Šmilauer, P. Hlaváček, and P. Padevět, “Micromechanical analysis of cement paste with carbon nanotubes,” *Acta Polytechnica*, vol. 52, no. 6, 2012.
- [43] F. Škvára, V. Šmilauer, P. Hlaváček, L. Kopecký, and Z. Cílová, “A weak alkali bond in (N, K)–A–S–H gels: Evidence from leaching and modeling,” *Ceramics - Silikáty*, vol. 56, no. 4, pp. 374–382, 2012.
- [44] P. Hlaváček, V. Šmilauer, F. Škvára, L. Kopecký, and R. Šulc, “Inorganic foams made from alkali-activated fly ash: mechanical, chemical and physical properties,” *Journal of the European Ceramic Society*, vol. in Press, 2014.
- [45] P. Hlaváček, *Micromechanical analysis of alkali activated fly ashes*. M.Sc. Thesis, Czech Technical University in Prague, 2010.
- [46] R. Šulc, *Vliv přísad a příměsí na hodnoty fyzikálně mechanických a chemických vlastností POPbetonu*. Ph.D. Thesis, Czech Technical University in Prague, 2012. (in Czech).
- [47] T. Strnad, *Physical - mechanical properties of a material on the basis of alkaline activated fly ash*. Ph.D. Thesis, Czech Technical University, Faculty of Civil Engineering, 2011. (in Czech).

- [48] E. Holt, *Early age autogenous shrinkage of concrete*. VTT Publications, 2001.
- [49] FIB, *Model Code 2010*. International Federation for Structural Concrete (fib), 2010.
- [50] Z. P. Bažant and S. Baweja, “Creep and shrinkage prediction model for analysis and design of concrete structures: Model B3,” tech. rep., Am. Concrete Institute, 2000.
- [51] G. Pickett, *Effect of Aggregate on Shrinkage of Concrete and Hypothesis Concerning Shrinkage*. Bulletin (Portland Cement Association. Research and Development Laboratories. Research Dept.), Portland Cement Association, 1956.
- [52] B. Patzák and et al., “Object Oriented Finite Element Method - OOFEM.” <http://www.oofem.org>, since 1993.
- [53] R. Vedalakshmi, V. Saraswathy, H.-W. Song, and N. Palaniswamy, “Determination of diffusion coefficient of chloride in concrete using warburg diffusion coefficient,” *Corrosion Science*, vol. 51, no. 6, pp. 1299 – 1307, 2009.
- [54] V. Šmilauer and J. Němeček, “Elastic properties of alkaline activated fly ash: results from nanoindentation and micromechanical modeling,” in *Alkali Activated Materials - Research, Production and Utilization*, pp. 677–688, 2007.
- [55] A. Zaoui, “Continuum Micromechanics: Survey,” *Journal of Engineering Mechanics*, vol. 128, no. 8, p. 808 – 816, 2002.
- [56] T. Mori and K. Tanaka, “Average stress in matrix and average elastic energy of materials with misfitting inclusions,” *Acta Metallurgica*, vol. 21, no. 5, pp. 1605–1609, 1973.
- [57] R. Hill, “Theory of mechanical properties of fiber-strengthened materials - III: Self-consistent model,” *J. Mech. Phys. Solids*, vol. 13, pp. 189–198, 1965.
- [58] Building Research Establishment, “Autoclaved aerated concrete,” *Digest*, no. 342, p. 7 pp., 1989.
- [59] D. P. Bentz, E. J. Garboczi, and K. A. Snyder, “A Hard Core/Soft shell Microstructural Model for Studying Percolation and Transport in Three-Dimensional Composite Media,” tech. rep., NIST Building and Fire Research Laboratory, Gaithersburg, Maryland, 1999.
- [60] P. R. Mudimela, L. I. Nasibulina, A. G. Nasibulin, A. Cwirzen, M. Valkeapää, K. Habermehl-Cwirzen, J. E. Malm, M. J. Karppinen, V. Penttala, T. S. Koltsova, et al., “Synthesis of carbon nanotubes and nanofibers on silica and cement matrix materials,” *Journal of Nanomaterials*, vol. 2009, p. 29, 2009.

- [61] RILEM, “Determination of the fracture energy of mortar and concrete by means of three-point bend tests on notched beams,” *Materials and Structures*, vol. 18, pp. 287–290, 1985.
- [62] G. Constantinides and F.-J. Ulm, “The effect of two types of C-S-H on the elasticity of cement-based materials: Results from nanoindentation and micromechanical modeling,” *Cem. Concr. Res.*, vol. 34, no. 1, pp. 67–80, 2004.

6 List of publications

Journals:

- V. Šmilauer, F. Škvára, J. Němeček, L. Kopecký, P. Hlaváček. Application of Micromechanics on Alkali-activated Materials. *Advances in Science and Technology*, 2010, 69(1), p. 75-85. (20 %)
- V. Šmilauer, P. Hlaváček, F. Škvára, R. Šulc, L. Kopecký, J. Němeček. Micromechanical multiscale model for alkali activation of fly ash and metakaolin, *Journal of Materials Science*, 2011, 46(20), p. 6545-6555. (20 %)
- V. Šmilauer, P. Hlaváček, P. Padevět: Micromechanical analysis of cement paste with carbon nanotubes, *Acta Polytechnica*, 2012, 52(6), p. 35-41. (40 %)
- F. Škvára, V. Šmilauer, P. Hlaváček, L. Kopecký, Z. Cílová. A weak alkali bond in (N, K)–A–S–H gels: Evidence from leaching and modeling, *Ceramics-Silikáty*, 2012, 56(4), p. 374-382. (23 %)
- Z. Abdollahnejad, P. Hlaváček, S. Miraldo, F. Pacheco-Torgal and J.L. Barroso de Aguiar. Compressive strength, microstructure and hydration products of hybrid alkaline cements. *Materials Research - Ibero-american Journal of Materials*, 2014. (10 %)
- P. Hlaváček, V. Šmilauer, F. Škvára, L. Kopecký, R. Šulc. Inorganic foams made from alkali-activated fly ash: mechanical, chemical and physical properties, *Journal of the European Ceramics Society*, 2014, *in Press*. (80 %)

International conferences:

- P. Hlaváček, V. Šmilauer. Model of ion transport in alkali-activated materials. In *Engineering Mechanics 2010*. Prague: Institute of Thermomechanics ASCR, 2010, p. 41-42. (50 %)

- V. Šmilauer, F. Škvára, J. Němeček, L. Kopecký, P. Hlaváček. Application of Micromechanics on Alkali-activated Materials. In Proceedings of the 12th International Ceramics Congress. Zurich: Trans Tech Publications ltd, 2010. (20 %)
- P. Hlaváček, V. Šmilauer, B. Patzák. Easy Generation of Models/Meshes Using an Open-Source Software Salome. In Engineering Mechanics 2011. Praha: Ústav termomechaniky AV ČR, 2011. (50 %)
- P. Hlaváček, V. Šmilauer, R. Šulc, L. Kopecký, F. Škvára. Elastic properties of geopolymer concrete based on fly-ash. In 31st Cement and Concrete Science Conference 2011. London: Imperial College Press, 2011. (30 %)
- P. Hlaváček, V. Šmilauer, P. Padevět et al. Cement Grains with Surface-Synthesized Carbon Nanofibers: Mechanical Properties and Nanostructure. In Nanocon 2011, Conference Proceedings. Ostrava: TANGER, spol.s r.o, 2011. (50 %)
- P. Hlaváček, V. Šmilauer. Fracture properties of cementitious composites reinforced with carbon nanofibers/nanotubes.. In Engineering Mechanics 2012. Prague: Institute of Theoretical and Applied Mechanics Academy of Sciences of the Czech Republic, 2012, p. 1-7. (50 %)
- V. Šmilauer, P. Hlaváček. Micromechanical properties of cement paste with carbon nanotubes. In Ibausil - 18. Internationale Baustofftagung. Weimar: Bauhaus-Universität Weimar, 2012, p. 822-829. (50 %)
- Z. Abdollahnejad, P. Hlaváček, F. Pacheco-Torgal, J.L. Barroso de Augiar. Preliminary experimental investigation on one-part geopolymer mixes. In Actas do Congresso da Construção 2012. 2012. (25 %)
- P. Hlaváček, V. Šmilauer. Fracture Properties of Cement Composites Reinforced by Carbon Nanotubes. In Computational Modeling of Fracture and Failure of Materials and Structures. Prague, CTU in Prague, 2013, p. 77. (50 %)
- P. Hlaváček, V. Šmilauer, F. Škvára. Alkali-activated fly ash foams - synthesis, chemical-physical properties and microstructure modeling. In Proceedings of the 13th International Ceramics Congress. 2014. (60 %)

7 List of projects

The financial support from the Grant Agency of the Czech Technical University in Prague and from the Czech Science Foundation is gratefully acknowledged.

7.1 Grant Agency of the Czech Technical University in Prague

2010-2012: SGS10/135/OHK1/2T/11 Experimental and numerical methods for multi-scale modeling of materials

2013-2014: SGS12/116/OHK1/2T/11 Microstructural and micromechanical characteristics of composites based on aluminum and aluminosilicates

7.2 Czech Science Foundation

2008-2010: GA103/08/1639 Microstructure of Inorganic Aluminosilicate Polymers

2011-2012: GD103/09/H078 Computer and Experimental Analysis of Civil Engineering Materials and Their Multilayered Systems

2012-2014: GAP104/12/0102 Aluminosilicate polymer foams

2013-2014: GA13-22230S Hybridní víceúrovňové nástroje modelování heterogenních pevných látek

Part II

Paper 1

Authors: Vít Šmilauer, Petr Hlaváček, František Škvára, Rostislav Šulc,
Lubomír Kopecký, Jiří Němeček

Title: Micromechanical multiscale model for alkali activation of fly ash
and metakaolin

Journal: Journal of Materials Science

Number: 20

Volume: 46

Year: 2011

Micromechanical multiscale model for alkali activation of fly ash and metakaolin

Vít Šmilauer · Petr Hlaváček · František Škvára ·
Rostislav Šulc · Lubomír Kopecký ·
Jiří Němeček

Received: 3 February 2011 / Accepted: 30 April 2011
© Springer Science+Business Media, LLC 2011

Abstract The process of alkali activation of fly ash and metakaolin is examined in the view of micromechanics. Elasticity is predicted via semi-analytical homogenization methods, using a combination of intrinsic elastic properties obtained from nanoindentation, evolving volume fractions and percolation theory. A new quantitative model for volume fraction is formulated, distinguishing the evolution of unreacted aluminosilicate material, solid gel particles of N-A-S-H gel, and open porosity, which is partially filled with the activator. The stiffening of N-A-S-H gel is modeled by increasing the fraction of solid gel particles. Their packing density and intrinsic elasticity differ in N-A-S-H gels synthesized from both activated materials. Percolation theory helps to address the quasi-solid transition at early ages and explains a long setting time and the beneficial effect of thermal curing. The low ability of N-A-S-H gel to

bind water chemically explains the high porosity of Ca-deficient activated materials. Micromechanical analysis matches well the elastic experimental data during the activation and elucidates important stages in the formation of the microstructure.

Introduction

Reactions between strong alkaline liquids and solid aluminosilicate materials produce an inorganic binder, which is known as geopolymer, inorganic polymer, chemically bonded ceramics, or alkali-activated cement. The state-of-the-art and historical achievements are comprehensively reviewed in several works [1–3]. It is worthy to note that the majority of fundamental research was carried out by chemists, who focused on atomistic and molecular scales using popular NMR or FTIR analyses. Another group of scientists tried to optimize the composition and curing process of activated materials, including fly ash [4–8].

The desire for a deeper understanding of alkali activation processes led researchers to various models. The first group of models focuses on the formation of a binder, emphasizing chemical and polycondensation processes during hardening [1, 9–11]. The second group describes reaction kinetics [11–13]. Notably, the model of Provis and van Deventer [14] aimed to capture eight ongoing reactions fitted with ten parameters. The third group describes the morphological evolution of the microstructure. For example, a descriptive model for alkali-activated fly ash captures general mechanisms independent of the activator composition or concentration [12]. All these models create a background for the micromechanical model assembled here.

V. Šmilauer (✉) · P. Hlaváček · R. Šulc · L. Kopecký ·
J. Němeček

Faculty of Civil Engineering, Czech Technical University
in Prague, Thákurova 7, 166 29 Prague 6, Czech Republic
e-mail: vit.smilauer@fsv.cvut.cz

P. Hlaváček
e-mail: petr.hlavacek@fsv.cvut.cz

R. Šulc
e-mail: rostislav.sulc@fsv.cvut.cz

L. Kopecký
e-mail: kopecky@fsv.cvut.cz

J. Němeček
e-mail: jiri.nemecek@fsv.cvut.cz

F. Škvára
Department of Glass and Ceramics, Institute of Chemical
Technology Prague, Technická 5, 166 28 Prague,
Czech Republic
e-mail: frantisek.skvara@vscht.cz

To the best knowledge, no quantitative model describing the volumetric evolution of phases in a simple manner has been published. These first-order models are extremely important in characterizing the evolution of porosity, which is related to other properties such as elasticity or strength. Powers and Brownyards [15] created such a model for Portland cement, which was a breakthrough at that time and helped later to optimize the microstructure of ordinary concrete. A similar volumetric model for the alkali activation of fly ash and metakaolin is formulated here to fill the gap.

The application of mechanics on finer scales, known as micromechanics, brings a deeper insight into the formation of the microstructure and properties as has been demonstrated for Portland cement [16–18], concrete [19], or textile [20]. The focus here is given on multiscale elastic analysis, which is based on the definition of intrinsic elastic properties of constituents. These were previously identified by the grid nanoindentation technique [21]. The changes in volume fractions and connectedness of individual constituents on fine scales are projected to elasticity on a higher scale. The scale bridging explains the formation of N-A-S-H gel and the microstructure from another stand-point.

Materials and methods

Fly ash and metakaolin

Low-calcium fly ash of class F originates from the Opatovice thermal electric power plant, the Czech Republic. The specific Blaine surface is 210 m²/kg. The XRD Rietveld analysis yielded the composition of 70 vol.% amorphous phases, 24 vol.% mullite, and 6 vol.% quartz.

Metakaolin comes from České lupkové závody a.s., Nové Strašecí, the Czech Republic. Chemical compositions of both materials are given in Table 1 while Fig. 1 shows the particle size distributions.

Alkali activator and curing

The activator was prepared from NaOH pellets, tap water, and sodium silicate in the form of water glass. Table 2 provides the ratios in the mixtures of fly ash and metakaolin. Note that metakaolin requires significantly more activator to maintain feasible workability. The compositions of both

Table 1 The chemical composition of fly ash and metakaolin (wt%)

	SiO ₂	Al ₂ O ₃	Fe ₂ O ₃	CaO	TiO ₂	K ₂ O
Fly ash	51.9	32.8	6.3	2.7	1.89	2.12
Metakaolin	48.66	47.41	1.33	0.03	1.99	0.15

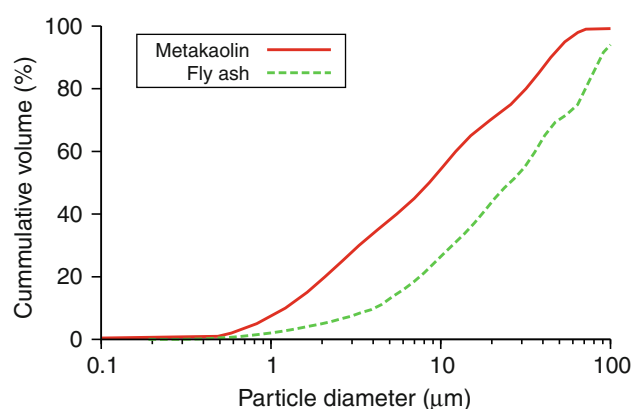


Fig. 1 Particle size distribution of fly ash and metakaolin

Table 2 Mixture composition. Mass oxide ratios for activators and activator-to-solid mass ratios

	Activator ratios		Activator-to-solid ratio (wt%)
	Na ₂ O/SiO ₂ (–)	H ₂ O/Na ₂ O (–)	
Fly ash	0.881	3.925	0.531
Metakaolin	1.669	2.743	1.416

mixtures were previously optimized to yield high compressive strength [8]. The mixtures were stirred for 5 min and cast in either plastic ampoules 26 mm in diameter and 45 mm in height or prisms 40 × 40 × 160 mm, gently vibrated for 5 min and sealed with a plastic foil. Ambient-cured samples were unmoulded after 10 days of hardening, after gaining sufficient strength, and kept in closed plastic bags. Heat-cured metakaolin samples were exposed to 80 °C for 12 h.

The 28-day compressive strength of heat-cured alkali-activated fly ash (AAFA) yields 84.14 ± 9.24 MPa, as determined from half-prisms 40 × 40 × 80 mm, and that of alkali-activated metakaolin (AAMK) 35.5 ± 1.20 MPa, obtained from 20 × 20 × 20 mm cubes.

Determination of open porosity

Cylindrical samples of a well-defined geometry (diameter ≈ 25 mm and thickness ≈ 5 mm) were dried out in an oven at 105 °C. The samples remained in the oven until the weight loss had stabilized, which took between 3 and 6 days. In addition, the He pycnometry provided skeletal densities of fly ash, metakaolin and activated mature samples. The open porosity was determined according to the following equation

$$\phi = \frac{\rho^{\text{sk}} - \rho^{\text{b}}}{\rho^{\text{sk}} - \rho^{\text{im}}}, \quad (1)$$

where ρ^{sk} represents the skeletal density, ρ^{b} is the bulk density, and ρ^{im} stands for the density of the intruding

medium. For the determination of ρ^{sk} , crushed samples were dried at 105 °C for 12 h prior to MIP (Autopore III Micromeritics) and He pycnometry (Micromeritics AccuPyc 1330) tests. The ρ^{sk} value is biased with resolution limits of MIP from the top ($d \approx 120 \mu\text{m}$) and the He pycnometry resolution from the bottom ($d \approx 0.062 \text{ nm}$). In the majority of cases, the intruding medium corresponded to air with $\rho^{im} \approx 0 \text{ g/cm}^3$. Some samples were immersed into non-polar *n*-octane with $\rho^{im} = 0.70134 \text{ g/cm}^3$ to check the penetration of larger molecules into smaller pores [22]. The open porosity was always determined as an average from three samples.

Continuum elastic micromechanics

Continuum micromechanics provides the framework in which elastic properties of heterogeneous microscale components are homogenized to the macroscale [23]. The analysis usually starts by defining a representative volume element (RVE), which identifies different components and their morphologies. Certain restrictions in terms of scale separation exist on the RVE size [23]; RVE must be substantially smaller than the macroscale body, which allows imposing homogeneous boundary conditions over RVE. This leads to a constant stress/strain field in individual microscale components of ellipsoidal shapes.

Effective elastic properties are obtained through averaging over the local contributions. Considering isotropic spherical inclusions perfectly bonded with a matrix leads to the estimation of effective bulk and shear moduli [23]

$$k_{\text{eff}} = \frac{\sum_r f_r k_r \left[1 + \alpha_0 \left(\frac{k_r}{k_0} - 1 \right) \right]^{-1}}{\sum_r f_r \left[1 + \alpha_0 \left(\frac{k_r}{k_0} - 1 \right) \right]^{-1}}, \tag{2}$$

$$\mu_{\text{eff}} = \frac{\sum_r f_r \mu_r \left[1 + \beta_0 \left(\frac{\mu_r}{\mu_0} - 1 \right) \right]^{-1}}{\sum_r f_r \left[1 + \beta_0 \left(\frac{\mu_r}{\mu_0} - 1 \right) \right]^{-1}}, \tag{3}$$

$$\alpha_0 = \frac{3k_0}{3k_0 + 4\mu_0}, \tag{4}$$

$$\beta_0 = \frac{6k_0 + 12\mu_0}{15k_0 + 20\mu_0}, \tag{5}$$

where f_r is the volume fraction of the r th phase, k_r its bulk modulus, and μ_r its shear modulus. A reference medium is described as the 0th phase.

Aligning k_0, μ_0 with a specific phase k_r, μ_r leads to the Mori–Tanaka method [24]. The reference medium creates a continuous matrix in which all inclusions are embedded. The self-consistent scheme of Budiansky, elaborated by Hill [25], is an implicit scheme for composites with a skeletal structure, where no dominant matrix exists. Now,

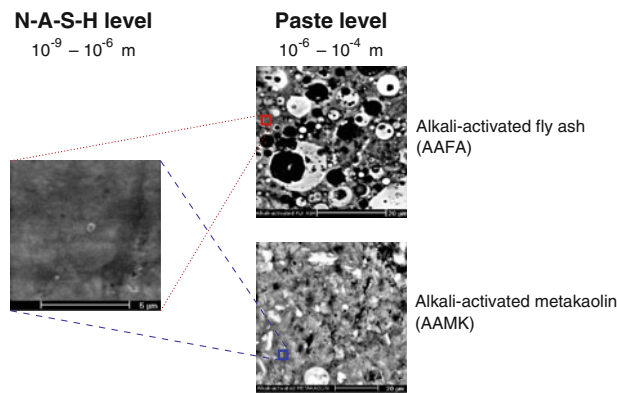


Fig. 2 Two levels in the multiscale analysis. The paste level displays two microstructures from alkali-activated fly ash and metakaolin

the reference medium points back to the homogenized medium itself, which leads to $k_0 = k_{\text{eff}}$ and $\mu_0 = \mu_{\text{eff}}$ after several iterations.

Levels of N-A-S-H gel and paste

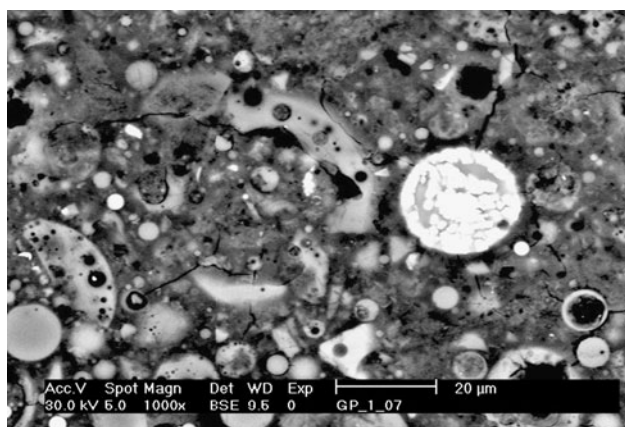
The heterogeneity of alkali-activated materials is manifested on several length scales. For the analysis of alkali-activated pastes, the definition of two levels is appropriate. Figure 2 shows the level of N-A-S-H gel, which contains a poorly crystallized product from a low calcium, alkali-activated material [4]. The paste level contains remnants of activated material, a part of the open porosity partially filled with an activator and the N-A-S-H gel.

Results and discussion

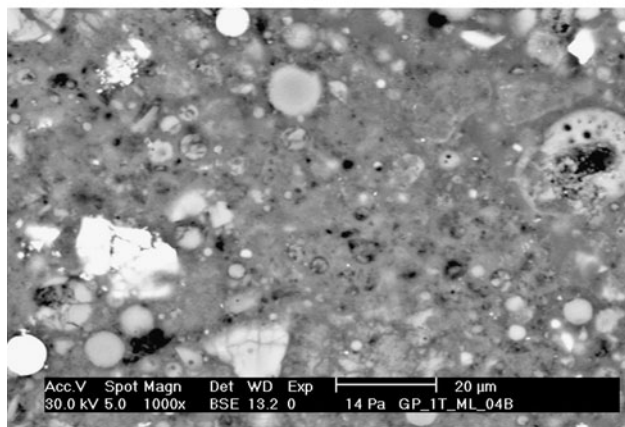
Figure 3 shows three characteristic BSE images of mature AAFA and AAMK samples.

Degree of reaction

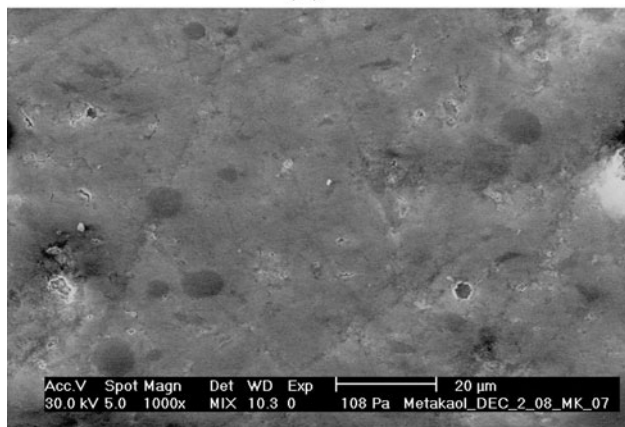
The degree of reaction, abbreviated as DoR, is defined as the amount of activated material consumed during the alkali activation process. In the activated material, reactive vitreous components are not differentiated from slowly reacting crystalline phases, hence DoR is always lower than one. The direct simulation of the DoR evolution in time, or reaction kinetics, is beyond the capabilities of presented models. Instead, the evolution of DoR in AAFA is taken from experimental data of Chen et al. [13], who measured the DoR progress on AAFA samples activated with 7.5 M KOH solution. The extent of DoR was determined by the HCl acid attack. Similar kinetic results were observed on calorimetric data, revealing that the activator/fly ash ratio is insignificant for the DoR evolution and that



(a)



(b)



(c)

Fig. 3 BSE images of matured AAFA and AAMK samples used further. **a** Ambient-cured fly ash for 11 months at ≈ 25 °C. **b** Heat-cured fly ash at 80 °C for 12 h. **c** Heat-cured metakaolin at 80 °C for 12 h

a maximum reaction rate occurs at 8–10 min after the contact, substantially reduced after 2 h at elevated temperatures [26].

The Arrhenius equation is utilized to recalculate DoR for various curing temperatures

$$\tau_e(T_0) = \tau(T) \exp \left[\frac{E_a}{R} \left(\frac{1}{T_0} - \frac{1}{T} \right) \right], \quad (6)$$

where T is an arbitrary constant temperature, T_0 is the reference temperature, R is the universal gas constant (8.314 J/mol K) and E_a is the apparent activation energy. The activation energy was found as 86.2 kJ/mol via isothermal calorimetry for activated AAFA using 8 M NaOH [8] which fits within 60–102 kJ/mol [13], although lower energies such as 31.5 ± 6 kJ/mol were reported for a different system of metakaolin and potassium activator [27]. Figure 4 shows the DoR evolution at 25 °C, recalculated from the data presented in [13] for temperatures of 20–75 °C with the help of Eq. 6. Also, the data from Fig. 4 were fitted using the Levenberg–Marquardt algorithm to the function

$$\text{DoR} = \frac{0.8}{1 + (0.17 - 0.17 \ln(t/10^4))^{4.477}}, \quad (7)$$

$t \leq 10^4$ days, $R^2 = 0.954$,

where t stands for an activation time in days at a temperature of 25 °C. Similar results for the evolution of DoR are available elsewhere [11, 12].

AAMK reacts much faster than fly ash and the kinetics was not monitored. Deduction from nanoindentation data provided DoR for mature AAMK samples as described in the following subsection.

Volumetric model for alkali activation

The volumetric model for the alkali activation process presents a stepping stone in micromechanical analysis.

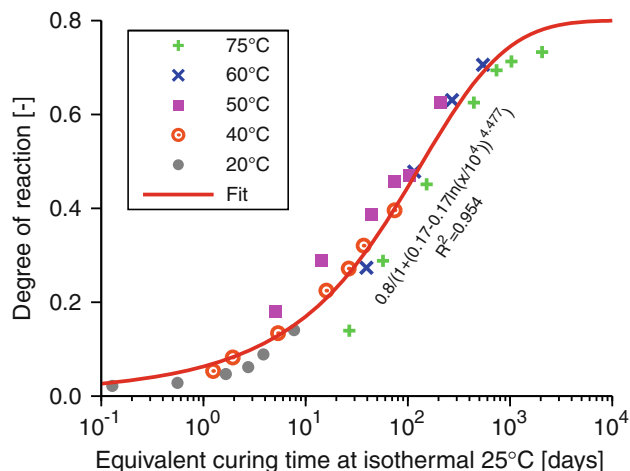


Fig. 4 Progress of DoR for alkali-activated fly ash by 7.5 M KOH obtained by time scaling according to Eq. 6. Here, the evolution of DoR is showed for a reference temperature of 25 °C. Original data [13] were gathered at isothermal temperatures of 20–75 °C. Activation energy considered is 86.2 kJ/mol

Much inspiration has been gathered from Portland cement-based systems, through famous research carried out by Powers and Brownyard [15]. Three assumptions underline the presented volumetric model:

1. No change in volume occurs after initial setting. The volumetric balance of all liquid and solid phases is maintained at any time. Although alkali-activated pastes exhibit high autogenous shrinkage, the effect in volume reduction is low. Rodríguez et al. [28] report high autogenous shrinkage, 8000 μ strain after 35 days of AAMK paste curing. This corresponds to 2.4% decrease in volume. Strnad [29] reports 4240 μ strain after 28 days of AAFA paste ambient curing. To the best knowledge, chemical shrinkage was never reported for AAMK or AAFA; the model makes no difference between filled and empty capillary pores.
2. The model uses only the DoR as the independent variable. Such a simplification neglects separate contributions of dissolution and polymerization of N-A-S-H gel, as previously noted [30]. More precise calculations would determine DoR from formed gel, instead of from dissolved material [3, p 123].
3. The whole activator is treated in the form of evaporable water, disregarding the solid part remaining after drying.

The volumetric model for AAFA or AAMK is expressed with a set of linear equations. They contain no time and depend on initial volumetric fractions and DoR only

$$f_{FA,MK}^{Skel}(\text{DoR}) = f_{FA,MK}^{Skel}(0^+)[1 - \text{DoR}], \quad (8)$$

$$f_{SGP}(\text{DoR}) = [f_{FA,MK}^{Skel}(0^+) + \alpha]\text{DoR}, \quad (9)$$

$$f_{FA,MK}^{Voids}(\text{DoR}) = f_{FA,MK}^{Voids}(0^+) - \beta\text{DoR}, f_{FA,MK}^{Voids}(\text{DoR}) \geq 0, \quad (10)$$

$$f_{OP}(\text{DoR}) = 1 - f_{FA,MK}^{Voids}(\text{DoR}) - f_{FA,MK}^{Skel}(0^+) - \alpha\text{DoR}. \quad (11)$$

The meaning of the symbols is explained on the system of activated fly ash first, see Fig. 5a for graphical

representation. $f_{FA}^{Skel}(\text{DoR})$ represents the skeletal volume fraction of unreacted fly ash. The voids persisting in unreacted fly ash are quantified with $f_{FA}^{Voids}(\text{DoR})$. It must be noted that the activator efficiently destroys a thin shell of plerospheres within a few minutes and opens the voids, which is denoted as time 0^+ . This is manifested by a partial loss of workability and heat release in isothermal calorimetry. $f_{FA}^{Voids}(0^+)$ was determined from the combination of the known skeletal density of fly ash, the known density of activating solution and the measured volume, and the weight of the mixture immediately after mixing.

f_{SGP} represents the volume fraction of solid gel particles. The term N-A-S-H gel is intentionally not used since it is defined on a higher scale as a combination of solid gel particles and a part of open porosity.

f_{OP} represents the volume of open porosity, which equals the maximum volume occupied with evaporable water. The activator fills up the major part of open porosity during the activation.

Five parameters from Eqs. 8–11 have to be determined from a known composition. Table 3 summarizes densities, initial volume fractions and parameters α , β . The parameter

Table 3 Fitted parameters for the volumetric model of alkali activation

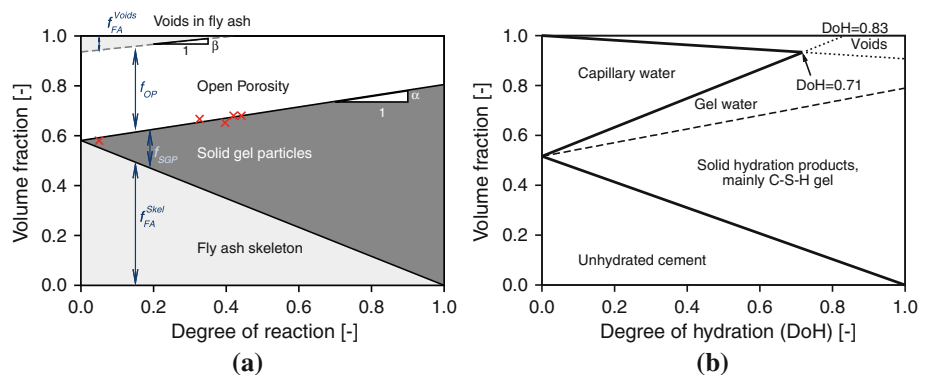
Parameter	AAFA	AAMK
Skeletal density of activated material (g/cm^3) ^a	2.070	2.372
Density of activator (g/cm^3)	1.545	1.477
Bulk density of paste (g/cm^3) ^{bc}	1.752	1.694
$f_{FA,MK}^{Skel}(0^+)$	0.581	0.296
$f_{OP}(0^+)$	0.355	0.672
$f_{FA,MK}^{Voids}(0^+)$	0.064	0.032
Parameter α	0.224	0.294
Parameter β	0.152	0.064

^a Determined from He pycnometry

^b Determined from measured geometry and sample mass

^c Including entrapped air

Fig. 5 The newly created volumetric model for alkali activation of fly ash and comparison to the Powers model for Portland cement. Measured open porosity is marked with crosses, parameters are summarized in Table 3. **a** Activated fly ash. **b** Portland cement at $w/c = 0.3$



β was obtained from porosity calculations using two intruding media according to Eq. 1. Here, the method of *n*-octan intrusion [22] yielded generally lower values than by water evaporation. Both porosities merged when $\text{DoR} \geq 0.42$, which leads to $\beta = 0.064/0.42 = 0.152$.

Figure 5b illustrates the fact that the Powers model for ordinary Portland cement paste yields a similar evolution of volume fractions as Fig. 5a. The major difference lies in gel water (occupying gel porosity under saturated conditions), associated with a characteristic 28% porosity of C-S-H [31]. Characteristic porosity of N-A-S-H gel is an invalid hypothesis as will be explained in “Elastic downscaling to a solid gel particle” section.

AAMK contains a much larger amount of open porosity, see Fig. 6. The AAMK bulk density of 1.694 g/cm^3 , see Table 3, corresponds well with the experiments of Duxson et al. [32], who reported $1.68\text{--}1.80 \text{ g/cm}^3$. The degree of reaction of mature samples, cured at $80 \text{ }^\circ\text{C}$ for 12 h, was determined from a histogram of indentation moduli [21]. Unreacted metakaolin corresponded to 2.8% of all solids by volume. Since nanoindentation does not “see” pores and open porosity was measured as 0.4263, $\text{DoR} = 1 - (1 - 0.4263) \cdot 0.028/0.296 = 0.946$ for a mature AAMK sample.

The pore size distribution obtained from MIP and He pycnometry is depicted in Fig. 7 for mature samples. Also, it is shown that matured ordinary Portland cement paste

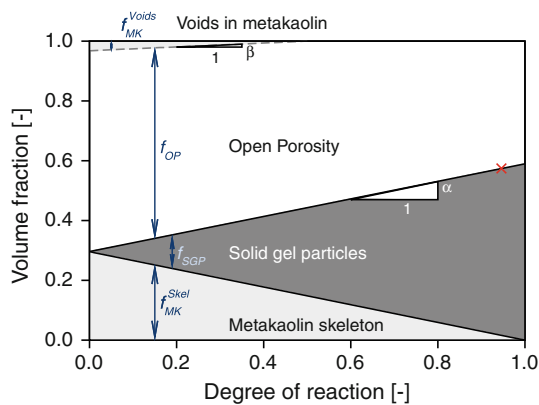
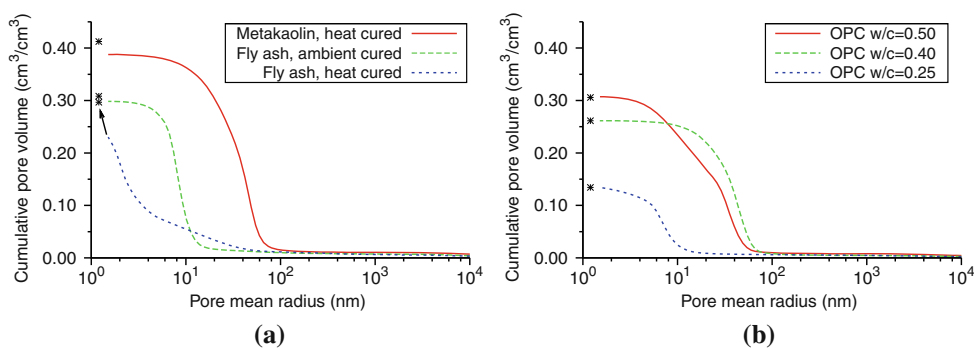


Fig. 6 The volumetric model for alkali activation of metakaolin. Measured open porosity is marked with the cross

Fig. 7 Cumulative pore volume for alkali-activated materials and Portland paste cured at $60 \text{ }^\circ\text{C}$ for 3 months. An asterisk denotes the total volume using also skeletal density from He pycnometry



with a water-to-cement ratio of 0.5 yields lower total porosity than presented activated materials. Note that ambient/heat curing of fly ash yields the same amount of open porosity but ambient curing contains more coarse pores. A different pore distribution also becomes obvious from Fig. 3.

The porosity results for AAFA are higher than those reported by Kovalchuk et al. [7], who found total porosity of activated fly ash, class F, between 15 and 20%, depending on the curing setup at a temperature of $95 \text{ }^\circ\text{C}$. They also noted that larger pores emerge under dry curing due to the evaporation of water and shrinkage of N-A-S-H gel.

Elastic downscaling to a solid gel particle

Elastic properties of mature N-A-S-H gel were previously obtained via grid nanoindentation from about 700 locations [21]. The mean Young’s modulus was unambiguously found in the range of $17.03\text{--}17.72 \text{ GPa}$, covering activated fly ash and metakaolin, cured under ambient or heat conditions. The indentation depth was approximately 300 nm , which reflects a part of open porosity, see Figs. 3 and 7.

Any sol–gel system (C-(A)-S-H, N-A-S-H) consists of solid particles dispersed in a liquid [33]. Sol–gel is far from equilibrium and solid particles may aggregate into clusters. If a condensation reaction in the system exists and is irreversible, more and more solid particles appear in the system and grow into fractals [33]. The linking of clusters continues until they reach a percolation threshold signaled by a sudden change of many properties such as elasticity.

It is worthy to mention that C-S-H is not a true gel but a precipitate, signaled by the presence of capillary pores and the appearance mainly around cement grains. A reversible condensation reaction dominates the C-S-H solidification [33]. Another consequence of reversibility is a constant 28% porosity of the C-S-H gel, irrespective of its origin [15]. The constant porosity allowed considering the C-S-H gel as one phase from a micromechanical perspective; a building block intermixed with porosity at a constant fraction [34, 35].

On the other hand, N-A-S-H is a true gel, which rather fills out all available volume and does not form only on the surface of activated material. The gel syneresis has been observed many times in alkali-activated materials; excessive shrinkage accompanied with strong sample disintegration might occur under sealed conditions [6, 29, 36]. Due to a true gel nature, no constant gel porosity exists, as in the case of C-S-H, and the micromechanical response needs to be determined from solid gel particles at the N-A-S-H level.

Two micromechanical parameters need to be identified for mature materials; the modulus of a fictitious solid gel particle and a fraction of open porosity which is associated to the N-A-S-H level. The latter is captured with the parameter $0 \leq \gamma \leq 1$, where 1 means a complete assignment of the open porosity to the N-A-S-H level. These two unknowns are unambiguously determined from nanoindentation moduli and macroscopic moduli. Table 4 summarizes data for mature AAFA and AAMK materials at the time of nanoindentation. In the case of AAFA, 98 days of ambient curing corresponds to $\text{DoR} = 0.440$ as determined from Eq. 7.

First, the parameter γ was determined from the known intrinsic properties in Table 5 and using homogenization via the self-consistent scheme at the paste level. The scheme is suitable especially for AAFA, where the volume fractions are roughly equal $f_{\text{SGP}} \approx f_{\text{OP}} \approx f_{\text{FA}}^{\text{skel}}$ at $\text{DoR} = 0.44$ and no dominant matrix can be distinguished. While practically all open porosity remained on the N-A-S-H level for AAFA, less than one third remained in the

Table 4 Parameters of mature activated materials at the time of indentation

Parameter	AAFA ^a	AAMK ^d
DoR	0.440	0.946
$f_{\text{FA,MK}}^{\text{skel}}$	0.325	0.016
f_{SGP}	0.354	0.558
f_{OP}	0.321	0.426
$f_{\text{FA,MK}}^{\text{voids}}$	0.000	0.000
γ	1.000	0.306
Normalized f_{SGP} on N-A-S-H level	0.525	0.811
Normalized f_{OP} on N-A-S-H level	0.475	0.189
E_{SGP} , downscaled (GPa)	48.160	25.480
E_{gel} , experiment (GPa)	$17.72 \pm 3.75^{\text{ac}}$	$17.72 \pm 4.43^{\text{cd}}$
E_{gel} , upscaled (GPa)	17.72	17.72
E_{paste} , experiment (GPa)	$32.05 \pm 0.90^{\text{ab}}$	$7.369 \pm 0.517^{\text{d}}$
E_{paste} , upscaled (GPa)	28.279	7.369

^a Ambient cured

^b Interpolated

^c Němeček et al. [21]

^d Heat-cured

Table 5 Intrinsic elastic properties used in homogenization models

Material	Young's modulus (GPa)	Poisson's ratio
Fly ash skeleton	105 ^a	0.2
Metakaolin skeleton	43.91 ^b	0.2
N-A-S-H gel	17.72 ^b	0.2
Open pores	0.001	0.001

Note Indentation moduli of fly ash and metakaolin skeletons underestimate their true stiffness; displacement under the indenter tip is biased with the deformation of compliant N-A-S-H gel surrounding the particles. The value 105 GPa for the fly ash skeleton assumes an average particle diameter 20–45 μm and the parallel arrangement of glass, mullite and quartz [37]. Indeed, the modulus from nanoindentation gives only 79.65 GPa [21]

^a Matsunaga et al. [37]

^b Němeček et al. [21]

case of AAMK. Such a result is consistent with Fig. 7, showing coarser porosity for AAMK.

Second, the downscaling from N-A-S-H gel to the solid gel particle was executed with the help of the Mori–Tanaka method. The self-consistent scheme, as an alternative, could not be applied. The reason is a high fraction of water-filled pores, which are close to the percolation threshold of the scheme. Unfortunately, the Young moduli 48.160 and 25.480 GPa show that no common solid gel particle exists for AAFA and AAMK.

The micromechanical analysis shows that the gel synthesized from AAMK is richer in solid gel particles which are also twice as compliant, compared to the gel from AAFA. This does not necessarily imply a different chemical composition of both gels, although small differences in the aluminum coordination and ²⁹Si NMR spectra were reported [1, 38]. In addition to chemical analysis, elastic modulus is a volumetric integral quantity, which also reflects the interaction between gel particles, their arrangement, organization, spacing, bonds, or rarefaction/compaction [39]. The metastable gel composition in activated materials is known to vary with an activator or the curing procedure. For example, a higher content of soluble Si in the system creates denser gel in AAMK [32]. Note that the activators were optimized to yield high compressive strength and they have different compositions.

Another factor yielding different elasticity of solid gel particles may arise from assumptions in homogenization methods, particularly perfect bonds among phases and ergodicity. The Mori–Tanaka scheme assumes matrix-inclusion morphology with a uniform distribution of solid gel particles in space. When a cluster-like assemblage with percolation characteristics dominates the morphology, several solid gel particles remain unconnected. Homogenization methods smear such an effect which leads to apparently softer inclusion. Other experimental methods

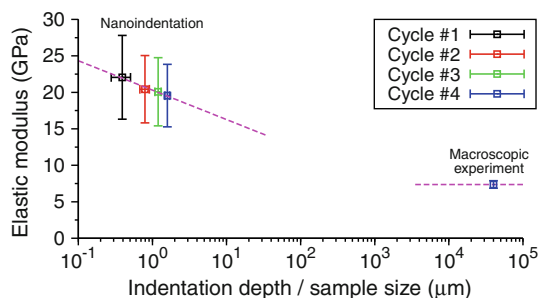


Fig. 8 Continuous porosity distribution of AAMK leads to the decrease of elastic moduli with the sample volume

are needed to support these indirect indications of different N-A-S-H gel nanostructures.

A continuous distribution of porosity breaks the condition of scale separation [23]. Figure 8 illustrates such a fact via a 10 × 12 nanoindentation grid on mature AAMK with a spacing of 30 μm and varying indenter’s depth. The first cycle of the indenter penetrates roughly 400 nm into the material, is unloaded and continues on the same spot up to 800, 1200, and 1600 nm. It is worthy to note that the indenter does not “see” voids on the surface and measures, in fact, the underlying solid material. Larger indents take more material into account and converge to the macroscopic modulus obtained on prisms 40 × 40 × 160 mm.

Notes on drying shrinkage

High autogenous shrinkage of alkali-activated concretes and pastes was noted under ambient-curing temperature [6, 28, 29, 36]. Since the samples were not mechanically restrained before the tests, no stress had evolved and no cracking had occurred. Autogenous shrinkage, whatever magnitude it had, proceeded freely without any induction of damage. No microcracks were observed on the specimens, which is also demonstrated in Fig. 9 with a perfect linear behavior on mature AAMK during cyclic loading.

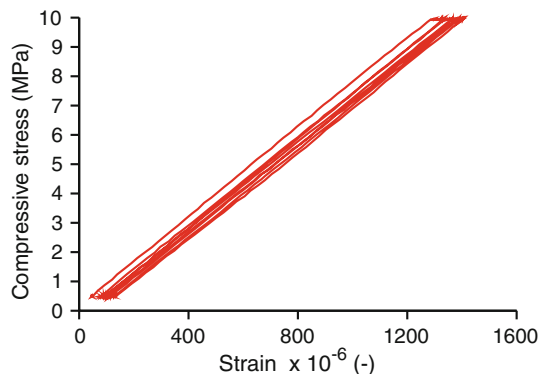


Fig. 9 A characteristic stress–strain plot of a AAMK prism 40 × 40 × 160 mm loaded uniaxially. Five loading/unloading cycles are shown, testifying linear dependence

Drying shrinkage is the well-known phenomenon for porous materials, where alkali-activated materials are of no exception. Exposing AAFA and AAMK samples to RH ≈ 30% led to the introduction of moisture gradients, shrinkage, and consequent tensile stress. Figure 10 demonstrates this fact on alkali-activated pastes after the exposure of approximately 1 year to RH ≈ 30%. These ambient-cured AAFA samples exhibit crack formation and propagation while the heat-cured AAMK sample seems to be free of macrocracks.

Introducing aggregates into shrinking alkali-activated material efficiently mitigates the macrocrack formation and the overall shrinkage [40, p 430]. The results have indicated that compressive strength steadily increases over years without any notion of the deterioration or crack formation on AAFA concrete under RH ≈ 30% [8].

Elasticity evolution during alkali activation process

The combination of a volumetric model, intrinsic elastic properties and a two-scale homogenization allows us to compute the evolution of elasticity during the alkali activation process. The upscaling starts from the solid gel particle and the moduli are matched exactly at the N-A-S-H level, see Fig. 11. It is evident from the paste moduli that a certain DoR must proceed before the gel interconnects the unreacted material. Introducing lower and upper percolation bounds, DoR_{LB}, DoR_{UB}, a solid percolation fraction is determined as

$$p = \frac{DoR - DoR_{LB}}{DoR_{UB} - DoR_{LB}}, \quad 0 \leq p \leq 1. \tag{12}$$

The elastic moduli from the N-A-S-H level are multiplied with *p*. From the macroscale tests, the bounds were

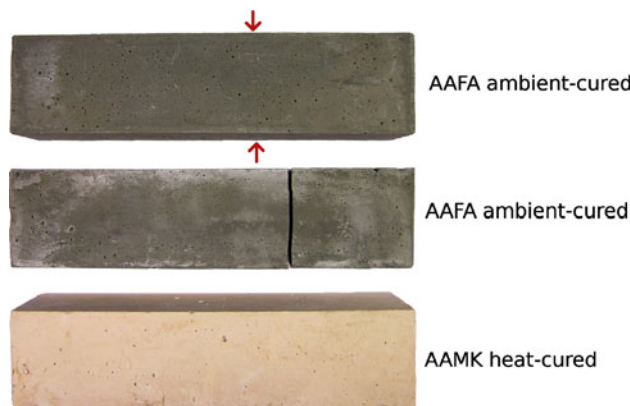
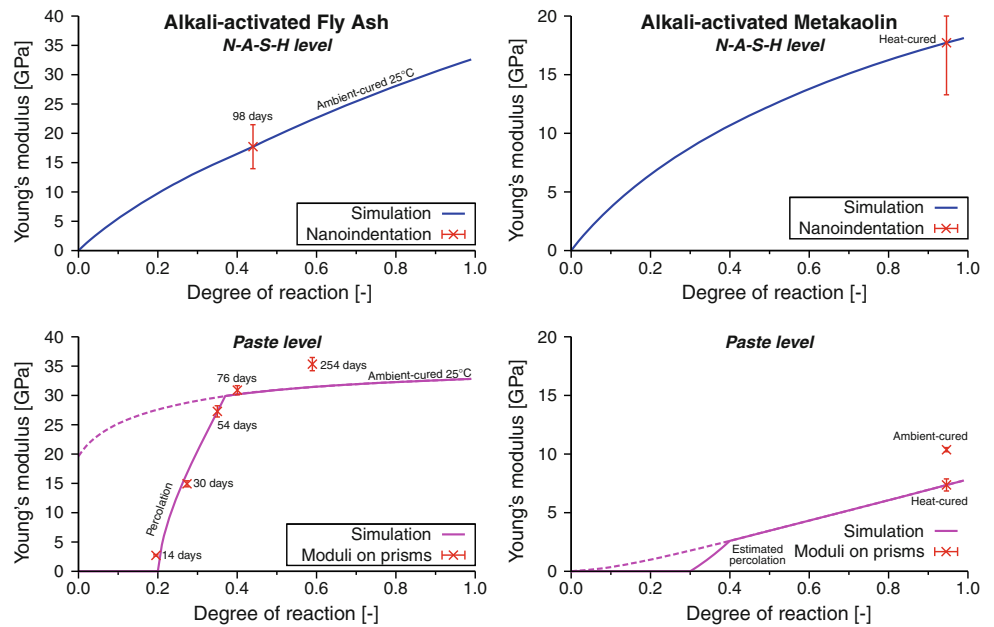


Fig. 10 Drying shrinkage on ambient-cured AAFA and heat-cured AAMK samples when exposed to RH ≈ 30%. An arrow on the prism 40 × 40 × 160 mm shows a visible microcrack which will propagate and later disintegrate the AAFA sample. Efflorescence on the surface originates from carbonation of excessive alkalis, which are carried to the surface in a moisture-gradient environment

Fig. 11 Simulated and measured Young's moduli on the levels of N-A-S-H gel and paste, for both AAFA and AAMK materials. *Dashed lines* disregard solid percolation



fitted to $DoR_{LB} = 0.20$, $DoR_{UB} = 0.37$ for AAFA and nicely demonstrate a steep evolution of elasticity in this region. Both bounds will be a function of the activator content since more solid gel particles are needed to bridge a larger gap among unreacted particles. This is analogous to Portland cements, where more hydration is needed for a higher water-to-cement ratio to achieve the percolation threshold of solids [41]. Dashed lines show the results under the assumption of perfect bonding among the phases.

Since finite elasticity is aligned with a solid material, the evolution of compressive/tensile strength follows the same pattern. This was demonstrated by Chen et al. [42], who found a steep gain of compressive strength when the material passed DoR between 0.15 and 0.35, depending on KOH molarity. The percolation thresholds are close to their values, which supports the view of dominating percolation mechanisms in the N-A-S-H gel formation.

Figure 11 also captures statistics; nanoindentation results are gathered from 500–700 indents [21] and cyclic load was applied on three prisms $40 \times 40 \times 160$ mm. The paste modulus of AAFA at 254 days is underestimated by 13%. The main reason probably lies in selective dissolution of fly ash, where remaining mullite has a high Young modulus of 230 GPa [37] and boosts the stiffness of the fly ash skeleton considerably. Another reason could be the assumptions underlying continuum micromechanical methods; a strong interaction among fly ash particles violates the homogeneous strain field around them. Also, N-A-S-H gel undergoes aging and rearrangement, changing the porosity distribution, the parameter γ , and possibly the intrinsic elasticity of a fictitious solid gel particle.

Figure 11 also provides the evolution of moduli for AAMK with experimental data on mature samples. Lower and upper percolation bounds were estimated. The heat-cured mature AAMK yielded a lower modulus than the ambient-cured counterpart, which could be explained micromechanically by changing the intrinsic elasticity of the solid gel particle or the parameter γ . Also, accelerated aging of activated metakaolin at elevated temperatures proved the gel transformation to Na-P1 zeolites [3, p 148], which would affect elasticity as well.

The elastic moduli for mature AAMK, found in the range of 7.37–10.37 GPa, correspond well with literature data; 2.5–5.5 GPa [32], 1–6 GPa [43], and up to 9.22 GPa [44]. On the contrary, the moduli for AAFA pastes are scarce in literature. Our colleague reported a dynamic modulus of 23.02 GPa for the AAFA paste after 308 days of curing at ≈ 22 °C [29].

More data exist for AAFA concrete; dynamic modulus of 22.15 GPa (also measured tangent static modulus of the same specimen 21.0 GPa) after 124 days of curing at ≈ 22 °C, attaining 24.6 GPa after 482 days [29]. Wongpa et al. [36] obtained chord moduli of 5.6–16.9 GPa on concrete with substantial cracks and Wallah and Rangan [6] reported tangent instantaneous moduli of 21.1–29.6 GPa for concrete. Considering concrete with 30 GPa, aggregate's moduli of 40 GPa and their volume fraction of 0.85, the AAFA paste should have 9.1 GPa using the Mori–Tanaka method. We hypothesize that such low moduli for the AAFA paste are caused by microcracks in the AAFA paste, which are unable to close up contrary to self-healing effects and carbonation in Portland-based systems.

Certain comparison also exists with the unpublished previous experiments, which did not prevent water evaporation by mould covering and sealing the samples during curing. Such measurements indicated much lower tangent moduli of mature AAFA pastes; 6.1 ± 1.8 GPa for ambient-cured and 8.35 ± 1.7 GPa, 11.4 ± 0.2 GPa for heat-cured specimens with similar compositions. The majority of previous AAFA pastes developed visible cracks on the surface, which apparently strongly reduced the specimen's moduli.

Relation to selected alkali activation models

The presented multiscale model shows no significant contradictions to existing models of alkali activation, especially due to a different approach and stand-point. The current model contributes to the chemically based models by treating the gel as an agglomeration of solid gel particles. Such a representation is advantageous in the micromechanical model, however, the shape of a solid gel particle can be almost arbitrary, intermixed with nanoporosity. The model of Barbosa et al. perfectly fits for the nanostructure of N-A-S-H gel [45].

Although N-A-S-H gels, originating from AAFA or AAMK, yield similar stiffnesses on the submicrometer scale [21], their nano-particulate structure appears to be micromechanically different. The N-A-S-H level shows significant variations in stiffness for a fictitious solid gel particle, which could be linked to gelation, reorganization and polymerization steps identified in a conceptual model of Duxson et al. [1] or Criado et al. [11]. More research is needed to validate the hypothesis about the same N-A-S-H gel nanostructure in AAFA and AAMK materials, even though TEM samples under high vacuum revealed very similar N-A-S-H morphologies [1].

A descriptive model of alkali activation of fly ash [12] reveals more detailed reaction mechanisms than quantified here. N-A-S-H gel, as the main reaction product, is not distributed only around fly ash as a precipitate but also fills capillary porosity as a true gel. Good adhesion to the majority of materials is a consequence of such gel formation [3]. Changing the reaction orders due to the deposition of reaction products [13] and depletion of the alkali potential remains unaddressed in the presented model and the whole kinetics must be provided externally.

Low chemical binding of capillary water to N-A-S-H gel testifies that water plays a major role for the dissolution and transport of dissolved glasses, but not to be consumed substantially [1]. Gelation, reorganization, and polymerization return water back to the system. The excess of water during curing is not beneficial as opposed to Portland-based systems [7]. Dry curing was found to remove water and to

stop reactions prematurely [7]. Introducing Ca-rich materials into the system would combine Figs. 5a,b and would reduce capillary porosity. It is known that high alkalinity hinders the dissolution of $\text{Ca}(\text{OH})_2$ and prevents, to some extent, the formation of C-(A)-S-H gels [3, p 84].

Conclusions

The application of elastic micromechanics with the volumetric model of alkali activation leads to the following conclusions:

1. Water is consumed only marginally during the alkali activation process in both AAFA and AAMK systems. For this reason, the volume fraction of a liquid activator governs the final open porosity. This is critical especially for activated metakaolin, where large quantities of the activator are needed for proper workability.
2. Introducing Ca in the system would be beneficial for possible water binding to C-(A)-S-H gels thus reducing capillary porosity.
3. Micromechanical analysis revealed elastic differences in the N-A-S-H gel composition on the nanometer scale. A fictitious solid gel particle in AAMK is almost twice as compliant as in the AAFA counterpart. Also, AAMK contains almost three times less porosity associated with the N-A-S-H level than AAFA. Commonly used methods, such as NMR, FTIR, or XRD, may provide only indirect evidence. This topic needs more research with consequences to stability and durability of AAFA and AAMK materials.
4. Percolation plays a significant role during the alkali activation process. A slow reaction kinetics at ambient temperature combined with a high percolation threshold implies slow hardening especially for AAFA.
5. The results testify that curing temperature has a small effect on the total open porosity or the micromechanical properties of mature AAFA [21]. However, ambient curing creates more coarse pores which is probably related to N-A-S-H gel's syneresis.
6. The presented model for alkali activation is general enough to accommodate different activated materials, various compositions of the activator and mixture proportions. Recalibration and kinetic monitoring must be executed prior to modeling.

Acknowledgements This research was supported by the Czech Science Foundation under the grant GAP104/10/2344, GA103/09/1748 and MSM 6046137302. M. Vokáč from Klokner Institute, CTU in Prague is greatly acknowledged for conducting precise measurements of elastic moduli.

References

1. Duxson P, Fernández-Jiménez A, Provis JL, Lukey GC, Palomo A, van Deventer JSJ (2007) *J Mater Sci* 42(9):2917. doi:[10.1007/s10853-006-0637-z](https://doi.org/10.1007/s10853-006-0637-z)
2. Pacheco-Torgal F, Castro-Gomes J, Jalali S (2008) *Constr Build Mater* 22(7):1305
3. van Deventer JSJ (eds) (2009) *Geopolymers: structures, processing, properties and industrial applications*, 1st edn. Woodhead Publishing Ltd, Cambridge
4. Fernández-Jiménez A, Palomo A (2005) *Cem Concr Res* 35:1984
5. Hardjito D, Rangan BV (2005) Research report gc 1. Faculty of Engineering, Curtin University of Technology, Perth
6. Wallah SE, Rangan BV (2006) Research Report GC 2. Curtin University of Technology, Perth
7. Kovalchuk G, Fernandez-Jimenez A, Palomo A (2007) *Fuel* 86(3):315
8. Škvára F, Kopecký L, Šmilauer V, Bittnar Z (2009) *J Hazard Mater* 168:711
9. Davidovits J (2001) In: Metha PK (ed) *Concrete technology, past, present and future*, Proceedings of V. Mohan Malhotra Symposium, ACI, p 383
10. van Jaarsveld JGS, van Deventer JSJ, Lorenzen L (1997) *Miner Eng* 10(7):659
11. Criado M, Fernández-Jiménez A, Palomo A (2010) *Fuel* 89(11):3185
12. Fernández-Jiménez A, Palomo A, Criado M (2004) *Cem Concr Res* 35:1204
13. Chen C, Gong W, Lutze W, Pegg I, Zhai J (2011) *J Mater Sci* 46(3):590. doi:[10.1007/s10853-010-4997-z](https://doi.org/10.1007/s10853-010-4997-z)
14. Provis JL, van Deventer JSJ (2007) *Chem Eng Sci* 62:2309
15. Powers TC, Brownyards TL (1948) *Studies of physical properties of hardened portland cement paste*. Bulletin 22, Research Laboratories of the Portland Cement Association, Chicago
16. Bernard O, Ulm FJ, Lemarchand E (2003) *Cem Concr Res* 33(9):1293
17. Šmilauer V, Bittnar Z (2006) *Cem Concr Res* 36(9):1708
18. Pichler C, Lackner R, Mang HA (2007) *Eng Fract Mech* 74:34
19. Grassl P, Jirásek M (2010) *Int J Solids Struct* 47(7–8):957
20. Šejnoha M, Zeman J (2008) *Int J Eng Sci* 46(6):513; special Issue: Micromechanics of Materials. doi:[10.1016/j.ijengsci.2008.01.006](https://doi.org/10.1016/j.ijengsci.2008.01.006)
21. Němeček J, Šmilauer V, Kopecký L (2011) *Cem Concr Compos* 33(2):163
22. Perera D, Uchida O, Vance E, Finnie K (2007) *J Mater Sci* 42(9):3099. doi:[10.1007/s10853-006-0533-6](https://doi.org/10.1007/s10853-006-0533-6)
23. Zaoui A (2002) *J Eng Mech* 128(8):808
24. Mori T, Tanaka K (1973) *Acta Metall* 21(5):1605
25. Hill R (1965) *J Mech Phys Solids* 13:189
26. Palomo A, Grutzeck MW, Blanco MT (1999) *Cem Concr Res* 29:1323
27. Provis JL, van Deventer JSJ (2007) *Chem Eng Sci* 62:2318
28. Rodríguez E, de Gutiérrez RM, Bernal S, Gordillo M (2009) *Rev Fac Ing* 49:30
29. Strnad T (2011) PhD thesis, Faculty of Civil Engineering, Czech Technical University (in Czech)
30. Rahier H, Denayer JF, van Mele B (2003) *J Mater Sci* 38:3131. doi:[10.1023/A:1024733431657](https://doi.org/10.1023/A:1024733431657)
31. Powers TC (1958) *J Am Ceram Soc* 41(1):1
32. Duxson P, Provis JL, Lukey GC, Mallicoat SW, Kriven WM, van Deventer JSJ (2005) *Colloids Surf A* 269:47
33. Scherer GW (1999) *Cem Concr Res* 29(8):1149
34. Constantinides G, Ulm FJ (2007) *J Mech Phys Solids* 55:64
35. Jennings HM (2008) *Cem Concr Res* 38(3):275
36. Wongpa J, Kiattikomol K, Jaturapitakkul C, Chindaprasirt P (2010) *Mater Des* 31(10):4748
37. Matsunaga T, Kim JK, Hardcastle S, Rohatgi PK (2002) *Mater Sci Eng A* 325(1–2):333
38. van Deventer J, Provis J, Duxson P, Lukey G (2007) *J Hazard Mater* 139(3):506
39. Neubauer CM, Jennings HM, Garboczi EJ (1997) *Cem Concr Res* 27(10):1603
40. Neville AM (1997) *Properties of concrete*. Wiley, New York
41. Šmilauer V (2011) *Multiscale hierarchical modeling of hydrating concrete*. Saxe-Coburg Publications, Stirling
42. Chen C, Gong W, Lutze W, Pegg I (2011) *J Mater Sci* 46(9):3073. doi:[10.1007/s10853-010-5186-9](https://doi.org/10.1007/s10853-010-5186-9)
43. Duxson P, Mallicoat SW, Lukey GC, Kriven WM, van Deventer JSJ (2007) *Colloids Surf A* 292(1):8
44. Kirschner AV, Harmuth H (2004) *Ceram-Silik* 48(3):117
45. Barbosa VFF, MacKenzie KJD, Thaumaturgo C (2000) *Int J Inorg Mater* 2(4):309

Part III

Paper 2

Authors: Petr Hlaváček, Vít Šmilauer, Rostislav Šulc, Lubomír Kopecký,
František Škvára

Title: Elastic properties of geopolymer concrete based on fly-ash

Source: Novel Developments and Innovation in Cementitious Materials

Conference: 31st Cement and Concrete Science Conference

Year: 2011

Elastic properties of geopolymer concrete based on fly-ash

P. Hlaváček, V. Šmilauer, R. Šulc and L. Kopecký
Department of Mechanics, Czech Technical University in Prague

F. Škvára
Department of Glass and Ceramics, Institute of Chemical Technology in Prague

ABSTRACT

Alkali-activation is a reaction process between strong alkaline liquid and solid aluminosilicate material. In presented paper, a micromechanical model-based prediction of Young's modulus for alkali-activated concrete is formulated. The micromechanical model describes the changes in composition of activated material during alkali reaction and predicts the evolution of elastic properties of the paste and concrete in time. Four-scale homogenization builds on intrinsic elastic data for individual components at each level. Elastic modulus of fly ash-based concrete is several times lower than that predicted. This discrepancy was fixed by introducing damage parameter to the paste level, which quantifies crack formation due to aggregates' restraints. Low self-healing ability of the studied calcium-deficient system mitigates crack closure with further reaction.

1. Introduction

The main objective of this work is to create a micromechanical model describing the development of microstructure during hardening of concrete based on alkali-activated fly ash. The microstructure evolution model at the level of paste was introduced previously (Smilauer et al., 2011). However, more detailed experiments showed that elasticity of hardened concrete is overestimated when compared to micromechanical models. We believe, that such inconsistency can be explained with introduction of cracks in the alkali-activated paste, which is quantified via damage parameter.

Alkali activation presents a reaction between a strong alkaline liquid and a solid aluminosilicate material (Duxson et al., 2007). The product is known as inorganic polymer, geopolymer or alkali-activated cement (Pacheco-Torgal, 2008; van Deventer 2009). The alkali-activated materials show excellent performance in acid environment, fire resistance, low drying shrinkage, improved durability, no alkali-silica reaction, freeze/thaw performance or lower creep induced by mechanical load, when compared to ordinary Portland concrete (Wallah and Rangan, 2006).

For deeper understanding of the alkali reaction, several chemistry-based models were introduced (Davidovits, 2001; Criado et al., 2010; Chen et al., 2011). The basic mechanism of geopolymer formation was described by Fernández-Jiménez (Fernández-Jiménez et al., 2006). More advanced structural models were introduced by Y. Zhang (Zhang et al., 2009) or J. L. Provis (Provis and van Deventer, 2007).

Another approach for material research is based on micromechanics, building on chemical models and introducing intrinsic properties of chemical phases on various scales. In addition to purely chemical description, these models can reveal phase arrangement or mutual interaction on different scales, and can be predictive for many engineering properties.

Elasticity presents one of the most developed frameworks of micromechanical models, which is employed in this analysis. Fly ash-based concrete is described on four scales; each scale taking into account relevant material phases. By doing so, the macroscopic elastic modulus during alkali-activation process is predicted. Since no fitting or calibrating procedure is involved in elasticity upscaling, discrepancies between experimental and simulated data reveal other mechanisms which can be taken into account in improved models. Low experimental elastic moduli of concrete demonstrate stiffness reduction of paste, which is caused by excessive restrained shrinkage, crack formation and low self-healing effects of fly-ash binder, see Figure 1.

2. Materials and methods

The fly ash class F from Opatovice brown coal power station, the Czech Republic, was used as the source material for alkali-activation. Specific Blaine surface is 210 m²/kg, the chemical composition is given in Table 1.

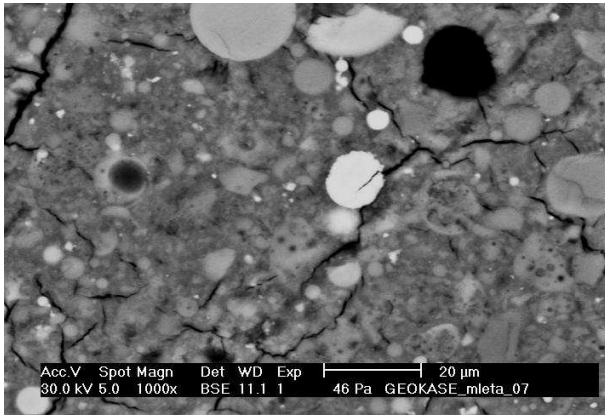


Figure 1. Fly ash paste with visible microcracks. Image by L. Kopecký

Fly ash was activated in the form of paste, or further intermixed with aggregates to create concrete. Their compositions, recalculated per 1 m^3 , are given in Table 2.

Table 1. The chemical composition of fly ash (wt%)

	SiO ₂	Al ₂ O ₃	Fe ₂ O ₃	CaO	TiO ₂	K ₂ O
Fly ash	51.9	32.8	6.3	2.7	1.89	2.12

Table 2. Composition of fly ash based concrete, data from (Strnad, 2010) and fly ash paste, data from (Šmilauer et al., 2011). Content is recalculated per 1 m^3 . Note, the sodium water glass consist of 34.3% dry matter and 65.7% water.

Component	Concrete (1 m^3)	Paste (1 m^3)
Fine aggregates 0/4mm	695 kg	–
Coarse aggregates 4/8mm	225 kg	–
Coarse aggregates 8/16mm	958 kg	–
Fly ash, class F	400 kg	1144 kg
Sodium water glass	167.8 kg	441.8 kg
Sodium hydroxide	29.4 kg	80.1 kg
Aluminium hydroxide	2.13 kg	–
Plasticizer, Glenium AC 40	8 l	–
Air Entrainer	1.2 l	–
Added Water	52.2 l	85.9 l
Water / fly ash ratio	0.33	0.34
Bulk density	2488 kg/m ³	1752 kg/m ³

The size of paste specimens was 40x40x160 mm (Šmilauer et al., 2011) while the size for concrete was 100x100x500 mm (Strnad, 2010). The concrete samples were cured under ambient conditions; temperature 22°C, relative humidity 62%. The paste samples were covered to prevent the water evaporation and cured also at room temperature.

Continuum micromechanics provides the framework in which elastic properties of heterogeneous microscale components are homogenized to the macroscale (Zaoui A., 2002). Prior to analysis, it is crucial to define a representative volume element (RVE), which includes all components and well describes the morphology. Certain restrictions in terms of scale separation exist on the RVE size (Zaoui A., 2002); RVE must be substantially smaller than the macroscale body, which allows imposing homogeneous boundary conditions over RVE boundaries. This leads to a constant stress/strain field in individual microscale components of ellipsoidal shapes.

In our case, the elastic homogenization analysis is divided into four levels according to the resolution. Relevant chemical/physical phases are mentioned:

1. level Solid Gel Particles + water → N-A-S-H gel
2. level N-A-S-H gel + fly ash + voids → Paste
3. level Paste + fine aggregates → Mortar
4. level Mortar + coarse aggregates → Concrete

Effective elastic properties are obtained through strain averaging over the relevant phases (Zaoui A., 2002). Considering isotropic spherical inclusions perfectly bonded with a matrix leads to the estimation of effective bulk and shear moduli. Mori-Tanaka homogenization method is employed for level 1,3, and 4, while self-consistent scheme is justified due to high porosity at the paste level.

Secant elastic moduli of paste and concrete samples were measured several times during slow hardening under ambient curing conditions. The Young's modulus was obtained from Hooke's law:

$$E = \frac{\Delta\sigma}{\Delta\varepsilon} = \frac{\sigma_a - \sigma_b}{\varepsilon_a - \varepsilon_b}, \quad (1)$$

where σ_a is upper loading limit, approximately one third of compressive strength and σ_b is the lower loading limit standardized as 0.5 MPa, $\varepsilon_a, \varepsilon_b$ are the corresponding measured strains. The results are introduced in Table 4 and compared with the simulations in Figure 4.

3. Results and discussion

Evolution of Young's modulus for level 1 and 2 was validated previously; see Figure 2 for results (Šmilauer et al., 2011). The predicted elastic modulus in the early stage of the alkali reaction is compared with the measured data overestimated; see the dashed line in Figure 2. The percolation theory was introduced to reduce the elasticity in the early stage, (Šmilauer et al., 2011).

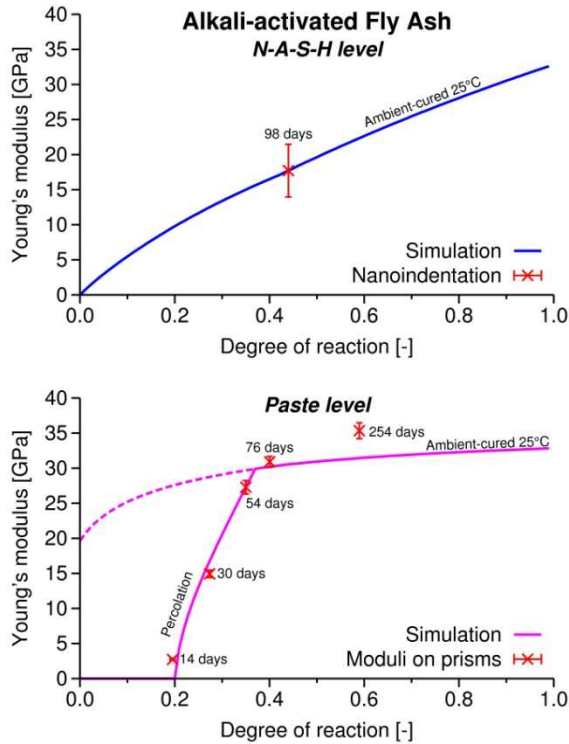


Figure 2. Measured and simulated elastic moduli of the alkali activated fly ash at the levels of N-A-S-H gel and paste.

Since experiments on paste and concrete were carried out under different curing temperatures, Arrhenius equation is used to find equivalent time

$$\tau_e(T_0) = \tau(T) \exp\left[\frac{E_a}{R} \left(\frac{1}{T_0} - \frac{1}{T}\right)\right], \quad (2)$$

where T and T_0 are actual and reference temperatures, R is the universal gas constant, $R=8.314 \text{ J}/(\text{K mol})$, E_a is the activation energy of fly ash. Calorimetric measurements found $E_a = 86.2 \text{ kJ}/\text{mol}$ on alkali-activated fly ash (Škvára et al., 2009). To demonstrate a strong effect of temperature, reaction rate from 20°C to 85°C changes about 400 times.

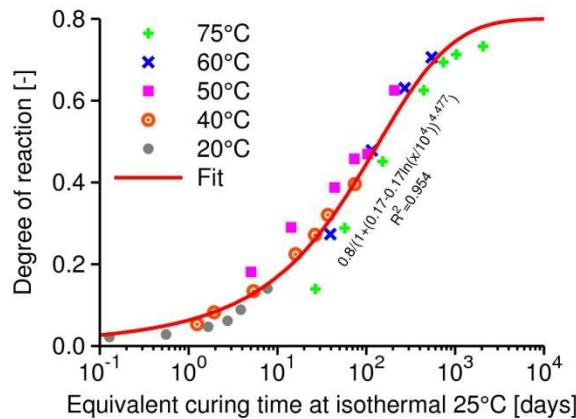


Figure 3. The development of DoR for alkali activated fly ash by 7.5 M KOH obtained by time scaling according to Arrhenius equation. The evolution of DoR is recalculated to a reference temperature 25°C , the data were measured in isothermal temperature range $20\text{--}75^\circ\text{C}$.

Degree of reaction is used as a microstructural parameter for recalculating reaction time. The evolution of DoR is recalculated from experimental data of Chen et al. (Chen et al., 2011). Figure 3 displays reaction progress for equivalent curing time at isothermal 25°C .

Table 3 summarizes important intrinsic properties of fly ash-based concrete composite. Details on solid gel particles and fly ash skeleton have been published elsewhere (Šmilauer et al., 2011). Young's modulus for fine aggregates, originated from Dobříň, the Czech republic was estimated as 60 GPa. In case of coarse aggregates the rock spilite was utilized, Young's modulus of spilite is known as 70 GPa.

Table 3. Intrinsic elastic properties used in the elastic homogenization for four levels.

Material	Young's modulus	Poisson's ratio
Fly ash skeleton	105 GPa	0.2
Voids	0.001 GPa	0.001
Water filled pores	0.001 GPa	0.499924
Fine aggregates	60 GPa	0.2
Coarse aggregates	70 GPa	0.2

Table 4 contains experimental data on concrete elastic moduli (Strnad, 2010). These were measured by mechanical tests.

Table 4. Measured Young's moduli on the concrete specimens during the hardening period. Data are taken from T. Strnad (Strnad, 2010).

Age of concrete	Young's modulus	Compressive strength
7 days	1.0 GPa	11.3 MPa
14 days	9.0 GPa	19.8 MPa
28 days	13.5 GPa	25.1 MPa
70 days	18.2 GPa	-
130 days	21.0 GPa	-

The four-level multiscale homogenization predicts evolution of elasticity, depicted in Figure 4 as the curve without any damage to the paste matrix. Discrepancy between measured data, denoted with crosses, and multiscale prediction can be attributed to crack formation in the alkali-activated binder, see Figure 1 for evidence. These cracks reduce overall stiffness of the matrix to significantly lower values, thus influencing elasticity at mortar and concrete levels. Initial percolation threshold between Figure 2 and Figure 4 was calibrated due to different composition and solid-to-solid spacing.

High autogenous shrinkage of alkali-activated paste was determined as 4240 microstrains after 28 days of ambient curing (Strnad, 2010). When no drying and no external restraints exist on a system, the autogenous shrinkage produce only minor cracks due to

heterogeneous composition of fly-ash composite. However, further restrains in the form of aggregates, which are present in the volume fraction 62%, present substantial framework to introduce large cracks in the alkali-activated paste. This phenomenon is quantified with the damage parameter, which is defined as:

$$D = 1 - \frac{\tilde{E}}{E}, \quad (3)$$

where \tilde{E} represents the elastic modulus of the damaged material and E is the theoretical elastic modulus of crack-free material.

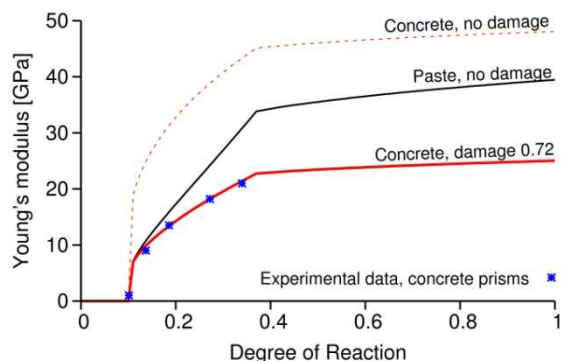


Figure 4. The development of elastic modulus during hardening of concrete based on the alkali-activated fly ash.

Micromechanical predictions can be reasonably calibrated when imposing a constant damage parameter $D=0.72$ to the paste level. By doing so, the paste elasticity is reduced to 28% and micromechanical methods correspond well to experimental concrete moduli.

Elastic moduli of heat-cured fly ash-based concrete were previously reported between 23 – 30.8 GPa (Hardjito and Rangan, 2005), determined from mechanical tests. Our results are consistent and due to ambient curing procedure attain the lower bound of those concretes.

4. Conclusion

Alkali-activated composite materials based on low calcium fly ash (class F) reveal crack formation in the paste during their hardening. High autogeneous shrinkage of the paste, complemented with external restrains of aggregates, is the driving mechanism of crack formation. A similar mechanism exists in OPC, but the self-healing effect ensures crack closure with further hydration. Since N-A-S-H gel has no characteristic porosity, further reaction is ineffective in crack closure. This leads to stiffness reduction of fly ash-based concrete, which led to estimation of damage parameter in the matrix to 0.72. Even such the high damage parameter is not manifested with sample disintegration, testified with hundreds of our experiments on fly ash-based concrete.

References

- Chen, C., Gong, W., Lutze, W., Pegg, I., Zhai, J., 2011. Kinetics of fly ash leaching in strongly alkaline solutions. *Journal of Materials Science*, 46(3):590.
- Criado, M., Fernández-Jiménez, A., Palomo, A., 2010. Alkali activation of fly ash. Part III: Effect of curing conditions on reaction and its graphical description. *Fuel*, 89(11): 3185-3192.
- Davidovits, J., 2001. In: Metha PK (ed) *Concrete technology, past, present and future*. Proceedings of V. Mohan Malhotra Symposium, ACI, p 383.
- Duxson, P., Fernández-Jiménez, A., Provis, J.L., Lukey, G.C., Palomo, A., van Deventer, J.S.J., 2007. Geopolymer technology: the current state of the art. *Journal of Materials Science*, 42(9):2917.
- Fernández-Jiménez, A., Palomo, A., Sobrados, I., Sanz, J., 2006. The role played by the reactive alumina content in the alkaline activation of fly ashes. *Microporous and Mesoporous Materials*, 91:111-119.
- Hardjito, D. and Rangan, B. V., 2005. *Development and Properties of Low-Calcium Fly Ash-based Geopolymer Concrete*, Research Report GC1, Faculty of Engineering, Curtin University of Technology, Perth, Australia.
- Milestone, N.B., 2006. Reactions in cement encapsulated nuclear wastes: need for toolbox of different cement types. *Advances in Applied Ceramics*, 105(1):13-20.
- Provis, J.L., van Deventer, J.S.J., 2007. Geopolymerisation kinetics. 2. Reaction kinetic modelling. *Chemical Engineering Science*, 62(9): 2318-2329.
- Škvára, F., Kopecký, L., Šmilauer, V., Bittnar, Z., 2009. Material and structural characterization of alkali activated low-calcium brown coal fly ash. *Journal of Hazardous Materials*, 168:711-720.
- Šmilauer, V., Hlaváček, P., Škvára, F., Šulc, R., Kopecký, L., Němeček, J., 2011. Micromechanical multiscale model for alkali activation of fly ash and metakaolin. *Journal of Materials Science*, published online.
- Strnad, T., 2010. *Physical – mechanical properties of a material on the basis of alkaline activated fly ash*. PhD. Thesis, CTU Prague.
- Zaoui, A., 2002. Continuum Micromechanics: Survey, *Journal of Engineering Mechanics* 128(8):808.
- Zhang, Y., Li, Z., Sun, W., Li, W., 2009. Setting and Hardening of Geopolymeric Cement Pastes incorporated with Fly Ash. *ACI Materials Journal*, 106(5): 405-412.

Part IV

Paper 3

Authors: Vít Šmilauer, Petr Hlaváček, Pavel Padevět

Title: Micromechanical analysis of cement paste with carbon nanotubes

Journal: Acta Polytechnica

Number: 6

Volume: 52

Year: 2012

Micromechanical Analysis of Cement Paste with Carbon Nanotubes

Vít Šmilauer, Petr Hlaváček, Pavel Padevět

Czech Technical University in Prague, Faculty of Civil Engineering, Department of Mechanics, Thákurova 7, 166 29 Prague 6, Czech Republic

Corresponding author: vit.smilauer@fsv.cvut.cz

Abstract

Carbon nanotubes (CNT) are an attractive reinforcement material for several composites, due to their inherently high strength and high modulus of elasticity. There are controversial results for cement paste with admixed CNT up to $500\ \mu\text{m}$ in length. Some results show an increase in flexural or compressive strength, while others showing a decrease in the values. Our experiments produced results that showed a small increase in fracture energy and tensile strength. Micromechanical simulations on a CNT-reinforced cement paste $50 \times 50\ \mu\text{m}$ proved that CNT clustering is the crucial factor for an increase in fracture energy and for an improvement in tensile strength.

Keywords: carbon nanotubes, cement hybrid material, micromechanics, fracture energy.

1 Introduction

Worldwide production of cement has increased significantly in recent years, due to the growing demand for concrete. In 2010, $3.3 \cdot 10^9$ tons of cement were produced, which is three times the quantity of $1.1 \cdot 10^9$ tons produced in 1990. For reasons of sustainability and profitability, secondary cementitious materials have been introduced into the binder, reducing the amount of Portland clinker in the cement. A further reduction can be made if the strength of the hydrated cement increases.

Carbon nanofibers (CNF) and carbon nanotubes (CNT) are a feasible approach to the production of a high strength binder, as has been demonstrated for composites [3, 19] and specifically for cement pastes [2, 4, 5, 9, 12]. Theoretical and experimental studies have indicated that CNT exhibit Young modulus from 180 to 588 GPa and tensile strength in the range between 2000 and 6140 MPa [10]. Both CNT and CNF as admixtures are very difficult to distribute uniformly, even within a small volume of cement paste. Flocculation make it impossible to obtain improved properties of composite materials, unless a special treatment is applied.

It is a challenging task to achieve good dispersion of CNT/CNF in a cement matrix. A simple powder mixing procedure leads to poor dispersal of the carbon nanomaterials in a cement paste. For this reason, Sanchez and Ince proposed adding silica fume to cement to increase the dispersiveness of CNF [15]. Dispersion of CNT/CNF in water using surfactants is another method, and is a widely-used way to introduce carbon nanomaterials into polymers [2]. However, most surfactants and additives interfere with the hydration reaction of cement, and usually prolong

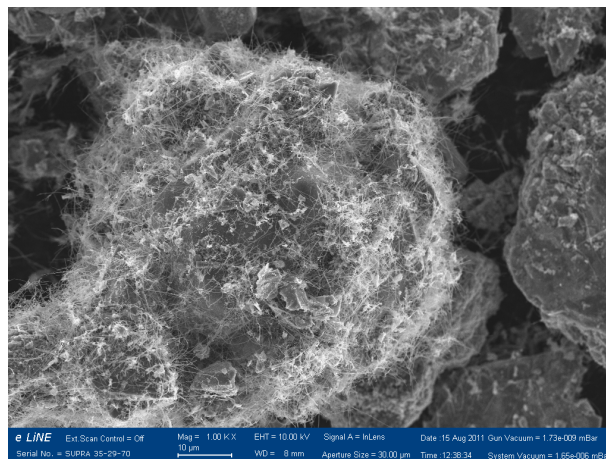


Figure 1: CNT synthesized on the surface of a cement grain. The image is $115\ \mu\text{m}$ in width. Image by K. Hruška, Institute of Physics ASCR, Prague.

the cement setting and hardening times.

Another way to enhance the dispersiveness of CNT/CNF is by functionalizing them. The carboxyl or hydroxyl groups attached to the surface of carbon that form during oxidation treatment can create bonds between the matrix and carbon nanomaterials. Functionalized CNT have already been proven to influence the mechanical properties of hydrated cement paste [2, 5].

Another method uses CNT directly synthesized on the surface of cement grains [12], see Figure 1. Cement hybrid material (CHM) of this type can easily be blended with conventional cement. This procedure guarantees dispersion of CNT in the cement matrix. It has been reported that even a small mass fraction of $\text{CNT}/\text{cement} = 0.005$ helped to increase flexural strength by 22 % [5].

CNT length (μm)	w/c	Compressive s. (MPa)		Flexural s. (MPa)		Ref.
		Plain	CNT	Plain	CNT	
< 10	P 0.30	38.3 ± 8.2	61.8 ± 0.8	2.3 ± 0.4	2.3 ± 0.2	[2]
< 30	P 0.30	—	—	9.2	12.6	[4]
< ~ 10	M 0.40	28.9	54.3	6.0	8.23	[8]
< 500	P 0.45	52.3 ± 0.7	62.1 ± 1.4	6.7 ± 0.1	8.4 ± 0.2	[5]
< 100	P 0.50	—	—	5.5	7.2	[9]
< ~ 5	P —	49	56	16	8	[12]

Table 1: Summary of published data on strength gain when CNT is added to cement. P-paste, M-mortar.

Reports on improvement of compressive and flexural strength when un/functionalized CNT is added to a cement paste are inconsistent across the literature. For example, a decrease of more than 30% in compressive strength has been reported [2]. Table 1 shows the most optimistic claimed improvements which were achieved by adding certain amounts of CNT/CNF to cement paste or mortar, measured after 28 days of hardening.

In addition, data from Table 1 demonstrates that even CNT shorter than $10 \mu\text{m}$ can be effective in providing added strength. This raises the question of the reinforcing mechanism. To shed the light on the mechanical effect of CNT, a series of experimental data was measured and micromechanical simulations were executed. The results are presented below.

2 Experiments

2.1 Materials

Ordinary Portland cement CEM I 42.5 R from Mokra, Czech Republic, was used as the source material for all specimens. The specific Blaine surface was $306 \text{ m}^2/\text{kg}$, the chemical composition of the relevant elements was CaO 65.6%, SiO₂ 19.0%, Fe₂O₃ 3.5%, MgO 1.1% by mass.

Cement hybrid material (CHM) with grown CNT on the surface was synthesized by a group from Aalto University, Finland, under the leadership of L. Nasibulina by the chemical vapor deposition method [13]. CNT growth occurred at about 600°C in a fluidized bed reactor, where acetylene served as the main carbon source due to its low decomposition temperature and its affordable price. The CNT grown on the cement particles are approximately 30 nm in diameter and up to $3 \mu\text{m}$ in length [11], and the specific surface area of CNT is about $10\text{--}20 \text{ m}^2/\text{g}$.

CHM has density $2.59 \text{ kg}/\text{m}^3$ and contains 30% of carbon by mass, which occupies 43% of the volume.

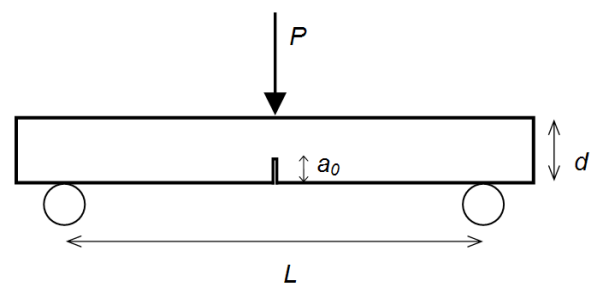


Figure 2: Layout of the three-point bending test used for fracture energy determination.

Table 2 summarizes the compositions of five experimental batches with the same water/binder ratio of 0.35. The batches cover feasible mixes potentially usable in concrete engineering. 0.2% Glenium ACE 40 superplasticizer was added to the binder mass. The superplasticizer contains 65% of water by mass, which was deducted from the total amount of water.

2.2 Casting and curing of the specimens

Hand stirring of each batch took three minutes, and consecutive vibration and form filling took an additional period of four minutes. Specimens $40 \times 40 \times 80 \text{ mm}$ in size were covered, and after 24 hours they were cured in a water bath at ambient temperature. At 30 days of hardening, the specimens were cut with a diamond saw into nine parts with approximate dimensions $13 \times 13 \times 80 \text{ mm}$.

The production of such small-size specimens by cutting from larger bodies is more efficient than direct casting into small molds. The casting and vibration of a small amount of material was found to be ineffective, and the quality of the specimens (including surface defects or material inhomogeneity) is significantly worse than the quality attained by hand-cutting from larger bodies.

Designation (mass %)	CEM I (g)	CHM (g)	Water (g)	Carbon/paste (vol %)
CEM 100 % + CHM 0 %	234.0	0	81.9	0
CEM 96.5 % + CHM 3.5 %	225.81	8.19	81.9	0.88
CEM 93 % + CHM 7 %	217.62	16.38	81.9	1.75
CEM 86 % + CHM 14 %	201.24	32.76	81.9	3.47
CEM 70 % + CHM 30 %	163.8	70.2	81.9	7.31

Table 2: Five batches of cement pastes with different amounts of CHM.

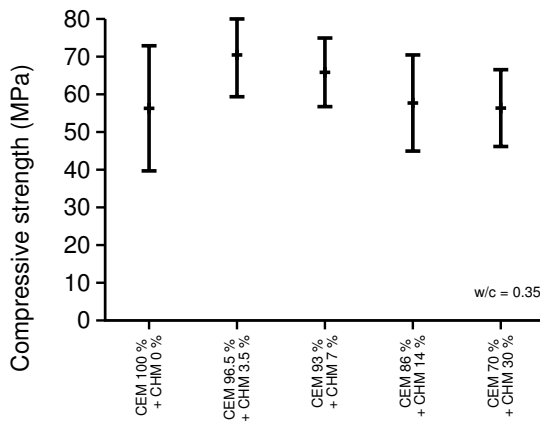


Figure 3: Compressive strength of a plain paste and pastes with admixed CHM.

In accordance with RILEM standards for mechanical testing [17], notches were cut in the middle of the beams to 45 % of the depth for subsequent fracture energy determination.

2.3 Determining the mechanical properties

The fracture energy, G_f , was determined according to the RILEM standard [17], see Figure 2 for the experimental scheme. At least five notched beams from one batch were used to obtain the statistical results.

The three-point bending test under a displacement-controlled regime gave access for the full load displacement curve on an MTS Alliance RT 30 electromechanical machine. The work of external force P is calculated as

$$W_f = \int_0^{u_f} P du \quad (1)$$

where u is the load-point displacement and u_f represents the final displacement at which the load is equal to zero. The average (effective) fracture energy in the ligament, according to the RILEM standard,

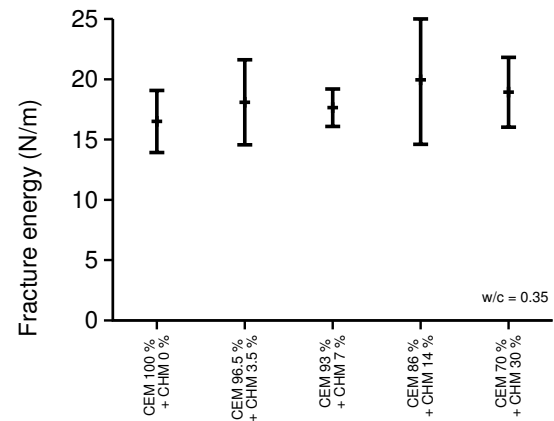


Figure 4: Fracture energy of a plain paste and pastes with admixed CHM.

is defined as

$$G_f = \frac{W_f}{b(d - a_0)} \quad (2)$$

where b is the thickness of the beam, d is the beam depth, and a_0 is the depth of the notch. The support span L was set to 50 mm.

The compressive strength was determined from two broken pieces of each beam. Thick metal pads 13×13 mm were put on the top and bottom surfaces, and the peak force was recalculated to the compressive strength.

2.4 Experimental results

Figure 3 shows the compressive strength of the hardened pastes at 30 days after the casting. Replacing 3.5 % cement with CHM leads to a 25 % increase in compressive strength, in our case from an average value of 56 MPa to an average of 70 MPa. This paste contains only 0.88 % of CNT by volume. Increased CHM dosage leads to a slight decrease in compressive strength.

Figure 4 depicts the evolution of fracture energy. The CHM samples exhibit an increase in fracture

Component	E (GPa)	ν	f_t (MPa)	G_f (N/m)
Porosity	0.2	0.02	—	—
Clinker	135	0.3	1800	118.5
Products	21.7	0.24	5.58	11.5
CNT	231	0.14	3000	200

Table 3: Elastic and fracture properties of the components.

energy even in a small amount of replacement. Replacing 3.5% of the cement by CHM causes a 14% increase in the fracture energy.

It should be added that a variation in CHM content has consequences for workability, paste density and porosity. The results indicate that the classical CNT pull-out or crack bridging mechanism does not occur. Microcrack shielding seems to be the most relevant mechanism operating in hardened cement paste reinforced by short CNT, giving only a slight increase in the fracture energy [7]. In contrast, PVA-reinforced cement-based composites with fibers several millimeters in length yield fracture energy that is higher by orders of magnitude [6]. This experimental finding is further supported by micromechanical simulations that show a certain increase in the upper-bound fracture energy.

3 Micromechanical simulations

2D micromechanical simulations aimed to reproduce the fracture energy from CNT-free and CNT-reinforced cement pastes and, in addition, to explore the role of clustering and CNT length. The CEMHYD3D cement hydration model generated the 3D microstructure of hydrated cement paste, from which a 2D slice $50 \times 50 \mu\text{m}$ was taken. Various chemical phases were reduced to three components; capillary porosity, clinker minerals and hydration products, which correspond mainly to C-S-H. For 30 days of hydration, the volume fractions yield to 14.2%, 11.6% and 74.2% respectively. The CNT volume fraction was considered as 3.47%, which corresponds to a composition of CEM 86% + CHM 14%.

CNT fibers were introduced as 1D truss elements, connecting particular nodes of 2D quadrilateral elements. Each fiber is represented by one finite element without intermediate hanging nodes, in order to simplify the model.

An isotropic damage material model is assigned to all four components. A simple cohesive crack model with linear strain softening and Mazars' measure of

strain is used:

$$\sigma = (1 - \omega)E\varepsilon = f_t \left(1 - \frac{h\omega\varepsilon f_t}{2G_f} \right), \quad (3)$$

$$\tilde{\varepsilon} = \sqrt{\sum_{I=1}^3 \langle \varepsilon_I \rangle^2}, \quad (4)$$

where σ is the normal stress transferred across a cohesive crack, f_t is the uniaxial tensile strength, h is the effective width of a finite element, ε is the normal strain to a crack, G_f is the mode-I fracture energy, and ω is the damage parameter. $\langle \varepsilon_I \rangle$ are positive parts of the principal values of the strain tensor ε . Equation (3) leads to an explicit evaluation of damage parameter ω .

Table 3 summarizes the elastic and fracture properties of the four components. The elastic modulus of porosity was assigned a finite value, since this speeds up convergence. It was checked that a further reduction of the modulus leads to negligible changes in results. Clinker minerals are crystalline phases with high tensile strength and normally suffer no damage during loading. Their fracture energy is recalculated from scratch-test results [18].

The properties of CNT are estimated on the basis of recent results [16]. Hydration products, mainly C-S-H, are taken as the low-density type of C-S-H [1]. The C-S-H tensile strength and the C-S-H fracture energy were deduced from experimental data and a 2D simulation of plain paste. These two parameters were identified by means of an inverse-problem, taking the most reasonable case of the two weakly dependent parameters; flexural strength assuming 5.8 MPa, similar to [5, 8], and for fracture energy assuming 16.5 N/m as determined from our lab tests, see Figure 4.

Figure 5 depicts microstructure images for micromechanical simulations. As mentioned above, a composition of CEM 86% + CHM 14% was considered for all cases, with the exception of plain paste. The cross-section of one CNT truss element was 50 nm times 1 μm , which in fact represents a bundle of CNT, not a single nanotube. The CNT length was randomized according to uniform distribution and length limit. The orientation of the CNT fibers is also random. Gaussian distribution of CNT fibers in a cluster was

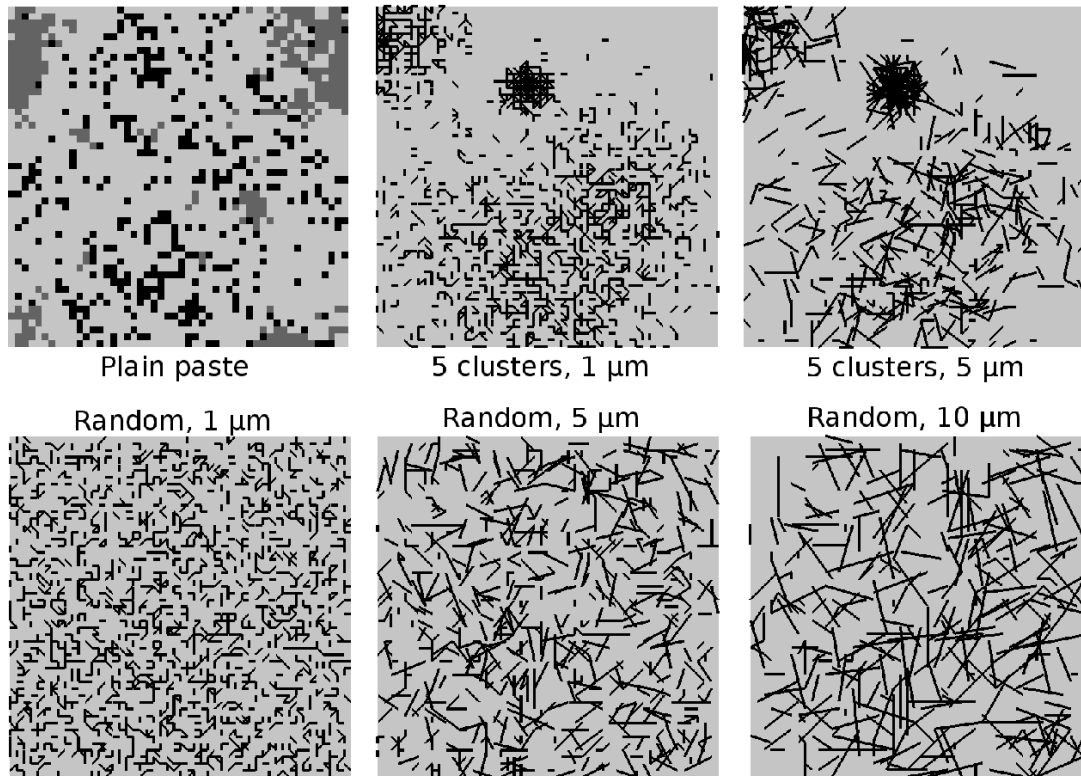


Figure 5: 2D microstructures used in the simulations. The plain paste contains three phases (black — porosity, dark gray — clinker minerals, light gray — hydration products). Other subfigures show CNT fibers distributed within plain paste, either in clusters or randomly.

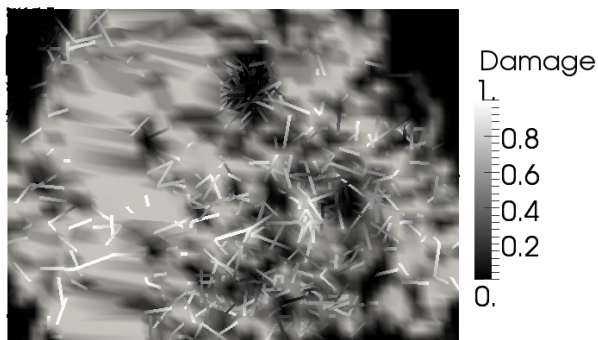


Figure 6: Deformed microstructure with 5 clusters and CNT length up to $5\ \mu\text{m}$ before the peak load.

used, and the cluster radius is uniformly distributed up to $10\ \mu\text{m}$.

The subfigures in Figure 5 show CNT fibers distributed in the paste. Each pixel was assigned to a quadrilateral element with four nodes, so the mesh is uniform and easily generated. Each simulation leads to 4900 unknown displacements, contains 150 displacement increments, uses the modified Newton-Raphson solver, and runs for approximately 5 minutes in the OOFEM package [14].

Figure 6 elucidates the damage distribution in the microstructure of 5 clusters with CNT length up to

CNT clusters	CNT length	f_t (MPa)	G_f (N/m)
Plain paste	Plain paste	5.8	16.5
5	$\leq 1\ \mu\text{m}$	5.9	15.5
5	$\leq 5\ \mu\text{m}$	6.3	25.9
0 (no clusters)	$\leq 1\ \mu\text{m}$	6.3	27.7
0 (no clusters)	$\leq 5\ \mu\text{m}$	7.1	43.8
0 (no clusters)	$\leq 10\ \mu\text{m}$	7.3	55.8

Table 4: Elastic and fracture properties of CNT-reinforced paste.

$5\ \mu\text{m}$ before the peak load. Note that there is no paste damage inside the heavily CNT-reinforced zones.

Table 4 summarizes the results from micromechanical simulations. It is evident that clustering of CNT is the most critical factor. Clustering leads to crack formation around strongly-reinforced zones, which renders the CNT reinforcement ineffective. The simulations show that the uniform distribution of $1\ \mu\text{m}$ CNT increases G_f from 16.5 to 27.7 N/m. Clustering leads to a smaller increase, even with CNT $5\ \mu\text{m}$ in length.

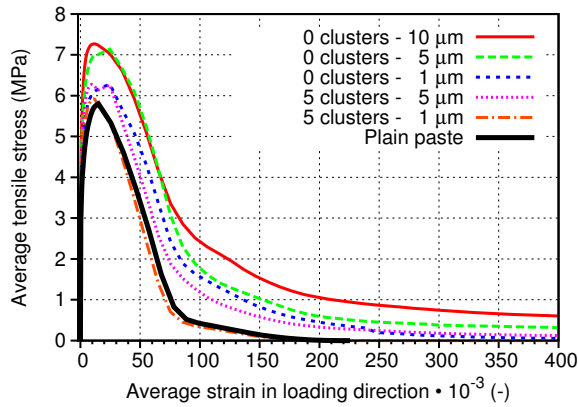


Figure 7: A stress-strain diagram for loaded microstructures.

Figure 7 plots the stress-strain diagram for plain and CNT-reinforced pastes. Note that there is not much increase in flexural strength but there is a significant improvement in ductility, which is reflected as an increase in fracture energy.

Addition of CNT to cement paste, in any form, leads necessarily to clustering. According to the Powers model of cement hydration, the CNT-unreinforced volume corresponds to the initial volume of unhydrated cement grains, where CNT cannot enter during initial mixing. The initial volume fraction of the clinker corresponds to

$$f_{\text{clinker}} = \frac{0.32}{w/c + 0.32}, \quad (5)$$

which for $w/c = 0.35$ yields 48%. This large volume remains unreinforced and prevents uniform distribution of CNT fibers. This explains why our experimental fracture energy is always lower than when micromechanical predictions with a uniform CNT distribution are used.

Further simulations with variable CHM content support the hypothesis that CNT clustering lowers the amount of fracture energy. Figure 8 shows that placing CNT only outside of originally unhydrated cement grains corresponds well with the experimental results. Cement paste with 30% CHM shows discrepancy with micromechanical simulation, the reason lies probably in lower workability and extensive CNT separation during mixing.

4 Conclusions

The role of CNT reinforcement in cement paste provides another option for improving the quasi-brittle behavior of cementitious materials. Experimental evidence shows a marginal improvement in compressive strength and fracture energy. As has been proven by numerical simulations, the clustering of CNT in

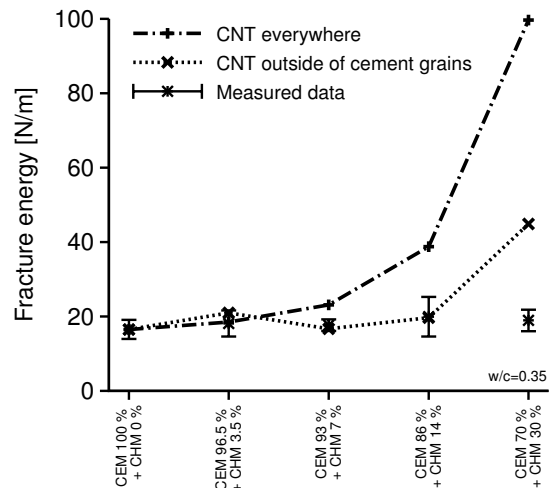


Figure 8: Fracture energy of pastes with variable CHM content (CNT length up to $3 \mu\text{m}$). Micromechanical simulations with average CNT length up to $2.5 \mu\text{m}$ consider CNT placement everywhere or only in areas outside of originally unhydrated cement grains.

the paste microstructure is the crucial factor, due to the presence of unreacted cement grains in the initial mixture and the intermixing of CHM with ordinary cement. However, micromechanical simulations show that a uniform distribution CNT fibers only $1 \mu\text{m}$ in length may increase the fracture energy from 16.5 to 27.7 N/m , and the flexural strength up to 10%.

Direct synthesis of CNT on the surface of cement particles solved the problem with flocculation of CNT separately added to the cement paste, but the problem of initially unhydrated grains remained. The claimed twofold increase in the compressive strength of cement paste with added CNT was not proven by our experiments [8]. Preliminary micromechanical simulations indicate that a real CNT reinforcement is ineffective when the tubes are shorter than an average cement grain. Hence, an effective CNT reinforcement needs to be at least approximately $15 \mu\text{m}$ CNT in length. The appropriate length of CNT reinforcement will be a topic for further research.

Acknowledgements

We gratefully acknowledge financial support from the Ministry of Education and Youth of the Czech Republic under CEZ MSM 6840770003, and from the Czech Science Foundation GAČR under projects P104/12/0102 and 103/09/H078.

References

- [1] G. Constantinides, F.-J. Ulm. The effect of two types of C-S-H on the elasticity of cement-based materials: Results from nanoindentation

- and micromechanical modeling. *Cem Concr Res* **34**(1):67–80, 2004.
- [2] A. Cwirzen, K. Habermehl-Cwirzen, V. Pentala. Surface decoration of carbon nanotubes and mechanical properties of cement/carbon nanotube composites. *Advances in cement research* **20**(2):65–74, 2008.
- [3] E. Hammel, X. Tang, M. Trampert, et al. Carbon nanofibers for composite applications. *Carbon* **42**(5-6):1153–1158, 2004.
- [4] Maria S. Konsta-Gdoutos, Zoi S. Metaxa, Surendra P. Shah. Multi-scale mechanical and fracture characteristics and early-age strain capacity of high performance carbon nanotube/cement nanocomposites. *Cement and Concrete Composites* **32**(2):110–115, 2010.
- [5] Geng Ying Li, Pei Ming Wang, Xiaohua Zhao. Mechanical behavior and microstructure of cement composites incorporating surface-treated multi-walled carbon nanotubes. *Carbon* **43**(6):1239–1245, 2005.
- [6] Victor C. Li, H. Horii, P. Kabele, et al. Repair and retrofit with engineered cementitious composites. *Engineering Fracture Mechanics* **65**(2–3):317–334, 2000.
- [7] Victor C. Li, Mohamed Maalej. Toughening in Cement Based Composites. Part I: Cement, Mortar, Concrete. *Cement and Concrete Composites* **18**(4):223–237, 1996.
- [8] Péter Ludvig, José M. Calixto, Luiz O. Ladeira, Ivan C. P. Gaspar. Using converter dust to produce low cost cementitious composites by in situ carbon nanotube and nanofiber synthesis. *Materials* **4**(3):575–584, 2011.
- [9] Z. S. Metaxa, M. S. Konsta-Gdoutos, S. P. Shah. Mechanical Properties and Nanostructure of Cement Based Materials Reinforced with Carbon Nanofibers and PVA Microfibers. *ACI Special Publication 270: Advances in the Material Science of Concrete SP-270-10* **270**:115–124, 2010.
- [10] P. Morgan. *Carbon fibers and their properties*. CRC Press, 2005. 794–796.
- [11] Prasantha R. Mudimela, Larisa I. Nasibulina, Albert G. Nasibulin, et al. Synthesis of carbon nanotubes and nanofibers on silica and cement matrix materials. *Journal of Nanomaterials*, 2009.
- [12] Albert G. Nasibulin, Sergey D. Shandakov, Larisa I. Nasibulina, et al. A novel cement-based hybrid material. *New Journal of Physics* **11**(2):023013, 2009.
- [13] Larisa I. Nasibulina, Ilya V. Anoshkin, Sergey D. Shandakov, et al. Direct synthesis of carbon nanofibers on cement particles. *Transportation Research Record: Journal of the Transportation Research Board* **2**(2142):96–101, 2010.
- [14] B. Patzák, Z. Bittnar. Design of Object Oriented Finite Element Code. *Advances in Engineering Software* **32**(10–11):759–767, 2001.
- [15] Florence Sanchez, Chantal Ince. Microstructure and macroscopic properties of hybrid carbon nanofiber/silica fume cement composites. *Composites Science and Technology* **69**(7–8):1310–1318, 2009.
- [16] V. Šmilauer, C. G. Hoover, Z. P. Bažant, et al. Multiscale Simulation of Fracture of Braided Composites via Repetitive Unit Cells. *Engineering Fracture Mechanics* **78**(6):901–918, 2011.
- [17] RILEM TC50-FMC. Determination of the fracture energy of mortar and concrete by means of three-point bend tests on notched beams. *Materials and Structures* **18**(4):285–290, 1985.
- [18] F.-J. Ulm, R. Pellenqs. Bottom-up materials science. In *MIT-France Energy Forum*. 2011.
- [19] B. I. Yakobson, C. J. Brabec, J. Bernholc. Nanomechanics of carbon tubes: Instabilities beyond linear response. *J Phys Rev Lett* **76**(14):2511–2515, 1996.

Part V

Paper 4

Authors: František Škvára, Vít Šmilauer, Petr Hlaváček, Lubomír Kopecký,
Zuzana Cílová

Title: A weak alkali bond in (N, K)-A-S-H gels: Evidence from leaching
and modeling

Journal: Ceramics-Silikáty

Number: 4

Volume: 56

Year: 2012

A WEAK ALKALI BOND IN (N, K)–A–S–H GELS: EVIDENCE FROM LEACHING AND MODELING

FRANTIŠEK ŠKVÁRA, #VÍT ŠMILAUER*, PETR HLAVÁČEK*, LUBOMÍR KOPECKÝ*, ZUZANA CÍLOVÁ

ICT Prague, Faculty of Chemical Engineering, Department of Glass and Ceramics,
Technická 5, 16628 Prague 6, Czech Republic

*Czech Technical University in Prague, Faculty of Civil Engineering, Department of Mechanics,
Thákurova 7, 16629 Prague 6, Czech Republic

#E-mail: vit.smilauer@fsv.cvut.cz

Submitted August 29, 2012; accepted November 9, 2012

Keywords: Aluminosilicate gel, N–A–S–H gel, Geopolymer, Leaching, Efflorescence

The alkali bond in (N, K)–A–S–H gels presents an up-to-date insufficiently resolved issue with significant consequences for efflorescence in alkali-activated materials. A series of experiments shows nearly all alkalis are leachable from alkali-activated fly-ash and metakaolin in excessive amounts of deionized water. A diffusion-based model describes well the alkali leaching process. Negligible changes of the (N, K)–A–S–H gel nanostructure indicate that Na, K do not form the gel backbone and H_3O^+ is probably the easiest substitution for the leached alkalis. Small changes in the long-term compressive strength of leached specimens support this hypothesis.

INTRODUCTION

The increasing demand for a low-cost and durable construction material stimulates further research in alternative cementitious binders [1 - 5]. Alkali-activated binders based on fly ash or slag represent such a promising group which has stimulated intensive interest worldwide.

The alkali-activation reaction is known from Portland-based materials in which calcium hydroxide promotes the hydrolysis and dissolution of the Si–O group of blended aluminosilicate materials. In contrast to this slow pozzolanic reaction, alkali-activated binders require a much stronger base environment, such as sodium or potassium hydroxides, often exceeding 8M. A detailed analysis of 25 compositions available in open literature revealed that alkali-activated fly ash is normally activated with Na_2O concentrations in the range of 29–237 g/kg of paste with the median 76.6 g/kg, see Fig. 1. These compositions had to meet reasonable workability and the majority of samples experienced curing above 50°C.

Historically, an alkali-activated binder has been called a geopolymer, inorganic polymer, chemically bonded ceramic or alkali-activated cement. Subtle differences originating rather from the commercial background have generated confusion and ill-coordinated research. Furthermore, many of these terms have broadened their meanings over time and started to describe Ca-rich materials as well. For these reasons, the term (N, K)–A–S–H gel is adopted here, describing the

chemical nature of the reaction product rather than its precursor, similar in terminology with C–S–H.

The nanostructure of a poorly crystallized (N, K)–A–S–H gel remains fully unresolved and is still far from being understood. Extensive characterization via NMR, XRD led to the conclusion that the (N, K)–A–S–H gel constitutes a Si–O–Al coordinated 3D network with water filled nanoporosity. Analogous models based on C–S–H or zeolites helped to understand its basic features. Nanoindentation demonstrated intrinsic indentation modulus of the N–A–S–H gel between 17 and 18 GPa on the submicrometers scale, regardless of activated material and curing conditions [6].

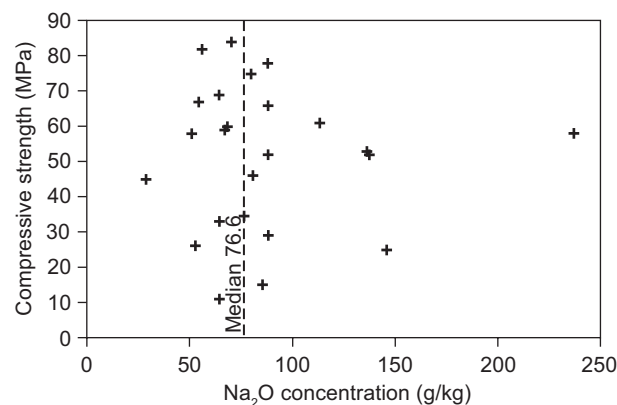


Figure 1. Literature review on Na_2O concentrations in alkali-activated fly-ash from 22 resources (mainly world journals with an impact factor). The SiO_2/Na_2O mass ratio differs in the range between 0 and 1.45.

However, further modeling deduced that basic building blocks of the N–A–S–H gels are different, depending on activating solutions [7].

The role of alkalis in the (N, K)–A–S–H gel seems to draw little attention. Several experiments testified efflorescence problems pointing out to the excessive and weakly bound Na in the gel network [5, 8]. It raises the question whether alkalis are essential elements in the gel nanostructure or they are remnants from the activating solution. This article aims at comparing N, K-leached and unleached (N, K)–A–S–H gels to prove that alkalis can be leached out without affecting the gel skeletal structure, without a loss in strength. This contrasts with C–S–H where calcium leaching leads to a collapse.

Existing models for Na(K) bonds
within (N,K)–A–S–H gels

Glukhovskiy [9] and Krivenko [10, 11] built up models based on the zeolite analogy, primarily related to analcime. They assume the (N, K)–A–S–H gel is amorphous, with randomly distributed little clusters of reciprocal structures, so called short-range-order of SiO₄ tetrahedra and AlO₄ octahedra. A strong Na ionic bond exists within the analcime structure; Na-cations are seated in the centers of the cages of the analcime network. Water molecules fully occupy 16 sites in the unit cell. It is known that Na leaching from zeolites occurs with difficulties, under specific hydrothermal conditions [12], leading to the collapse of zeolite. The model offers no explanation on the weak Na bond and why there is no collapse after the full leaching.

Davidovits [13, 14] formulated a geopolymer model based on the polymeric Si–O–Al network; poly(sialate), poly(sialate-siloxo) and poly(sialate-disiloxo) repetitive units. He described stages in the gel formation, starting with dissolution in a strongly alkaline environment, formation of silanol groups and polycondensation. The weak negative charge on Al^{IV} in the tetrahedral coordination is balanced by Na⁺(K⁺) cations in a strong

ionic binding. Further polycondensation continues into the Na-poly(sialate-disiloxo) albite framework with a feldspar chain structure. The feldspar (albite) crystalline lattice framework is fully reciprocal. Na, (K, Ca) cations are bonded to oxygen in SiO₄ and AlO₄ tetrahedra, but not to alumina, in order to overbalance the excessive negative charge. The leaching of Na (K) alkalis from the feldspar-like structure, without the collapse of the aluminosilicate network of newly formed gel, is in reciprocal contradiction. The leaching of alkalis from the feldspar structure, e.g. during weathering, results in the total collapse of feldspar spatial framework and formation of the sheet silicates and clay minerals.

Fernández-Jiménez et al. [15] presented a model inspired by the sol-gel process. The colloids themselves form cross-links leading to 3-D structures. The Al₂O₃/K₂O ratio equals one since certain other ions must be included in the structure to offset the electrical imbalance generated when Al³⁺ ions replace Si³⁺ ions in the polymer. The Al in these gels is tetrahedrally coordinated.

Cloos et al. [16] assume that silico-alumina gels are based on Si^{IV}, occurring in a tetrahedral coordination with a partial substitution of Al^{IV} (Al³⁺). The negative charge in the core is compensated by the positive charge of mono- or polymeric hydroxyaluminium cations Al(OH)₂⁺. Increasing the Al/(Al+Si) ratio, the complexity of these polymeric cations increases, whilst the net charge per alumina atom decreases. At very high Al/(Al+Si) ratios (> 0.8), this charge tends to zero and a demixing is observed and the next phases (pseudo-boehmite and bayerite) appear.

Mason et al. [17] assume that the existence of Al^{IV} in association with Si^{IV} requires an additional charge and structural balancing components in the form of Na⁺ (K⁺) cations. The spectra of 9.4 T ²³Na NMR reveal that the positions of the peaks are similar to those observed for sorbed Na⁺ on the surface of silica. The hydration state suggests the Al^{IV} phase is kaolinite-like, and the ²⁹Si data indicates that at least in one case allophane is present.

Barbosa et al. [18] consider the gel as randomly

Table 1. Basic models N(K)–A–S–H gels and Na(K) bond.

Authors	Analogy	Na(K) bond within N(K)–A–S–H gels
Glukhovskiy [9], Krivenko [10,11]	Zeolites, analcime	Alkali cations are linked with a strong ionic bond within the Si–O–Al network and remain hardly leachable.
Davidovits [13,14]	Organic polymer	Na ⁺ (K ⁺) compensate a weak negative charge on Al ^{IV} . Further polycondensation into the Na-poly(sialate-disiloxo) albite framework with a feldspar chain structure.
Fernández-Jiménez et al. [15]	Synthetic gel, colloid	Na ⁺ (K ⁺) compensate a weak negative charge on Al ^{IV} .
Cloos et al. [16]	Synthetic gel, colloid	Al(OH) ₂ ⁺ or Al _n (OH) _m ^{(3n-m)+} compensate a charge of Al ^{IV} in the tetrahedral coordination. The Na ⁺ bond remains unaddressed.
Mason et al. [17]	Synthetic gel	Na ⁺ (K ⁺) compensate a weak negative charge on Al ^{IV} .
Barbosa et al. [18]	Organic polymer	Na(H ₂ O) _n ⁺ , K(H ₂ O) _n ⁺ compensate a weak negative charge on Al ^{IV} .

oriented Al, Si polymeric chains providing cavities of sufficient size to accommodate the charge-balancing hydrated Na ions in the form of $\text{Na}(\text{H}_2\text{O})_n^+$, $\text{K}(\text{H}_2\text{O})_n^+$. The model allows easy cation leaching while keeping a positive-negative charge balance.

EXPERIMENTAL

Materials and methods

Fly ash of class F originated from the Opatovice brown-coal power plant, Czech Republic. Metakaolin from the Sedlec location, Czech Republic, was prepared from ordinary kaolin treated at 750°C for 24 hours. Table 2 provides chemical compositions of both materials.

Table 3 provides initial compositions for Na, K alkali-activated fly ash and metakaolin which are denoted further as AAFA and AAMK. The compositions were optimized to meet standard workability and possess compressive strength above 40 MPa. Sodium and potassium metasilicate solutions were intermixed with NaOH or KOH and water added. All samples were cured at 80°C for 12 hours and stored in a 20–25°C environment under RH 45–50 %, if not specified differently.

Experimental methods included XRD (PANalytical X'Pert PRO Philips), FTIR (Nicolet 740 Nexus), NMR MAS (^{29}Si , ^{27}Al , ^{23}Na , BrukerAvance 500WB/US), EDX+ EBSD (XL 30 ESEM), AAS (Varian Spectr AA880). More detailed study was devoted to raw fly ash

using electron microscopy (Hitachi S-4700 coupled with the SDD detector) with analyzer XRF (ARL 9400/HP+). Particular details of leaching conditions and specimens' geometries are provided in the following subsections.

RESULTS AND DISCUSSION

Before proceeding to leaching experiments, alkali leachability from inactivated materials had to be assessed. Raw fly ash contains certain amounts of Na, K, see Table 2. Immersing 20 g of raw FA into 1000 g of deionized water and constant shaking for 72 hours revealed that only 1.7 % of Na_2O and 0.8 % of K_2O had leached out. For this reason, the alkalis present in FA and MK were neglected in the assessment of the overall leaching balance.

Remaining Na, K in (N, K)–A–S–H gels after long-term leaching

A sufficiently long Na, K leaching from AAFA and AAMK reveals an asymptotic concentration of alkalis in (N, K)–A–S–H gels. To speed up the leaching process, paste samples were crushed under the size of 0.5 mm and leached 150 days in deionized water with regular water exchange between 1 and 3 days. The content of Na, K was determined using X-ray fluorescence analysis. Table 4 shows the initial and final concentrations of Na_2O and K_2O in the geopolymer paste; only 2 % of Na_2O and

Table 2. Chemical compositions of fly ash and metakaolin.

Oxide (wt. %)	SiO_2	Al_2O_3	Na_2O	K_2O	CaO	MgO	Fe_2O_3	TiO_2
Fly ash	53.52	32.87	0.33	2.05	1.80	0.85	5.89	1.89
Metakaolin	50.43	46.20	0.03	1.07	0.38	0.27	1.07	0.27

Table 3. Initial compositions of pastes and mortars in terms of mass ratios.

	$\text{SiO}_2/(\text{Na,K})_2\text{O}$	$\text{H}_2\text{O}/(\text{Na,K})_2\text{O}$	Activator/(FA, MK)	Fly ash/sand	Initial $(\text{Na,K})_2\text{O}/\text{all}$ [g/kg]
Paste, fly ash, Na	1.06	4.57	0.46	–	47.81
Paste, fly ash, K	1	3.14	0.36	–	51.47
Paste, metakaolin, Na	1	3.5	1.1	–	95.24
Paste, metakaolin, K	1	3.5	1.1	–	95.24
Mortar, fly ash, Na	1.06	4.28	0.44	1:1.5	23.78
Mortar, fly ash, K	1	3.85	0.41	1:1.5	24.05

Table 4. Concentration of M_2O in the geopolymer before and after leaching for 150 days.

	Initial concentration $\text{M}_2\text{O}/\text{initial mass}$ [g/kg]	Final concentration after 150 days of leaching $\text{M}_2\text{O}/\text{initial mass}$ [g/kg]	Molar concentration M^+/Al^- in N–A–S–H gel before leaching [mol/mol]	Molar concentration M^+/Al^- in N–A–S–H after leaching [mol/mol]
AAFA, Na	47.81	0.96	0.7	0.01
AAFA, K	51.47	0.77	0.46	0.01
AAMK, Na	95.24	5.71	0.72	0.04
AAMK, K	95.24	1.9	0.47	0.01

1.5 % of K_2O remained in AAFA and 6 % of Na_2O and 2 % of K_2O in AAMK. This shows that Na, K are weakly bound in the (N, K)-A-S-H gel and could be almost completely leached out.

The theoretical molar ratio M^+/Al^- is calculated from the amount of dissolved Al from fly ash or metakaolin which combined to the (N, K)-A-S-H gel. The Al leaching from hardened AAFA after 18 days was found to be only 0.1 % of the overall Al amount, therefore leached Al can be neglected. The degree of reaction for AAFA was previously estimated as 0.5 and for AAMK as 0.99 [6]. Table 4 provides molar ratio M^+/Al^- before and after leaching. Considering the charge-balancing interaction between (Na^+, K^+) and Al^- , the leached alkali cations need to be replaced. We hypothesize H_3O^+ presents the most suitable replicant.

Leaching kinetics of Na_2O from N-A-S-H gels and modeling

The previous section proved almost full leaching of Na, K from the AAFA and AAMK pastes. The following experiment quantifies the Na leaching kinetics from AAFA. A sodium-activated AAFA specimen with the size of $40 \times 40 \times 160$ mm was submerged into 600 ml of deionized water, where the water had regular replacement between one and three days. The concentration of Na in the water bath was measured after each water replacement.

Table 5 summarizes the measured concentrations of Na_2O during 18 days. The remaining Na_2O in the paste was deduced from the leached Na and the initial concentration, see Table 3.

The unknown diffusion coefficient for the Na transport was determined using the 3D leaching simulation in the OOFEM software [18]. One eighth of the $40 \times 40 \times 160$ mm sample was considered due to symmetry reasons, see Figure 2 for the geometry. The numerical

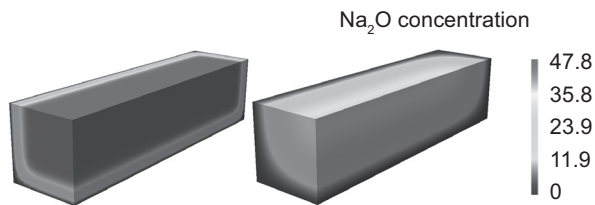


Figure 2. Na leaching simulation on an eighth of the $40 \text{ mm} \times 40 \text{ mm} \times 160 \text{ mm}$ prism. Concentrations of Na_2O (g/kg) in the AAFA paste after 28 days of leaching (left) and after 365 days of leaching (right).

simulation assumes the diffusion coefficient to be constant and independent of the concentration. It is well known that the water vapor diffusivity coefficient drops by a factor of approximately 20 for mature concrete [20]. Nonlinear diffusion would cause a slowdown in the leaching process. However, the asymptotic values are retained. Figure 3 shows the average concentration of Na_2O in the paste during the leaching experiment and the results from the numerical simulation. The diffusion coefficient for the Na transport in the AAFA was fitted to $D = 1.6 \cdot 10^{-7} \text{ m}^2/\text{day}$. Figure 2 depicts the concentration field at 28 days and 365 days of leaching.

Na_2O profile from EDX analysis

The Na_2O concentration profile from the sample surface could be verified independently by EDX analysis. Surface areas were cut from the 28 day-leached AAFA and AAMK prisms and exposed to an EDX line analysis. Figure 4 shows the Na_2O concentration profile with strongly heterogeneous values. Analytical solution of a linear diffusion equation leads to the error function [20]

$$c(x, t) = c_{init} \operatorname{erf}\left(\frac{x}{2\sqrt{Dt}}\right) \quad (1)$$

where c_{init} is the initial concentration of Na_2O in the body, $c(x, t)$ is the concentration at a given time and the position x from the surface, D represents the constant diffusion coefficient and the time t represents 28 days.

Figure 4 displays analytical solution for AAFA and AAMK with measured data. The upper and lower feasible bounds are displayed with corresponding diffusion coefficients. Due to higher porosity of AAMK, the diffusion coefficient attains a higher value. Note that the

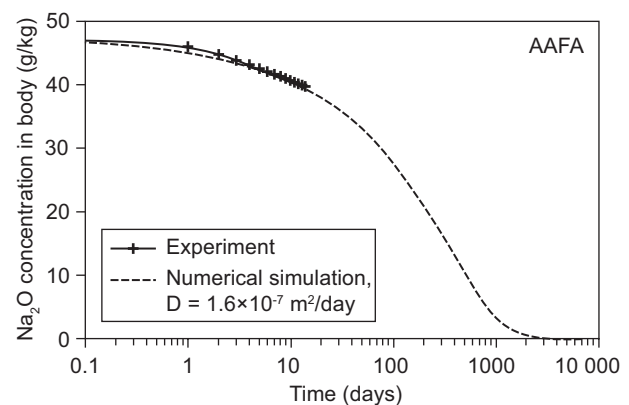


Figure 3. Concentrations of Na_2O in the AAFA paste. The prism $40 \times 40 \times 160$ mm was leached in deionized water which was regularly replaced.

Table 5. Concentration of Na_2O in the water bath during the leaching experiment.

Time [day]	1	2	3	4	7	8	9	10	11	14	15	16	17	18
Conc. [g/l]	3.96	2.66	2.02	1.53	2.95	1.12	0.86	0.78	0.72	1.33	0.61	0.52	0.48	0.43

measured concentration profiles reach non-zero values on the surface since certain transport occurs during the preparation for EDX analysis.

Visible evidence for efflorescence

Exposing Na-activated materials to a moisture-gradient environment leads to the formation of efflorescence [5], Figure 5. The leaching of Na from the bulk activated material reacts with atmospheric CO₂ and forms visible carbonates, hydrocarbonates and sulfates. The analysis of efflorescence products revealed no crystalline silicates.

Alkali transport could be mitigated when samples are exposed to RH < 30 %. Such low humidity seems to be sufficient for breaking-up continuous pore channels for ion transport. Any rewetting of a sample surface reactivates the transport mechanisms and efflorescence

reappears after a short time.

Exposing wet polished samples to a low vacuum environment leads to a quick formation of efflorescence. Figure 6 shows the beginning stage of surface efflorescence on AAFA.

SEM of leached samples and compressive strength

No visible changes on fracture surfaces were observed in leached AAFA specimens for 3 years, Figure 7. The samples were immersed in a sealed container with deionized water which was exchanged every week. No observable differences are evident for AAMK leached for 3 months, Figure 8.

No degradation of N–A–S–H gels after leaching

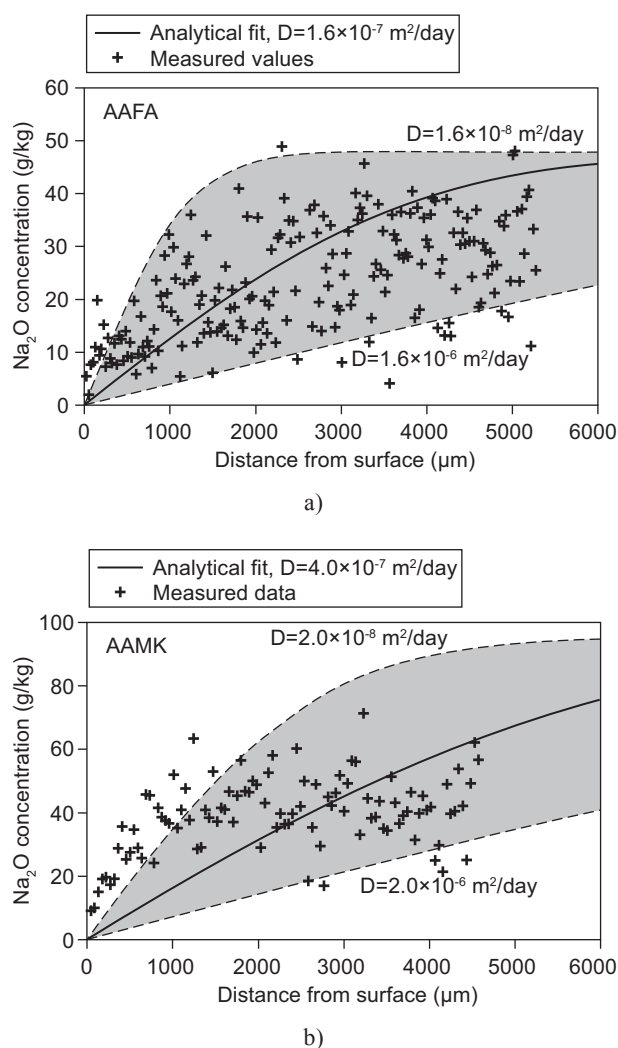


Figure 4. The Na₂O concentration profile in AAFA (a) and AAMK (b) after 28 days of leaching in deionized water. Measured points in black were gathered using the EDX linear analysis. Black lines show solution via error function with feasible lower and upper bounds.

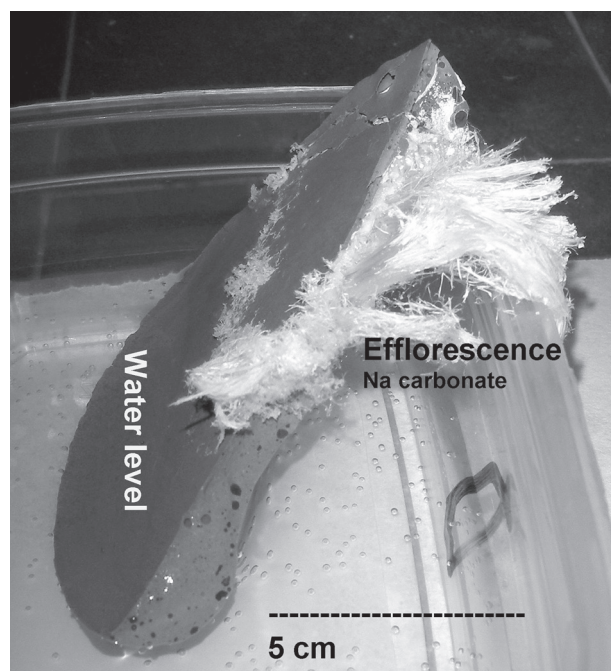


Figure 5. High efflorescence after 50 days of partially-immersed AAFA.

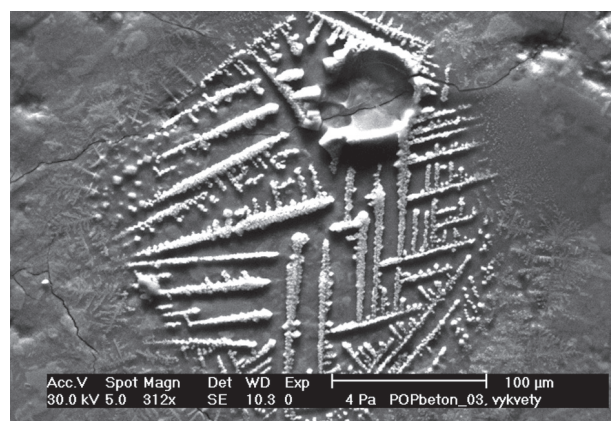


Figure 6. Efflorescence on the surface of AAFA (Na₂CO₃, NaHCO₃) in ESEM.

is supported via compressive strength measurement on AAFA mortars, Figure 9. The specimens (4×4×16 cm) were left for 550 days on air or immersed in water. Different strengths within air and water-cured samples could be partially attributed to the fact that dry concrete exhibits higher strength due to higher cohesion forces between the gel particles.

When a strength decrease is associated with the process of Na leaching, gradual strength degradation would occur, which is not the case here. Similar findings were observed on samples immersed up to two years in water [21-24]. This indicates only the Si-O-Al-O-Si chain forms a load-bearing nanostructure within the N-A-S-H gel and Na is bound weakly, practically unaffacting compressive strength.

This strongly contrasts with C-S-H-based materials, where calcium leaching of Portland pastes in the ammonium nitrate solution proved a significant reduction in compressive strength to about one fourth of sound samples [25, 26]. The nanoindentation experiment

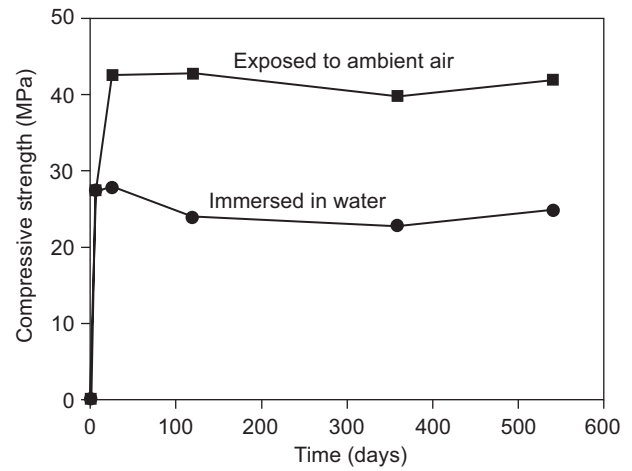
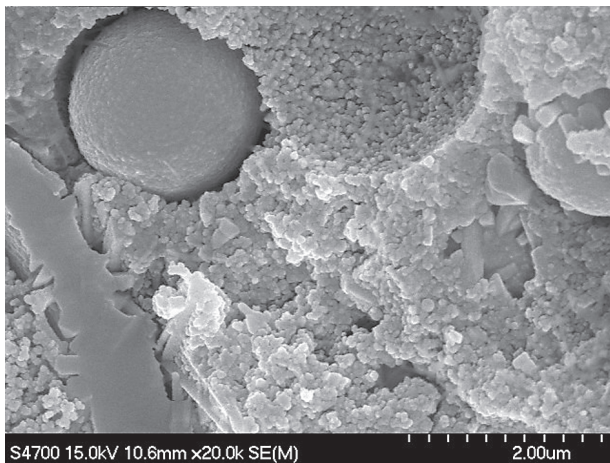
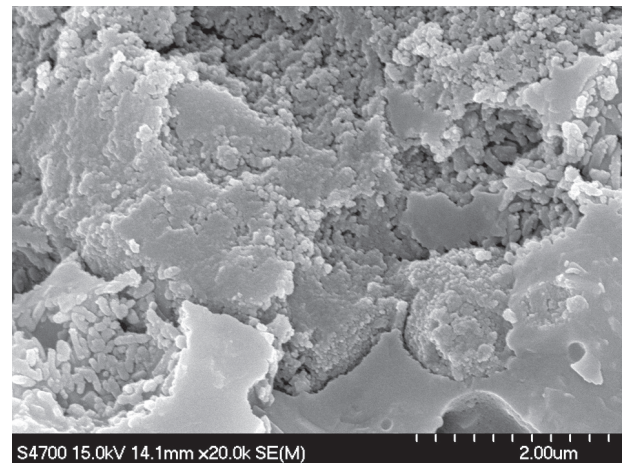


Figure 9. Compressive strength evolution of AAFA mortars. The samples were exposed to ambient air or immersed in water at 20-25°C.



a)



b)

Figure 7. AAFA samples unleached (left) and leached for 3 years (right), fracture surface in SEM.



a)



b)

Figure 8. AAMK samples unleached (left) and leached for 3 months (right), fracture surface in SEM.

testified that the elastic modulus of low-density type C–S–H dropped from 21.7 to 3.0 and that of C–S–H high-density type dropped from 29.4 to 12 GPa [27]. These findings clearly demonstrate Ca being a significant part of the C–S–H gel while Na being abundant in the N–A–S–H gel.

^{29}Si , ^{27}Al NMR MAS spectra of Na-activated AAFA and AAMK

The ^{29}Si and ^{27}Al NMR spectra of leached and unleached AAFA samples are essentially the same, without any noticeable changes exceeding the NMR inaccuracies. Leached samples were 150 days in deionized water with regular water exchange between 1 and 3 days.

The ^{29}Si spectra for AAMK show a small difference which is probably attributed to the peak at -109.3 ppm, previously ascribed to crystalline silica phases [3]. Both AAFA and AAMK indicate that the Si–O–Al backbone remains essentially the same before and after Na leaching.

Mitigation of Na leaching and ^{23}Na MAS NMR

Na leaching drops to almost zero when AAFA samples are exposed to temperatures over about 600°C for 2 hours. Figure 12 demonstrates the Na_2O concentration in the water bath (1:50 by mass) after the 24 hour exposure of prismatic samples 40×40×160 mm. The change indicates that Na enters directly into the structure of the N–A–S–H gel and becomes an integral part of the newly formed sodium silicate glass as demonstrated in the following ^{23}Na NMR MAS spectra.

The ^{23}Na NMR MAS spectra in Figure 13 show that at 20°C Na occurs in the structure in the form of $\text{Na}(\text{H}_2\text{O})_n^+$ where $n = 2-8$ [28]. The peak at -4 ppm is attributed to the sodium associated with Al inside the gel nanostructure [3]. The shift to negative values above 400°C is attributed to water evaporation. A further series of peaks in the spectrum at 400–600°C corresponds to the overall rearrangement of the N–A–S–H gel structure. A dominant peak at -14ppm occurs at 600°C, which corresponds to the structure of sodium silicate glass

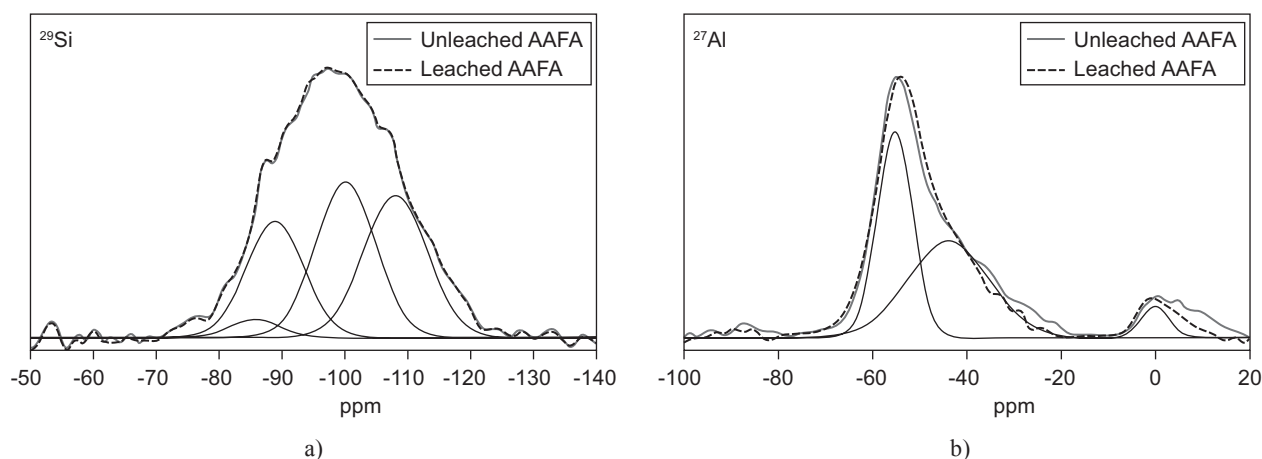


Figure 10. ^{29}Si and ^{27}Al NMR MAS spectra for AAFA. Deconvolution spectra plotted for unleached samples.

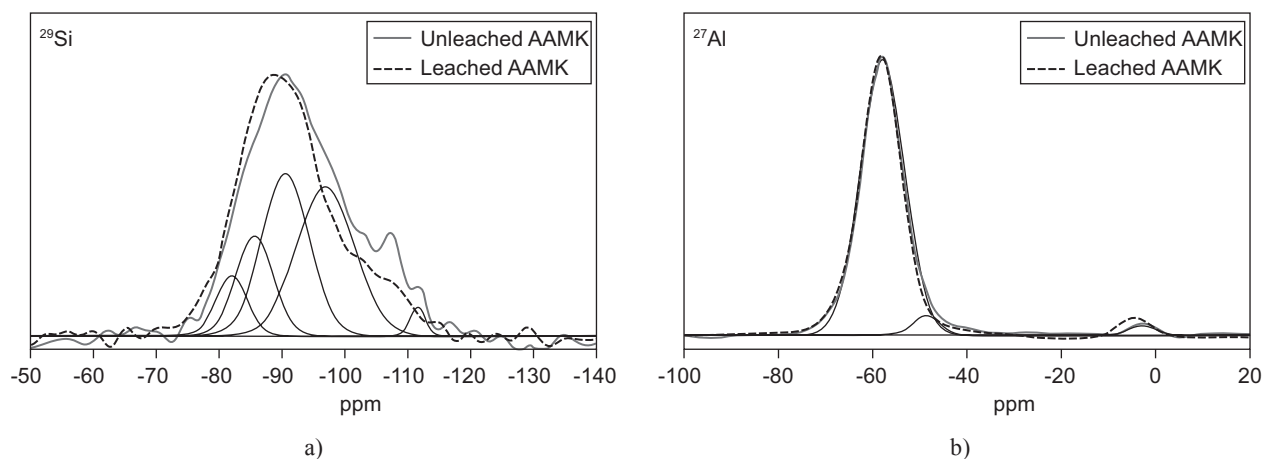


Figure 11. ^{29}Si and ^{27}Al NMR MAS spectra for AAMK. Deconvolution spectra plotted for unleached samples.

[29, 30]. The ^{39}K NMR spectrum demonstrated a similar effect [30]. Therefore, Na acts as a melting agent above 600°C and becomes embedded within sodium silicate glass.

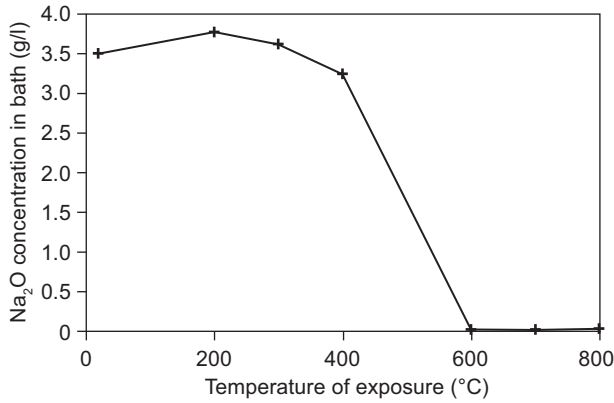


Figure 12. Na leachability from the AAFA paste in dependence on the previous temperature history.

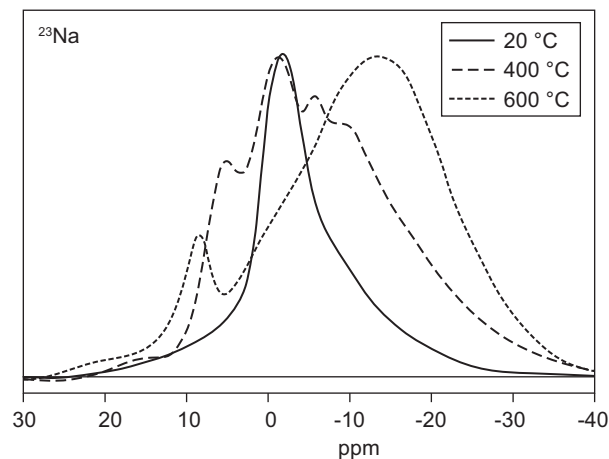


Figure 13. ^{23}Na NMR MAS spectra of AAFA in dependence on the thermal history.

Refined model for the alkali bond within (N,K)-A-S-H gels

A weak Na, K bond in (N, K)-A-S-H gels could be interpreted using the model from Barbosa et al. [18]. The positively-charged alkali cation can be replaced with other cations present in the system, see Figure 14. The most probable is H_3O^+ but $\text{Al}(\text{OH})_2^+$ or $\text{Al}_n(\text{OH})_m^{(3n-m)+}$ could also compensate the negative charge according to Cloos et al. [16]. The presence of other metal cations (Fe, Mn, Ca, K) in the geopolymer precursor (metakaolin, fly ash) can also easily balance the negative charge on Al^{IV} . The refinement for the alkali bond presents a minor adjustment in the 3D model of the Si-O-Al-O-Si network.

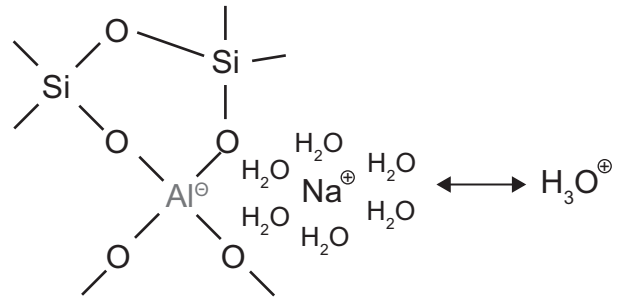


Figure 14. An alkali bond according to Barbosa et al. [18] and its replacement with an H_3O^+ cation during leaching.

CONCLUSIONS

The series of experiments demonstrated a weak bond of Na(K) in the (N, K)-A-S-H gel. The analyses of the Na, K role in alkali activated fly ash and metakaolin-based systems lead to the following conclusions:

1. Na, K create a strong base environment for the dissolution of glass phases from activated materials in accordance with up-to-date knowledge. Na, K is bound only weakly in the nanostructure of the (N,K)-A-S-H gel and is leachable almost completely. This causes alkali-activated materials to be prone to efflorescence with excessive remnants of alkalis in the system. (Na,K)OH easily diffuses to the surface where it reacts with atmospheric CO_2 while forming visible salts such as $\text{Na}_2\text{CO}_3 \cdot n\text{H}_2\text{O}$, NaHCO_3 , K_2CO_3 , KHCO_3 .
2. Almost all Na can be leached out from the gel without compromising compressive strength. This renders Na as an unnecessary load-bearing element in the nanostructure of the N-A-S-H gel and demonstrates A-S-H to be a load-bearing structure. In such particular case, the Al negative charge must be balanced by another cation, probably by readily available H_3O^+ .
3. The diffusivity for Na leaching was found between $1.6 \cdot 10^{-7}$ and $4.0 \cdot 10^{-7} \text{ m}^2/\text{day}$. Similar values are expected for K.
4. Exposing Na-activated fly ash to temperatures over 600°C practically stops Na leaching. This is explained by Na embedding inside the newly formed glasses.

Acknowledgement

We gratefully acknowledge the financial support from the Czech Science Foundation GAČR under projects P104/12/0102 and P104/10/2344.

References

1. Gartner E.M., Macphee D.E.: *Cem. Concr. Res.* 47, 736 (2011).
2. Pacheco-Torgal F., Castro-Gomes J., Jalali S.: *Constr. and Build. Mater.* 22, 1305 (2008).
3. Provis J.L., van Deventer J.S.J. et al.: *Geopolymers, structure, processing, properties and industrial applications*, CRC Press 2009.
4. Škvára F., Kopecký L., Šmilauer V., Bittnar Z.: *J. Hazard. Mater.* 168, 711 (2009).
5. Škvára F., Kopecký L., Myšková L., Šmilauer V., Albebovská L., Vinšová L.: *Ceramics-Silikáty* 53, 276 (2009).
6. Němeček J., Šmilauer V., Kopecký L.: *Cem. Concr. Comp.* 33, 163 (2011).
7. Šmilauer V., Hlaváček P., Škvára F., Šulc R., Kopecký L., Němeček J.: *J. Mater.Sci.* 46, 6545 (2011).
8. Ly L., Vance E.R., Perera D.S., Aly Z., Olufson K.: *Adv. in Tech. of Mat. and Mat. Proc. J.* 8, 239 (2006).
9. Glukhovskiy, V.D.: *Soil Silicates* (Gruntosilikaty), Budivelnik Publish, Kiev, Ukraine 1967.
10. Krivenko P.: *Adv. in Sci. and Tech.* 69, 1 (2010).
11. Krivenko P., Kovalchuk G.: *J. Mater. Sci.* 42, 2944 (2007).
12. Klika Z., Weiss Z., Mellini M.: *Acta Geodynamica et Geomaterialia* 2, 1 (2005).
13. Davidovits J. in: *Proc. 2nd Inter. Conf. Géopolymère 1999*, p. 9-40, Ed. J. and R. Davidovits, C. James, Institut Géopolymère 1999.
14. Davidovits J.: *Geopolymers Chemistry and Applications*, 2nd ed. Institut Géopolymère 2008.
15. Fernández-Jiménez A., Vallepu R., Terai T., Palomo A., Ikeda K., *J. Non-Cryst. Solids* 352, 2061 (2006).
16. Cloos P., Léonard A.J., Moreau J.P., Herbillon A., Fripiat J.J.: *Clays Clay Miner.* 17, 279 (1969).
17. Mason H.E., Maxwell R.S., Carroll S.A.: *Geochim. Cosmochim. Acta* 75, 6080 (2011).
18. Patzák B., Bittnar Z.: *Advances in Eng. Soft.*, 32, 759 (2001).
19. Barbosa V.F.F., Mac Kenzie K.J.D., Thaumaturgo C.: *Intern. J. Inorg. Mater.* 2, 309 (2000).
20. Vedalakshmi R., Saraswathy V., Song H.W., Palaniswamy N.: *Corros. Sci.* 51, 1299 (2009).
21. Hardjito D., Rangan B.V.: *Research Report GC 1*, Curtin University of Technology, Perth, Australia 2005.
22. Hardjito D., Wallah S.E., Sumajouw D.M.J., Rangan B.V.: *ACI Mater. J.* 101, 67 (2004).
23. Wallah S.E., Hardjito D., Sumajouw D.M.J., Rangan B.V. in: *Proc. ICFRC Inter. Conf.*, p. 527 – 539, Ed. Parameswaran V.S., Pub. Allied Publishers Private Limited, New Delhi 2004.
24. Strnad T., PhD Thesis, Czech Technical University in Prague, 2010.
25. Kamali S., Moranville M., Leclercq S.: *Cem. Concr. Res.* 38, 575 (2008).
26. Carde C., Raul F.: *Cem. Concr. Res.* 27, 539 (1997).
27. Constantinides G., Ulm F.J.: *Cem. Concr. Res.* 34, 67 (2004).
28. Maekawa H., Saito T., Yokokawa T.: *J. Phys. Chem. B* 102, 7523 (1998).
29. Tossell J.A., *Phys. Chem. Minerals* 27, 70 (1999).
30. Phair J.W., van Deventer J.S.J.: *Minerals Eng.* 14, 289 (2001).

Part VI

Paper 5

Authors: Petr Hlaváček, Vít Šmilauer, František Škvára, Lubomír Kopecký,
Rostislav Šulc

Title: Inorganic foams made from alkali-activated fly ash: mechanical,
chemical and physical properties

Journal: Journal of the European Ceramics Society

Year: 2014, *in Press*

Inorganic foams made from alkali-activated fly ash: mechanical, chemical and physical properties

P. Hlaváček^{a,*}, V. Šmilauer^{a,*}, F. Škvára^b, L. Kopecký^a, R. Šulc^a

^a*Czech Technical University in Prague, Faculty of Civil Engineering, Thákurova 7,
166 29 Prague 6, Czech Republic*

^b*Institute of Chemical Technology in Prague, Faculty of Chemical Engineering,
Department of Glass and Ceramics, Technická 5, 166 28 Prague 6, Czech Republic*

Abstract

Alkali-activation of fly ash together with an aluminum powder blowing agent led to the synthesis of inorganic fly ash-based foam (FAF). The FAF is characterized by means of its compressive and flexural strength, thermal conductivity and capacity, exposure to high temperatures, performance in chemically aggressive environments, and 2D morphology. In comparison to traditional autoclaved aerated C-S-H-based materials, FAF retains exceptionally good fire resistance and high chemical durability, exhibits a rather closed-pore network, and requires temperatures below 80°C for curing without the need for autoclaving. Experiments and micromechanical simulations prove that reasonable bulk densities lie in the range of 400 to 800 kg/m³.

Keywords: alkali-activation, fly ash, foam, chemical durability, thermal resistance, mechanical properties

1. Introduction

Autoclaved aerated concrete (AAC) presents the most commonly used inorganic foam. AAC is a lightweight inorganic construction material exhibiting excellent combination of thermal and mechanical properties. The AAC is usually produced from a fine-grained cement mortar with the help

*Corresponding author: Phone +420 22435 4482 (4483)

Email addresses: petr.hlavacek@fsv.cvut.cz (P. Hlaváček), vit.smilauer@fsv.cvut.cz (V. Šmilauer), frantisek.skvara@vscht.cz (F. Škvára), kopecky@fsv.cvut.cz (L. Kopecký), rostislav.sulc@fsv.cvut.cz (R. Šulc)

of aluminum powder. The reaction between aluminum powder and alkalis from the cement mortar liberates hydrogen, thus increasing the total volume of the mixture. Successive autoclave treatment improves the compressive strength and reduces drying shrinkage [1, 2].

A cement-based AAC is a well-known material in Europe since 1920's. A Swedish architect Johann Eriksson patented the AAC in 1923. The first AAC manufacturer in the world was established in Sweden in 1929, and the use of a fly ash (FA) as a filler was first mentioned in Lindman's patent in 1931 [3].

Despite the long AAC history, only few authors mentioned aerated alkali-activated materials. In 1987, Costopoulos patented a fly ash-based aerated concrete [4]. He used fly ash class C or class F blended with ordinary Portland cement that was aerated either by i) hydrogen peroxide releasing oxygen, ii) a sodium carbonate releasing carbon dioxide, or iii) acetic acid in a water solution. Prud'homme *et al.* [5, 6], on the other hand synthesized a geopolymer-based foam from dehydroxylated kaolinite activated by a solution of potassium hydroxide and potassium silicate, where silica fume served as a blowing agent. Delair *et al.* [7] examined the durability of a kaolinite-based geopolymeric foam in aqueous media. Bell and Kriven [8] prepared foams from metakaolin-based geopolymer, and Cilla *et al.* [9, 10] created an open cell geopolymer foam. A review of geopolymer foam concrete can be found in [11].

The world annual production of fly ashes is estimated to be around 600 million tons [12]. It is estimated that only 20-30% of FA is utilized, while the majority is dumped on landfills/lagoons, leading to an ecological burden. Several researchers have proved a successful utilization of fly ash by means of alkali-activation [13, 14, 15, 16]. The alkali-activation generally presents a reaction between a strong alkaline liquid (e.g. a solution of sodium hydroxide and sodium metasilicate) and a solid aluminosilicate material (e.g. fly ash, metakaolin or blast furnace slag). Depending on the authors, the reaction product is called soil-cement [17], geopolymer [18], inorganic polymer [19], or alkali-activated material [13, 20, 21, 22]. The stability of alkali-activated fly ashes has been proved by Wallah and Rangan by long term tests [15]. Further details on alkali-activated materials can be found in [23, 24, 25].

In this paper, we design, synthesize, and optimize an alkali-activated fly ash foam (FAF) at temperatures below 80°C. The FAF is a Portland cement-free, non-autoclaved, foam, composed of alkali-activated fly ash and aluminum powder. Hydrogen liberation during the activation process leads

to a closed-pore network. A laboratory-scale production process is elaborated and mixture compositions undergo optimization for their pore distribution and bulk density.

The FAF compressive and flexural strength, thermal conductivity and capacity, and residual strength after exposure to high temperatures and aggressive environments are determined and compared with traditional AAC. Finite element simulations on 2D representations complement the understanding of the FAF elasticity. A long-term chemical durability test proves the stability and the closed pore nature of the produced FAF.

2. Materials and blowing process

The fly ash class F from the Opatovice brown coal power plant, Czech Republic (Blaine 210 m²/kg) is used as the source material for alkali-activation, see Tab. 1 for the chemical composition. Fig. 1 shows the FA particle size distribution.

Table 1: Chemical composition of fly ash (wt %).

	SiO ₂	Al ₂ O ₃	Fe ₂ O ₃	CaO	K ₂ O	TiO ₂
Fly ash	51.9	32.8	6.3	2.7	2.12	1.89

The aluminum metal powder (Al) from Albo Schlenk Inc., Bojkovice, Czech Republic, product type 76013 (average particle diameter by mass, $d_{50} \approx 35 \mu\text{m}$), is used as an air entraining agent.

Sodium hydroxide pellets dissolved in sodium metasilicate constitute the alkali activator. The composition of the alkali activator, i.e. the sodium hydroxide to metasilicate ratio, is taken from our previous research on alkali-activated fly ash [16, 22, 26]. The solid/liquid ratio and the amount of Al metal powder is optimized with respect to the FAF stability, porosity, and pore distribution. Fine tuning of the composition is done iteratively. The final compositions of the mixes are given in Tab. 2 and the corresponding pore structures are shown in Fig. 2.

The reaction between the Al metal powder and the alkaline activator proceeds quickly, approximately as



When 0.045 g of Al metal powder is mixed with 50 g of FA and an activator, there is approximately 15 seconds for stirring and casting a specimen. The

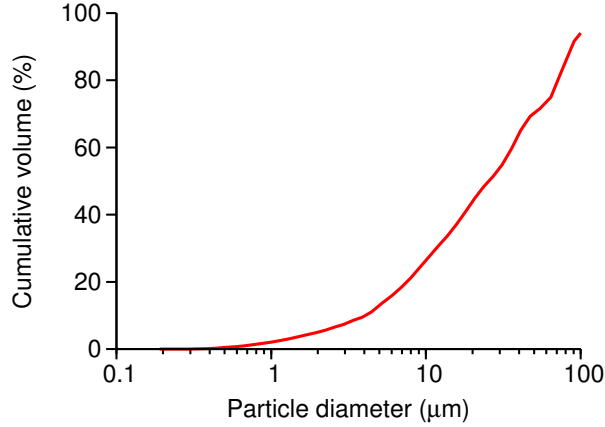


Figure 1: The particle size distribution curve of fly ash used in experiments.

Table 2: FAF compositions (the listed masses fill approximately the volume of 100 ml).

Mixture	FA (g)	Liquid/solid (-)	NaOH (g)	Na metasilicate (g)	Al (g)	Bulk density (kg/m^3)
FAF 1	50	0.37	2.8	15.7	0.030	751
FAF 2	50	0.38	2.9	16.1	0.030	778
FAF 3	50	0.39	3.0	16.5	0.030	772
FAF 4	50	0.37	2.8	15.7	0.045	700
FAF 5	50	0.38	2.9	16.1	0.045	671
FAF 6	50	0.39	3.0	16.5	0.045	626
FAF 7	50	0.37	2.8	15.7	0.060	574
FAF 8	50	0.38	2.9	16.1	0.060	521
FAF 9	50	0.39	3.0	16.5	0.060	422

hydrogen releases for about 1-2 minutes at ambient temperature. To reach a homogeneous pore distribution, the fly ash and Al metal powder are thoroughly mixed together in a dry state and the activator is added subsequently. Hand stirring takes place directly in a plastic form. Several attempts to mix the fly ash paste with the Al metal powder led to an improper pore distribution. The forms are kept under laboratory conditions at 22°C for two hours and subsequently put in the oven for 12 hours at 80°C . All specimens are prepared by cutting from larger bodies on a diamond saw.

Fig. 2 shows polished sections of the FAF with the mix compositions from Tab. 2. Since the proportions have four degrees of freedom, the composition

of the activation solution is fixed and suitable ranges for liquid/solid and Al/solid ratios are determined experimentally.

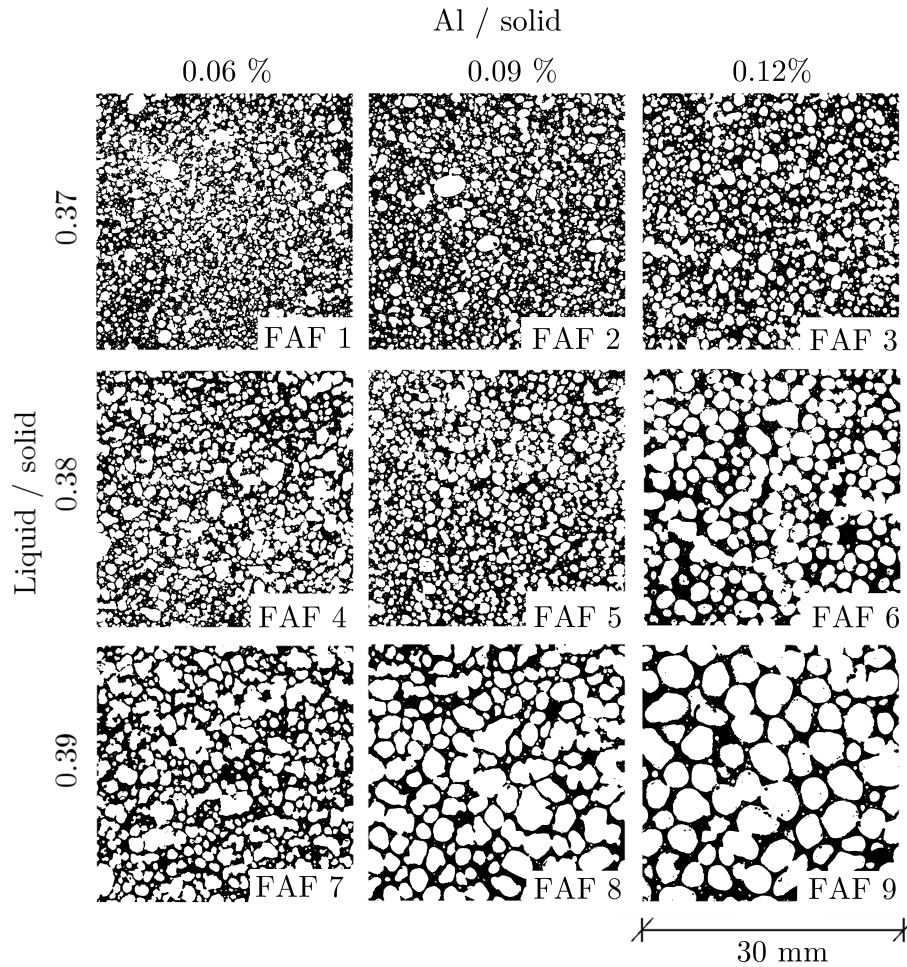


Figure 2: The liquid/solid and Al/solid effect on the FAF pore distribution (pores are filled with an acrylic sealant).

The FAF nucleation and stability of the pore structure at the fresh state strongly depends on the viscosity of the initial mix. The viscosity can be easily tuned by the amount of added liquid activator, i.e. by the liquid/solid ratio. Our experiments indicate that liquid/solid ratios above 0.39 results in pastes with low viscosity, allowing rapid pore nucleation and, when all formed hydrogen gas leaves, a deflation. On the other hand, FAF produced with

liquid/solid ratios under 0.37 results in high viscosity pastes that does not allow pore propagation; consequently, the corresponding specimens exhibit very low inflation. As it can be noticed in Fig. 2, the amount of Al metal powder has a less significant effect on the pore structure than the amount of liquid activator. The suitable amount of Al powder was found to be of approximately 0.1% of the fly ash mass.

For further testing, the composition FAF 5 is selected as the best representative of all mixes.

3. Methods

3.1. Mechanical properties

The uniaxial compression test on 30 mm cubes provides the stress-strain diagram. The compressive strength is calculated from the peak load and the Young's modulus of elasticity is derived from the linear part of the stress-strain curve. Flexural strength is determined from a three point bending test on $40 \times 40 \times 160$ mm³ prisms. Mechanical tests are performed on the TIRA test 2300 testing machine under a strain-controlled mode with deformation rate set at 0.5 mm/min.

3.2. Thermal conductivity and capacity

The thermal conductivity and volumetric heat capacity is measured on cylindrical specimens 15 mm thick and 70 mm in diameter under ambient conditions at 25°C on Applied Precision, IZOMET 2104.

3.3. Chemical durability

The resistance to aggressive environments is quantified by a loss of compressive strength, reduction of elasticity, and a weight loss. The 30 mm FAF cubes are immersed in solutions of Na₂SO₄, MgSO₄, NaCl, H₂SO₄, and HCl. The concentrations of sulphates are taken from the European standard for concrete [27]. Due to the lack of appropriate standards for the performance of cements in acidic media, the pH of acids is taken from Allahverdi and Škvára [28, 29], see Tab. 3 for the concentrations. The FAF cubes remain in the solutions for 90, 180 and 360 days, respectively. The solutions are replaced every 14 days to ensure a stable pH. The samples are removed and air-dried at 22°C two days prior to compressive tests.

Table 3: Details of chemical durability experiments.

Solution	Na ₂ SO ₄	MgSO ₄	NaCl	H ₂ SO ₄	HCl
Concentration	44 g/l	5 g/l	164 g/l	pH 2	pH 2

3.4. Fire resistance

The fire resistance test comprise temperature profiles according to Fig. 3. Prolonged exposures to 500°C, 800°C, and 1100°C act on 30 mm FAF cubes. The volume changes, mass losses and stress-strain diagram are recorded on cooled specimens.

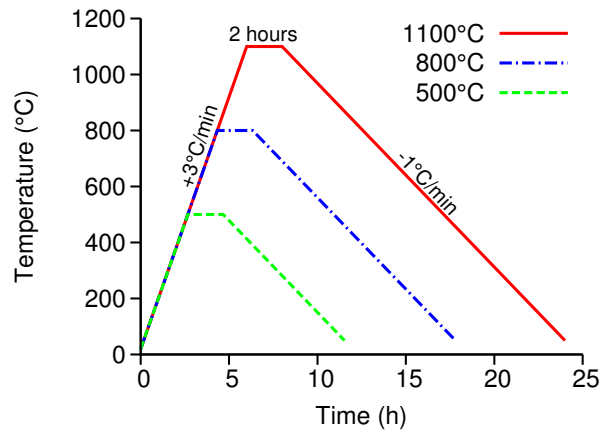


Figure 3: Temperature profile during the fire resistance test.

4. Results and discussion

4.1. Mechanical and physical properties

Tab. 4 summarizes the measured bulk density ρ^b , the compressive strength f_{cm} , the flexural strength f_{tm} , the thermal conductivity λ and the thermal capacity c_p on FAF 5. The values always represent an average of at least four measurements. In addition, Tab. 4 mentions a traditional AAC with a similar bulk density [30, 31].

Table 4: Data on FAF and traditional AAC [30, 31].

		FAF	AAC 600	AAC 675
Bulk density	ρ^b (kg/m ³)	671	600	675
Compressive strength	f_{cm} (MPa)	6.0	4.5	6.3
Flexural strength	f_{tm} (MPa)	1.0	0.85	1.0
Thermal conductivity	λ (W/m/K)	0.145	0.160	0.180
Thermal capacity	c_p (J/kg/K)	1089	-	-

4.2. Chemical durability

Resistance to chemically aggressive environments is determined by a long-term exposure at ambient temperature. Tab. 5 shows the evolution of the compressive strength, Young’s modulus and relative mass after 90, 180 and 360 days of exposure. The degree of pore saturation (ps) did not exceeded the value of 0.6 in any case, proving that the pores are of a closed nature. The results from Tab. 5 show that the most severe degradation of FAF occurs

Table 5: Compressive strength (f_{cm}), Young’s modulus (E), and relative mass (m_r) of FAF after chemical durability test.

	f_{cm} (MPa)			E (MPa)			m_r (-)		
	90	180	360	90	180	360	90	180	360
Na ₂ SO ₄	5.30	4.72	5.13	773	731	602	0.97	0.94	0.96
MgSO ₄	3.10	3.44	4.43	569	556	662	0.98	0.95	0.98
NaCl	3.27	3.77	2.68	511	526	409	1.00	0.99	1.00
H ₂ SO ₄	2.30	1.60	1.21	218	203	28	0.87	0.79	0.75
HCl	1.74	1.34	1.21	181	145	37	0.86	0.79	0.76

in HCl and H₂SO₄ solutions. FAF deteriorates in two mechanisms simultaneously. The first corresponds to Al depletion from N-A-S-H gel; specifically, the leaching leads to the ejection of Al from the aluminosilicate framework, leaving a relatively strong Si–O–Si skeleton [28]. Whereas the second mechanism corresponds to the dissolution of N-A-S-H gel in a low pH environment. The tested samples deteriorated up to 60 % in volume based on the degree of pore saturation. According to our previous research on alkali-activated materials that were exposed to sulphate solutions, no new crystalline phases appear in XRD [32]. It is worthy to note that C-S-H gel would disintegrate almost completely under such an acid environment [33].

4.3. Fire resistance

Fig. 4 shows the change of volume, mass, and color of FAF after the fire-resistance test. Almost all chemically and physically bound water is removed already at 800°C. The highest shrinkage increment appears between 800°C and 1100°C, which is related to gel sintering. A further positive effect is embodying Na directly in glass, implying a loss of efflorescence [26].

Tab. 6 displays the evolution of compressive strength and Young’s modulus. The increase of compressive strength and Young’s modulus for samples loaded by 1100°C can be explained by gel transformation into glass.

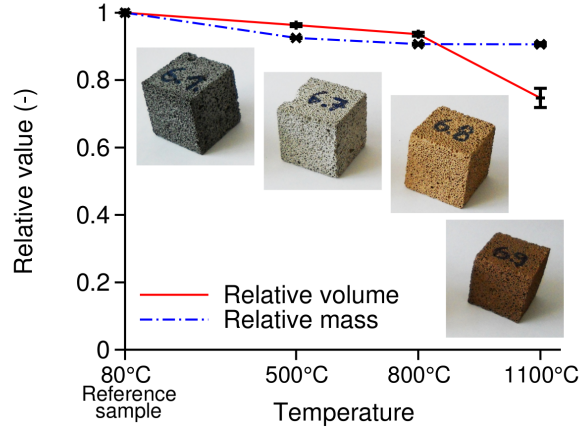


Figure 4: Relative changes of mass and volume of FAF with standard deviations.

Table 6: Compressive strength (f_{cm}) and Young’s modulus (E) of FAF after fire-resistance test, standard deviations in parentheses.

Temperature	f_{cm} (MPa)		E (MPa)	
reference 80 °C	5.99	(1.61)	833.8	(140.0)
500 °C	6.74	(1.82)	776.9	(116.2)
800 °C	5.13	(1.04)	734.1	(110.9)
1100 °C	13.25	(2.96)	1349.5	(188.4)

4.4. Homogenization of Young’s modulus

Effective Young’s modulus provides useful information on the microstructure, especially the interconnectedness of phases and their intrinsic elastic

properties. A 2D scan of FAF 5 (see Fig. 2) gives a starting microstructure for a numerical analysis aiming at simulating the effective Young’s modulus.

The porosity of FAF can be divided into two groups. The first one represents small micropores ($< 100 \mu\text{m}$), which reside in the activated fly ash paste. The second group are macropores ($> 100 \mu\text{m}$) creating the FAF pore structure. The macroporosity of the specimens ϕ^{macro} is calculated from a known bulk density of the paste $\rho_{\text{paste}}^{\text{b}} = 1752 \text{ kg/m}^3$ [22] and the measured FAF bulk density $\rho_{\text{foam}}^{\text{b}}$

$$\phi^{\text{macro}} = 1 - \frac{\rho_{\text{foam}}^{\text{b}}}{\rho_{\text{paste}}^{\text{b}}}. \quad (2)$$

The role of macroporosity on elasticity is explored on a 2D scan of FAF 5. The image is converted to 256 grayscales and 13 meshes generated with macroporosities in the range of 0.50–0.74 in 0.02 increments. Fig. 5 shows three different macroporosity values.

A burning algorithm explores the paste connectedness within the images. All connected paths are identified and disconnected parts from the edges eliminated. As the macroporosity increases, several unconnected paste clusters emerge. The ratio of the pixels that remains after the burning algorithm to the original amount is called solid percolation. Fig. 6 shows the extent. The solid percolation threshold represents the macroporosity where no path between the top and the bottom exists. In our particular case, this corresponds to a macroporosity of 0.72, which equals the FAF bulk density of 490 kg/m^3 . However, the solid percolation threshold in 3D would be higher due to out-of-plane solid paths [34]. This result is in agreement with the lowest bulk density of 400 kg/m^3 measured in our experiments.

The burnt images, see percolation of paste on Fig. 5, serve for creating a mesh where each black pixel corresponds to one quadrilateral finite element. The regular mesh has 500×500 elements with an element size of $40 \mu\text{m}$. Since the porosity is not meshed, the resulting mesh contains between 70 000 and 130 000 finite linear quadrilateral elements. The horizontal edges are loaded by kinematic uniform boundary conditions in the form of a prescribed displacement, while the vertical edges are kept free. The intrinsic Young’s modulus of alkali-activated paste is of 35.35 GPa and the Poisson’s ratio is set at 0.2; these values correspond to the degree of fly-ash reaction of 0.59 from our previous research [22]. Fig. 5 shows the whole process up to the final FE analysis.

The averaged vertical stress and strain provide the effective Young’s mod-

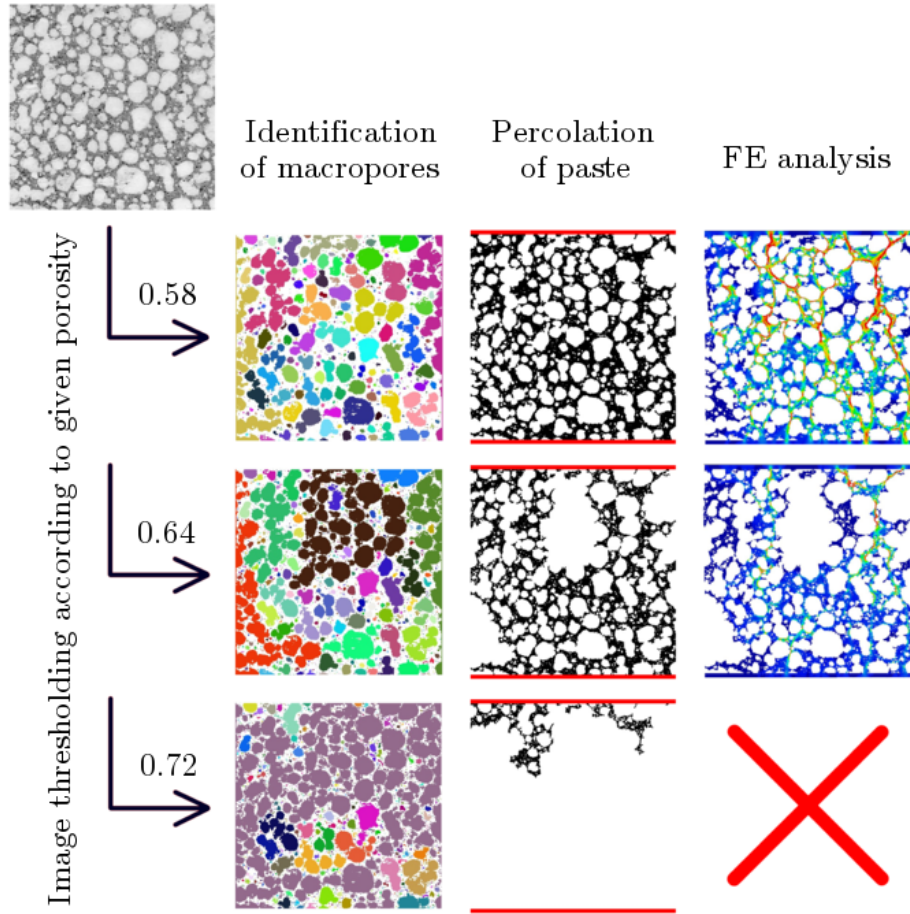


Figure 5: Image processing of FAF 5: thresholding, identification, percolation, stress σ_{22} .

ulus

$$E_{eff} = \frac{\langle \sigma_{22} \rangle}{\langle \varepsilon_{22} \rangle}, \quad (3)$$

which is shown in Fig. 7 for different macroporosities. The experimental modulus agrees well with the simulation results.

5. Conclusion

Fly ash, alkali activator, and aluminum powder led to the design, synthesis and optimization of fly ash foam (FAF). Variations in input materials

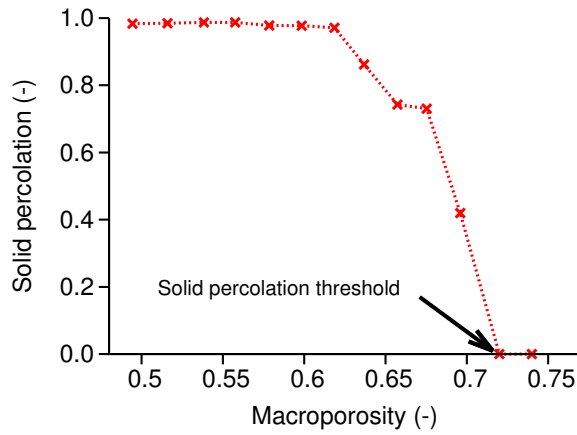


Figure 6: Solid percolation of FAF for different macroporosities.

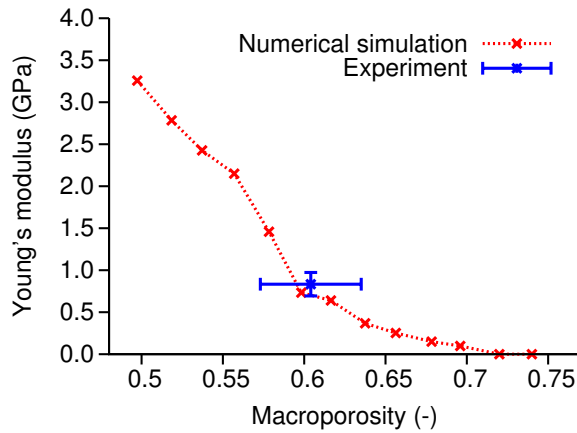


Figure 7: Young's modulus for various macroporosities.

proved feasible bulk densities in the range of 400 to 800 kg/m³. The initial mix viscosity was found crucial in the preparation process. Characteristic samples with bulk density of 671 kg/m³ exhibit similar properties to commercially produced autoclaved aerated concrete in terms of mechanical and thermal properties. FAF exhibit major benefits over traditional aerated materials:

- high fire resistance up to 1100°C accompanied by high shrinkage and material sintering;

- long-term chemical durability in a liquid aggressive environment of Na_2SO_4 , MgSO_4 , NaCl , H_2SO_4 , and HCl . The durability stems mainly from a closed-pore network and absence of leachable Ca in the FAF;
- fly ash utilization and the absence of autoclaving.

Acknowledgement

The authors are grateful to M. Vokáč for conducting mechanical tests and P. Semerák for measurements of thermal properties. Financial support from the Czech Science Foundation under the project GAP104/12/0102 is gratefully acknowledged for experimental part while the project GA13-22230S is appreciated for numerical simulations.

References

- [1] Narayanan N, Ramamurthy K. Structure and properties of aerated concrete: a review. *Cement Concrete Comp* 2000;**22**:321–9.
- [2] Jerman M, Keppert M, Výborný J, Černý R. Hygric, thermal and durability properties of autoclaved aerated concrete. *Constr Build Mater* 2013;**41**:352–9.
- [3] Pytlik RC, Saxena J. Autoclaved Cellular Concrete: The Building Material for the 21st Century. In: Wittmann FH, editor. *Advances in autoclaved aerated concrete*, Rotterdam/Brookfield: A.A. Balkema; 1992,1–18.
- [4] Costopoulos NG, Newhouse HK. Building material manufacturing from fly ash. US Patent 4,659,385; 1987.
- [5] Prud'homme E, Michaud P, Joussein E, Peyratout C, Smith A, Arrii-Clacens S, et al. Silica fume as porogent agent in geo-materials at low temperature. *J Eur Ceram Soc* 2010;**30**:1641–8.
- [6] Prud'homme E, Michaud P, Joussein E, Peyratout C, Smith A, Rossignol S. In situ inorganic foams prepared from various clays at low temperature. *Appl Clay Sci* 2011;**51**:15–22.

- [7] Delair S, Prud'homme E, Peyratout C, Smith A, Michaud P, Eloy L, et al. Durability of inorganic foam in solution: The role of alkali elements in the geopolymer network. *Corros Sci* 2012;**59**:213–21.
- [8] Bell JL, Kriven WM. Preparation of ceramic foams from metakaolin-based geopolymer gels. In: Lin HT, Koumoto K, Kriven WM, Garcia E, Reimanis IE, Norton DP, editors. *Developments in strategic materials, Ceram Eng Sci Proc*, New Jersey: John Wiley & Sons Inc; 2009;**29**:97–112.
- [9] Cilla MS, Colombo P, Morelli MR. Geopolymer foams by gelcasting. *Ceram Int* 2014;**40**:5723–30.
- [10] Cilla MS, Morelli MR, Colombo P. Open cell geopolymer foams by a novel saponification/peroxide/gelcasting combined route. *J Eur Ceram Soc* 2014;**34**:3133–7.
- [11] Zhang Z, Provis JL, Reid A, Wang H. Geopolymer foam concrete: An emerging material for sustainable construction. *Constr Build Mater* 2014;**56**:113–27.
- [12] Ahmaruzzaman M. A review on the utilization of fly ash. *Prog Energy Combust* 2010;**36**:327–63.
- [13] Shi C, Krivenko PV, Roy D. *Alkali-activated cements and concretes*. 1st ed. Oxon: Taylor & Francis; 2006.
- [14] Fernandez-Jimenez A, Palomo A. Characterisation of fly ashes. Potential reactivity as alkaline cements. *Fuel* 2003;**82**:2259–65.
- [15] Wallah SE, Rangan BV. Low-calcium Fly Ash-based Geopolymer Concrete: Long Term Properties. *Res. Report-GC2 Curtin University of Technology, Perth, Australia*; 2006.
- [16] Škvára F, Kopecký L, Šmilauer V, Bittnar Z. Material and structural characterization of alkali activated low-calcium brown coal fly ash. *J Hazard Mater* 2009;**168**:711–20.
- [17] Glukhovskiy VD. *Soil Silicates (Gruntosilikaty)*. Kiev: Budivelnik publisher; 1959.

- [18] Davidovits J. Synthesis of new high-temperature geo-polymers for reinforced plastics/composites. *In: Proceedings of PACTEC'79, Society of Plastic Engineers* 1979;151–4.
- [19] Van Jaarsveld J, Van Deventer J, Lukey G. The effect of composition and temperature on the properties of fly ash-and kaolinite-based geopolymers. *Chem Eng J* 2002;**89**:63–73.
- [20] Palomo A, Grutzeck MW, Blanco MT. Alkali-activated fly ashes. A cement for the future. *Cem Concr Res* 1999;**29**:1323–9.
- [21] Fernández-Jiménez A, Palomo A. Composition and microstructure of alkali activated fly ash binder: Effect of the activator. *Cem Concr Res* 2005;**35**:1984–92.
- [22] Šmilauer V, Hlaváček P, Škvára F, Šulc R, Kopecký L, Němeček J. Micromechanical multiscale model for alkali activation of fly ash and metakaolin. *J Mater Sci* 2011;**46**:6545–55.
- [23] Duxson P, Fernández-Jiménez A, Provis JL, Lukey GC, Palomo A, van Deventer JSJ. Geopolymer technology: the current state of the art. *J Mater Sci* 2007;**42**:2917–33.
- [24] Pacheco-Torgal F, Castro-Gomes J, Jalali S. Alkali-activated binders: A review: Part 1. Historical background, terminology, reaction mechanisms and hydration products. *Constr Build Mater* 2008;**22**:1305–14.
- [25] Provis JL, van Deventer JSJ. *Geopolymers: Structures, Processing, Properties and Industrial Applications*. 1st ed. Oxford/Cambridge/New Delhi: Woodhead Publishing Ltd; 2009.
- [26] Škvára F, Šmilauer V, Hlaváček P, Kopecký L, Cílová Z. A weak alkali bond in (N, K)–A–S–H gels: Evidence from leaching and modeling. *Ceram-Silikaty* 2012;**56**:374–82.
- [27] EN 206-1:2000, Concrete - Part 1: Specification, performance, production and conformity. *European Committee for Standardization*; 2000.
- [28] Allahverdi A, Škvára F. Acidic corrosion of hydrated cement based materials. *Ceram-Silikaty* 2000;**44**:152–60.

- [29] Allahverdi A, Škvára F. Sulfuric acid attack on hardened paste of geopolymer cements-part 2. Corrosion mechanism at mild and relatively low concentrations. *Ceram-Silikaty* 2006;**50**:1–4.
- [30] Neville AM. *Properties of Concrete*. New Jersey: John Wiley & Sons, Inc.; 1997.
- [31] Building Research Establishment. Autoclaved aerated concrete. *Digest* 1989;**342**:7 pp.
- [32] Jílek T. Vliv agresivního prostředí na vlastnosti geopolymerních materiálů [Thesis *in Czech*]. Institute of Chemical Technology, Prague; 2006.
- [33] Constantinides G, Ulm FJ. The effect of two types of C-S-H on the elasticity of cement-based materials: Results from nanoindentation and micromechanical modeling. *Cem Concr Res* 2004;**34**:67–80.
- [34] Bentz DP, Garboczi EJ, Snyder KA. A Hard Core/Soft shell Microstructural Model for Studying Percolation and Transport in Three-Dimensional Composite Media. *Res. Report: NIST Building and Fire Research Laboratory, Gaithersburg, Maryland*; 1999.